Defect-Related Photoluminescence of Zinc Oxide Nanorods

C. M. Mbulanga

2015

Defect-Related Photoluminescence of Zinc Oxide Nanorods

By

Crispin Munyelele Mbulanga

Submitted in partial-fulfilment of the requirementsfor the degree of

MAGISTER SCIENTIAE

In the Faculty of Science at the

Nelson Mandela Metropolitan University

December 2015

Supervisor: Prof Reinhardt Botha

Co-Supervisor: Dr Zelalem Urgessa

ACKNOWLEDGEMENTS

I would like to thank and express my gratitude to:

- My supervisor, Prof. J. Reinhardt Botha, who gave me the opportunity to work on this project within his group. He supported me throughout its full completion. I attribute the level of this Master’s degree to his encouragement and effort. One simply could not wish for a better and friendlier supervisor.
- My co-supervisor, Dr.Zelalem Urgessa, who has always been there to listen and engage heartily and endlessly in serious research-related discussions.
- All the professors and staff who have helped me throughout my time in the physics department, the nanophotonics group, and the international office as well.
- Prof. Hendrik Swart at the University of the Free State, Bloemfontein, for allowing me to use his facilities for surface characterization, and for his precious advices and discussions.
- Dr. Mart-Mari Duvenhage and Dr Liza Coetsee-Hugo at the University of the Free State University, Bloemfontein, for their advice in the interpretation of experimental data collected from their laboratories.
- All my current and previous colleagues at NMMU for their enormous support and a good conducive atmosphere in the lab.
- The South African Research Chairs Initiative of the Department of Science and Technology, the National Research Foundation and Nelson Mandela Metropolitan University for funding my studies. The African Institute for Mathematical Sciences, Senegal, is also acknowledged for providing the cash deposit needed for securing a South African study permit.
- My parents for their encouragement and support.
- Uncle Mr Jean Marie Mambo and his family for their love, financial support, and otherwise.
- Finally, and most importantly, to Mrs Nadege for her understanding and real love.

DECLARATION

I, Crispin Munyelele Mbulanga, s213514028, hereby declare that this MSc dissertation is my own work and has not previously been submitted for assessment or completion of any postgraduate qualification to another University or for another qualification.

Crispin Munyelele Mbulanga

CONTENTS

List of figures

List of tables

List of publications

C.M. Mbulanga, Z. N. Urgessa, S. R. Tankio Djiokap, J. R. Botha, M. M. Duvenhage and H. C. Swart: Surface characterisation of ZnO nanorods, *in press to Physica* B: Condensed Matter, 2015.

Z. N. Urgessa, **C. M. Mbulanga**, S. R. Tankio Djiokap, J. R. Botha, M. M. Duvenhage, H. C. Swart: The defect passivation effect of hydrogen on the optical properties of solution-grown ZnO nanorods, in press to *Physica B: Condensed Matter*, 2015.

Z. N. Urgessa, J. R. Botha, M. O. Eriksson, **C. M. Mbulanga**, S. R. Dobson, S. R. Tankio Djiokap, K. F. Karlsson, V. Khranovskyy, R. Yakimova, and Per-Olof Holtz: Low temperature near band edge recombination dynamics in ZnO nanorods, (Journal of Applied Physics, 116, 123506 (2014)).

S. R. Tankio Djiokap, Z. N. Urgessa, **C. M. Mbulanga**, A. Venter and J. R. Botha: Transport characteristics of n-ZnO/p-Si heterojunction as determined from temperature dependent current-voltage measurements, *in press to Physica B*: Condensed Matter, 2015.

Abbreviations

2D - Two dimensional
A^oX - Neutral acceptor bound exciton
AES - Auger Electron Spectroscopy
ASA - Atomic sphere approximation
BE - Bound exciton or Binding energy
C - Carbon
CBD - Chemical bath deposition
CB - Conduction band
CC - Configurational coordinate
Cl - Chlorine
DAP - Donor-acceptor pair
DBE - Deep band emission
DI water - De-ionized water
DLE - Deep Level emission
D^oX - Neutral donor bound exciton
E_g - Energy gap
F - Fluorine
FWHM - Full width at half maximum
FX - Free excitons
GGA - Generalized gradient approximation
H - Hydrogen
hcp - Hexagonal close packed
KE - Kinetic energy
L^a - Longitudinal acoustic
LDA - Local-density approximation
LMTO - Linearized muffin tin orbital
LO - Longitudinal optic
MBE - Molecular Beam Epitaxy
M_h - Hole effective mass
M_o - Electron effective mass
MOCVD - Metal-Organic Chemical Vapour Deposition
MOVPE - Metal-Organic Vapour-Phase Epitaxy
NBE - Near band edge emission
PA - Positron Annihilation
PL - Photoluminescence
PLS - Photoluminescence Spectroscopy
PLD - Pulsed Laser Deposition
PM - Photomultiplier
PP - Pseudopotential

PVP - Poly(vinylpyrrolidone)
RFMS - Radio Frequency Magnetron Sputtering
RT - Room temperature
SEM - Scanning Electron Microscopy
Si - Silicon
SIC-PP - Self-interaction corrected pseudopotentials
S - Sulfur
T^a - Transverse acoustic
TCE - Trichloroethylene
TES - Two electron satellite
TO - Transverse optical
ToF-SIMS - Time-of-Flight Secondary Ion Mass Spectroscopy
UV - Ultraviolet
VB - Valance band
XPS - X-ray Photoelectron Spectroscopy
XRD - X-Ray Diffraction
ZnO - Zinc oxide

ABSTRACT

In this dissertation, Zinc oxide (ZnO) nanorods grown by a two-step chemical bath deposition method on Si substrate is characterized. Research was conducted on ZnO nanorods for the understanding of their optical properties at room temperature (RT), with the emphasis on the visible luminescence. To this end, controlled thermal treatments of as-grown ZnO nanorods were conducted under different conditions, such as annealing time and environment, at atmospheric pressure. Results related to the following studies are reported: an investigation of the structure of ZnO nanorods, an analysis of the chemical composition of the surface, an investigation of the surface stoichiometry of the rods, and a study of defect-related photoluminescence of ZnO nanorods upon thermal treatment in different ambients.To achieve this, the samples were investigated by Scanning Electron Microscopy (SEM), X-ray Diffraction (XRD), Time-of-Flight Secondary Ion Mass Spectrometry (ToF-SIMS), X-ray Photoelectron Spectroscopy (XPS), Auger Electron Spectroscopy (AES) and room temperature (RT) photoluminescence Spectroscopy (PL).

As-grown ZnO nanorods exhibit a hexagonal shape and have the wurtzite structure; they have, respectively, an average length and diameter of ~900 nm and ~50 nm, and most of the rods are perpendicular to the substrate. The main extrinsic species found in as-grown nanostructures are C, H, F, S, and Cl. ToF-SIMS and XPS confirmed the presence of H related-defects, and the oxygen 1 S XPS peak at 531.5 eV is therefore assigned to oxygen bound to H-related defects. Based on stoichiometry studies, it is found that the near surface regions of as-grown ZnO nanorods (2 to 10 monolayers) are rich in Zn. The RT luminescence of as-grown ZnO nanorods exhibits a near band edge emission centered at ~379.5 nm and deep level emission extending from ~450 nm to ~850 nm. When these nanorods are thermally treated at high temperatures (>850 ^{o}C), it is found that even though their crystalline quality is preserved, their morphology is significantly affected, regardless of annealing ambient. Furthermore, in the near surface regions of annealed ZnO nanorods it is found that the Zn/O stoichiometric ratios deviate from unity. Specifically, oxygen vacancies form within the first 100 nm from the sample surface. Further from the surface, the material is deficient in Zn. It is deduced from XPS and AES that the ambient affects the activation rate of intrinsic defects. Furthermore, the only extrinsic defects that are affected by thermal treatment are found to be H-related defects. At high annealing temperatures (300 ^{o}C to ~700 ^{o}C), H-related defects are removed, and this removal process is found to affect significantly the RT luminescence properties of ZnO nanorods. Specifically, hydrogen passivates vacancy-related defects, depending on the thermal treatment. PL spectroscopy is used to follow this passivation effect as a function of annealing temperature, which causes an initial quenching followed by an enhancement of the green and the red luminescence, regardless of the ambient.

Finally, the green luminescence that arises following annealing above ~800 ^{o}C is assigned to Zn vacancy-related defects, while the red luminescence that dominates the visible band of ZnO nanorods upon annealing between 400 ^{o}C and 600 ^{o}C is suggested to be due to oxygen vacancy-related defects.

1. INTRODUCTION

Zinc oxide (ZnO) is a semiconductor with interesting properties, such as a large direct band gap and a stable free exciton, even above room temperature. Its high band gap (~3.37 eV) ensures a large breakdown field, and the thermal stability of the material allows high temperature operation. These properties make ZnO an ideal compound for high power and high temperature electronic devices, and have caused it to gain substantial interest in the research community [1-5]. Specifically, a growing interest exists in quasi-one-dimensional ZnO (e.g. nanorods, nanowires, nanobelts and nanotubes), considered as potential candidates for applications such as gas sensors [6], biosensors [1-2], nanolasers [3], optical waveguides [5], and light emitting diodes [3]. It is clear therefore, that ZnO nanostructures and its ternary alloys like $Mg_xZn_{1-x}O$ and $Cd_xZn_{1-x}O$ have the potential to compete with III-V nitrides for optoelectronic applications [7-8].

Several techniques have been used in the fabrication of ZnO. These include: gas-phase methods (vapour-phase transport [9], pulsed laser deposition [10], metal-organic chemical vapour deposition [11], molecular beam epitaxy [12] and the like) and aqueous solution-based methods (chemical bath deposition (CBD), hydrothermal growth and sol-gel methods). CBD is simple, requires no catalyst, is economical and can be carried out at significantly lower temperatures than most of the other techniques [13]; hence it has been used to produce the ZnO nanorods characterised in this study.

Nevertheless, for ZnO to be usable within industry a great deal more research still needs to be conducted, including on the control of native defect activation, and the understanding of the effect of intrinsic and extrinsic defects on the optical properties, compensation processes, the achievement of stable and repeatable p-type conductivity, etc. As an illustration, nanostructured materials have a large surface-to-volume ratio compared to epitaxial films, which amplifies defect-related effects on/near the surface of ZnO in many ways [14]. For optoelectronic applications such as light emitting diodes, surface states in the band gap can lead to technical challenges. These states are mostly due to non-stoichiometry, adsorbed foreign species and high concentrations of intrinsic defects in the near-surface region of ZnO. For example, the incorporation of hydrogen (H) in ZnO has been shown by cathodoluminescence spectroscopy to strongly affect the green luminescence in ZnO, and indeed in different ways, depending on deviations from the ideal stoichiometry [15]. Yang *et al.*[14], based on XPS investigations, showed also a correlation between surface radiative recombination and the presence of OH-bonds and chemisorbed oxygen on the surface of solution-grown ZnO nanorod arrays, as well as H-bonds on polar surfaces. Furthermore, Bai *et al.* [16] reported that the high surface coverage by hydroxyl (OH) groups can affect strongly the sensitivity of ZnO sensors. Therefore, it is important to investigate the structure, the complete chemical composition and the distribution of impurities, as well as the surface stoichiometry to achieve a better understanding of the origin and nature of deep centers involved in the PL of ZnO nanorods at room temperature (RT) [17-19].

In this work, we report and discuss surface-sensitive experimental results for solution-grown ZnO nanorods following thermal treatments in different ambients at atmospheric pressure. As-grown ZnO nanorods were studied first, followed by thermal treatment under different conditions, in order to investigate the effect of defects (extrinsic and intrinsic) on the optical properties. To this end, the morphology, crystalline properties and chemical composition as function of depth, annealing temperature and annealing ambient were respectively studied by Scanning Electron Microscopy (SEM), X-ray Diffraction (XRD) and Time-of-Flight Secondary Ion Mass Spectrometry (ToF-SIMS). In order to support ToF-SIMS results, X-ray Photoelectron Spectroscopy (XPS) and Auger Electron Spectroscopy (AES) analyses were conducted in order to investigate the stoichiometry of ZnO nanorods as function of annealing temperature. Finally, PL spectroscopy was used to study the effect of native and extrinsic defects on the RT optical properties, with the emphasis on the visible emission from ZnO.

Significant experimental evidence of the effects of thermal treatment on the morphological and crystalline properties, the identity of extrinsic defects and the stoichiometric properties of ZnO nanorods are provided. The presence of hydrogen in as-grown ZnO nanorods is confirmed and the effects of hydrogen and native defects upon thermal treatment on the RT optical properties are reported.

To provide a guide through the dissertation, the remaining chapters are previewed: a literature review is presented in chapter 2. Important characteristics of ZnO and established knowledge related to the material that have relevance to the present investigation are provided and discussed. This is followed in chapter 3 by a detailed discussion of characterisation methods that were used in the present study. The results obtained are presented and discussed in chapter 4. The main conclusions from this study are given in chapter 5.

2. LITERATURE REVIEW

In this chapter the fundamental properties of zinc oxide (ZnO) that are of relevance to the current investigation are briefly reviewed and summarised. Section 2.1 summarises some of the physical and electrical properties of ZnO. Section 2.2 presents theoretical calculations and related experimental results of the electronic band structure of ZnO. The basic radiative recombination mechanisms in ZnO in general, and the low temperature photoluminescence (PL) properties of ZnO nanorods grown by chemical bath deposition (CBD) in particular, are briefly discussed in section 2.3. Finally, section 2.4 summarises first-principles calculations of intrinsic point defects in ZnO and defect-related radiative recombination bands in ZnO.

2.1. Crystal and electronic band structure

2.1.1 Crystal structure

ZnO is an II^b-VI^a semiconductor. One of its constituents, namely zinc (Zn), has five stable isotopes, the most important ones being ^{64}Zn (48.89%), ^{66}Zn (27.81%), and ^{68}Zn (18.57%), whereas oxygen (O) generally exists as ^{16}O (99.76%) [20]. The electronic configuration of Zn is $1s^2\ 2s^2\ 2p^6\ 3s^2\ 3p^6\ 3d^{10}\ 4s^2$ and that of O $1s^2\ 2s^2\ 2p^4$. This shows that Zn and O have oxidation states of +2 and -2 respectively, forming ZnO as a compound. The possible phases are the cubic rock salt (NaCl) structure, cubic zinc blende structure and hexagonal wurtzite structure. They are represented in fig.2.1. At ambient pressure and temperature, the thermodynamically stable phase of ZnO is the hexagonal wurtzite structure. This is due to the strong electronegativity of oxygen 3.5, the second highest of all chemical elements, and the weak electronegativity of Zn compared to that of O [20]. Each atom of one kind is surrounded by four nearest neighbours of the other kind, forming a tetrahedral coordination consisting of sp3 covalent bonds. This covalent bonding is one of the facts that explains the high melting point (1975 ^oC) and relatively low density (5.606 g/cm^3) of ZnO. Furthermore, the wurtzite structure consists of two interpenetrating hexagonal close-packed (hcp) sub-lattices and exhibits a unique axis, the c-axis that is directed along one of the tetrahedral binding orbitals. However, due to the fact that the zinc-oxygen bond possesses also a very strong ionic character, ZnO is both a covalent and ionic compound with an ionicity of f_i=0.616 on the Phillips ionicity scale [20]. Per bond in the wurtzite lattice, the cohesive energy is approximately equal to 7.692 eV [21]. This value has been calculated theoretically using the generalized gradient approximation (GGA) method [21].

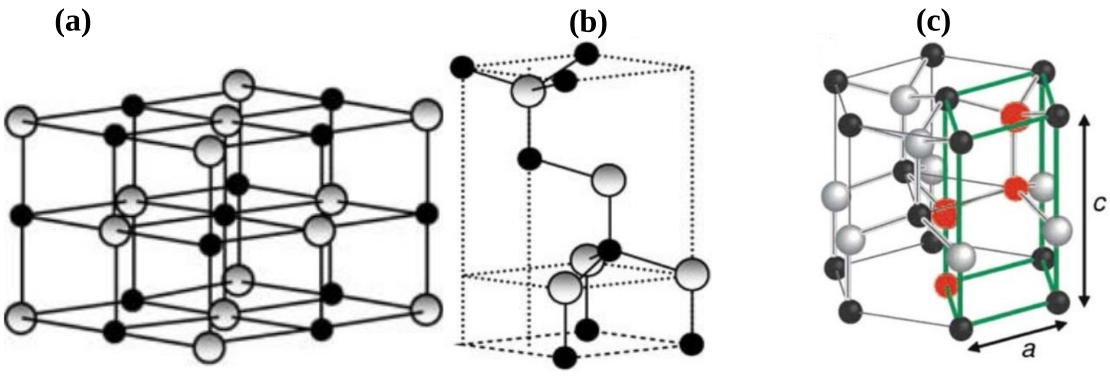

Figure 2.1. Different structures of ZnO: (a) Cubic rock salt, (b) Cubic zinc blende and (c) Hexagonal wurtzite. The shaded gray and black spheres denote zinc and oxygen atoms, respectively. The parallelepiped in (c) is the unit cell [24].

The point group of the hexagonal wurtzite structure (symmetry operations of ZnO) is 6mm (international notation) or C_{6v} (Schoenflies notation). The symmetry operations consist of a 6-fold rotation axis (the c-axis) and 6 mirror planes parallel to the axis of rotation. The conventional (primitive) unit cell is shown in fig. 2.1c in green and contains two pairs of ions.

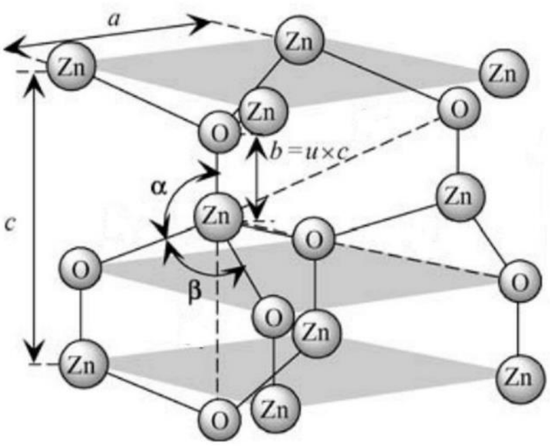

Figure 2.2. Schematic representation of a wurtzitic ZnO structure with lattice constants **a** in the upper basal plane and **c** in the basal direction, **u** parameter and bond angles **α** and **β** [24].

Fig. 2.2 displays the wurtzite ZnO structural parameters in details. The lattice parameters of the unit cell are **a** and **c,** with **u** an internal parameter describing the relative displacement between the group II and group VI sublattices, as showed in fig. 2.2. Reported **c/a** ratios for the natural crystal structure of ZnO are between 1.593-1.6035, deviating slightly from the ideal wurtzite ratio $c/a = \sqrt{8/3} = 1.633$ [22]. Furthermore, due to the sequence of Zn^{2+} and

O^{2-} ions in planes perpendicular to the crystallographic c-axis, there exists a dipole moment parallel to the c-axis between the polar Zn-terminated and O-terminated faces. The remaining faces show a non- polar character [23].

The crystal facets/planes are specified using either Miller indicesor Miller-Bravais indices Fig. 2.3a shows in blue the crystallographic axes related to the Miller indices [hkl] and in black those relating to the Miller-Bravais indices [HKIL], where $H = (2h-k)/3$, $K = (2k-h)/3$, $I = -(h+k/3)$ and $L = l$. Fig. 2.3b shows the typical polar Zn (or O)-terminated facets and lateral non-polar facets. Using the Miller-Bravais notations the Zn-terminated polar facets are denoted by (0001), whereas the O-terminated polar facets are indicated by (000$\bar{1}$). The six non-polar side facets are denoted by (01$\bar{1}$0), ($\bar{1}$100), ($\bar{1}$010), (0$\bar{1}$10), (1$\bar{1}$00) and (10$\bar{1}$0). Six faces are easily distinguishable in the magnified scanning electron micrograph of ZnO shown in fig. 2.3b.

In summary, the physical parameters of ZnO of interest are listed in table I. While most of these parameters are well-defined, uncertainty remains in some of them, such as the thermal conductivity. In the next section the electronic band structure of ZnO will be discussed in detail.

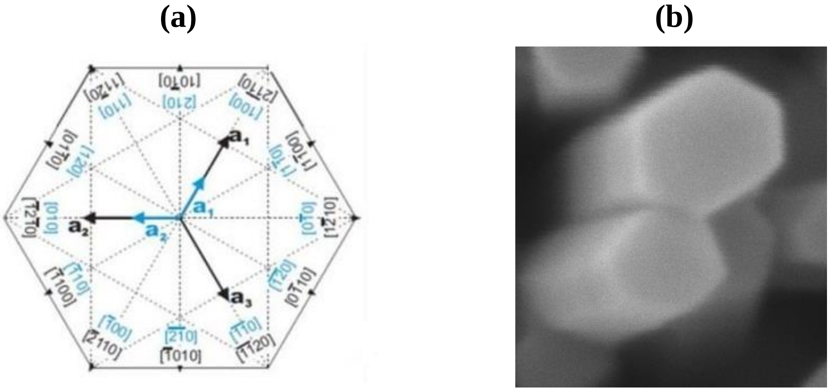

Figure 2.3. (a) Crystallographic axes shown using Miller indices [hkl] in blue, and the Miller-Bravais notation [HKIL] in black [13]; (b) SEM image of one ZnO nanorod showing the polar Zn (O)-terminated face and six lateral non-polar faces.

Table I. Some physical properties of ZnO (m_o is the free electron mass) [13].

Physical Parameter	**Value**
Density (g/cm^3)	5.606
Stable phase	Wurtzite
Melting point (^{o} C)	1975
Thermal conductivity (W/K.cm)	0.6-1.2
Linear expansion coefficient (/^{o} C)	a: $6.5x10^{-6}$ and c: $3.0x10^{-6}$
Static dielectric constant	8.656
Refractive index	2.008-2.029
Exciton binding energy (meV)	60
Electron effective mass (m_o)	0.24
Electron Hall mobility (low n-type conductivity) (cm^2/Vs)	200
Hole effective mass (m_o)	0.59
Hole Hall Mobility (for low p-type conductivity) (cm^2/Vs)	5-50

2.1.2 Electronic band structure

The electronic band structure of ZnO has been calculated for the cubic rock salt (NaCl) structure, cubic zinc blende structure and hexagonal wurtzite structure using different theoretical methods, including the local-density approximation (LDA), using atomic self-interaction corrected pseudopotentials (SIC-PP), the Korringa-Kohn-Rostoker Green's function method, the atomic sphere approximation (ASA) and linearized muffin-tin orbital (LMTO)) methods, including spin–orbit coupling (ASA–LMTO), within the LDA [21, 22, 24]. Only results for the hexagonal wurtzite structure are discussed here.

The ultimate aim is to approximate the solution of the following many-body time-independent Schrödinger equation for any electronic subsystem:

$$\left\{-\frac{\hbar^2}{2m}\sum_j \nabla_j^2 + \sum_j V_{ext}(r_j) + \frac{1}{2}\sum_{j\neq i}\frac{e^2}{\left|r_j - r_i\right|} - E\right\}\phi(r_1,...r_N) = 0 \qquad 2.1$$

where

$$V_{ext}(r_j) = -\sum_i \frac{Z_i e^2}{\left|r_j - R_i\right|} \qquad 2.2$$

is the external potential acting on electron j, due to nuclei of charges Z_i. Here i refers to nuclei and j to the N electrons in the subsystem; and R_i and Z_i respectively the coordinates and atomic number of the nuclei.

However, the wave function $\phi(r_1,...r_N)$ is a very complicated quantity that cannot be investigated experimentally and that depends on 4N variables: three spatial variables and one spin variable for each of the N electrons. Hence all theoretical methods are about the approximation of it and the associated Schrodinger equation using an electronic density as the basic variable in order to solve the Schrödinger equation.

Fig. 2.4 shows the band structure (E vs k) of ZnO. Calculations were done using the following methods: standard pseudopotential (PP), the SIC-PP, the LDA, and the SIC-PP [21]. The valence band (VB) maxima and the lowest conduction band (CB) minima occur at the Γ point k=0 indicating that ZnO is a “direct band gap semiconductor”. Fig. 2.4a shows 10 bands (occurring at around -9 eV in the right hand panel and at around -5 eV in the left hand panel) corresponding to the Zn 3d levels; the 6 bands from -5 eV to 0 eV correspond to O 2p bonding states. The lowest CB is formed from the empty 4s states of Zn^{2+} or the antibonding sp^3 hybrid states, whereas the VB originates from the occupied 2p orbitals of O^- or from the bonding sp^3 orbitals. Note that the fact that these results do not perfectly agree with experimental results does not invalidate this understanding of the band gap. In terms of accuracy, the ASA–LMTO method within the LDA proved to be more consistent with experiment. Table II presents both calculated and measured energy gap values for comparison.

Table II. Calculated and measured energy gaps E_g [13, 24].

	LDA-PP	**LDA-SIC-PP**	**ASA–LMTO within the LDA**	**Experiment**
E_g	0.23 eV	3.77 eV	3.437 eV	3. 3714 eV

In addition, it has been observed from experiments that the VB splits into three bands of states near the Γ point, named A, B, and C [24]. They are also referred to as the heavy-hole, light-hole, and crystal field split-off bands, respectively. In reality, from the influence of the hexagonal crystal field, the VB splits into two states: A and B [25]. Given the spin, a further splitting (owing to spin–orbit coupling) into three twofold-degenerate sub-VBs is induced.

The theoretical energy splitting between the A, B, and C bands are E_{AB} =10 meV and E_{BC}=34 meV [25]. The latter values are in good agreement with the experimental values measured for several bulk crystals which are E_{AB} = 9.5 meV and E_{BC}= 39.7 meV [26]. The next section focuses on basic recombination mechanisms and illustrates typical PL spectra of ZnO nanorods grown by CBD.

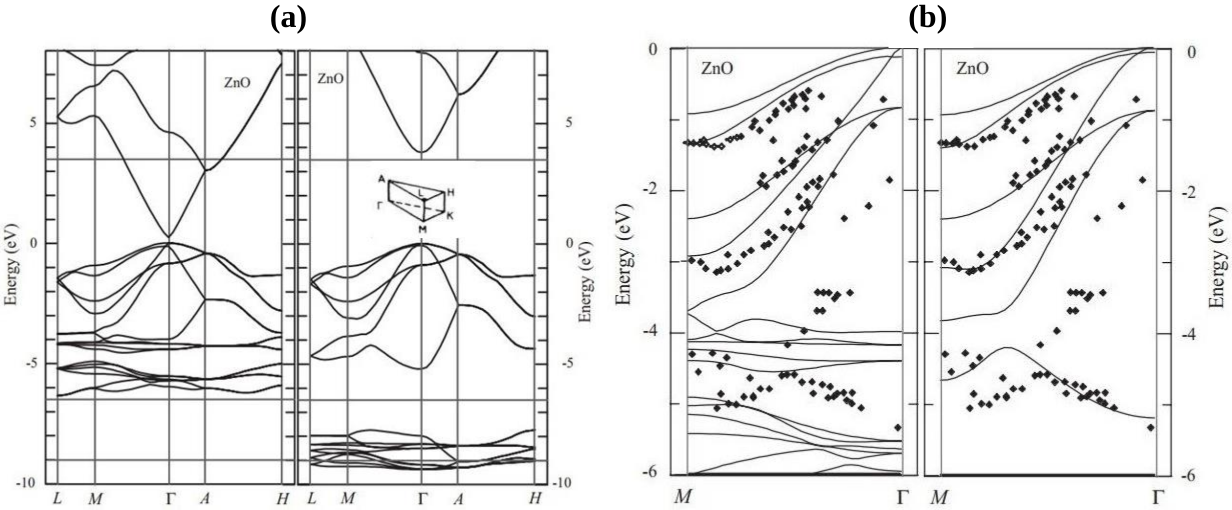

Figure 2.4. (a) LDA bulk band structure of ZnO as calculated by using a standard pseudopotential (PP) (left panel) and by using SIC-PP (right panel). (b) Comparison of calculated and measured valence bands of ZnO. The left panel shows the standard LDA, while the right panel shows SIC-PP results [21].

2.2. Photoluminescence of zinc oxide: overview

2.2.1. Recombination mechanisms

Luminescence in semiconductors refers to light emission from a material through any process other than blackbody radiation. Being a non-equilibrium process, external energy has to be supplied to the system in order for luminescence to occur. Luminescence is referred to as photoluminescence (PL) when it is caused by photon absorption.

Typically the material is irradiated by a laser with photon energy $\mathrm{h}\nu > E_g$, the band gap in k-space. Fig. 2.5 exhibits a simplified band structure of ZnO near the centre of the first Brillouin zone.

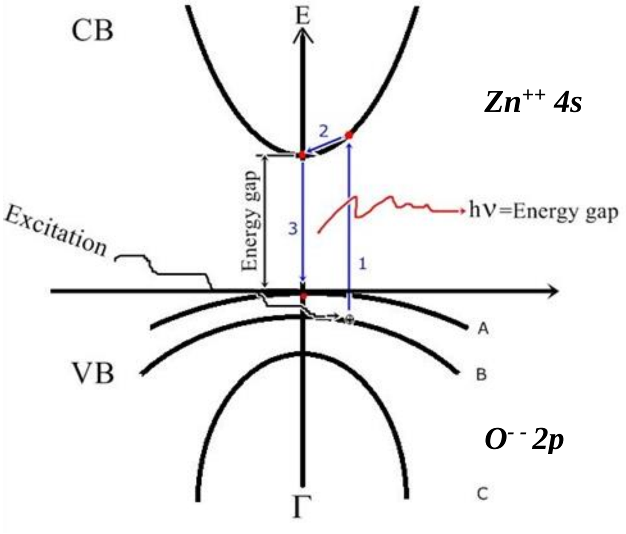

Figure 2.5. A simplified schematic drawing of the band structure of ZnO in the vicinity of the Γ point in k-space.

Under photo excitation an electron in the valence band gains energy and leaves behind a hole (see arrow 1). An electron-hole pair (e-h) is thus generated. The generated electrons and holes thermalize to the lowest energy states in their respective bands via phonon emission, as shown by arrow 2 before they recombine across the fundamental band gap (arrow 3). Excited electrons and holes can also recombine through defect/impurity levels situated in the forbidden band gap. In general, recombination can happen through either radiative or non-radiative processes. When recombination produces light (photons), the process is called “radiative recombination”; if not, it is called “non-radiative recombination”.

Radiative recombination involves different mechanisms. Possible radiative recombination mechanisms are illustrated in fig. 2.6a. Recombination mechanisms involving native defects will be discussed later in more detail. Fig. 2.6b shows exciton-related low temperature radiative recombination lines most often observed in the PL of ZnO [20, 27, 28-29].

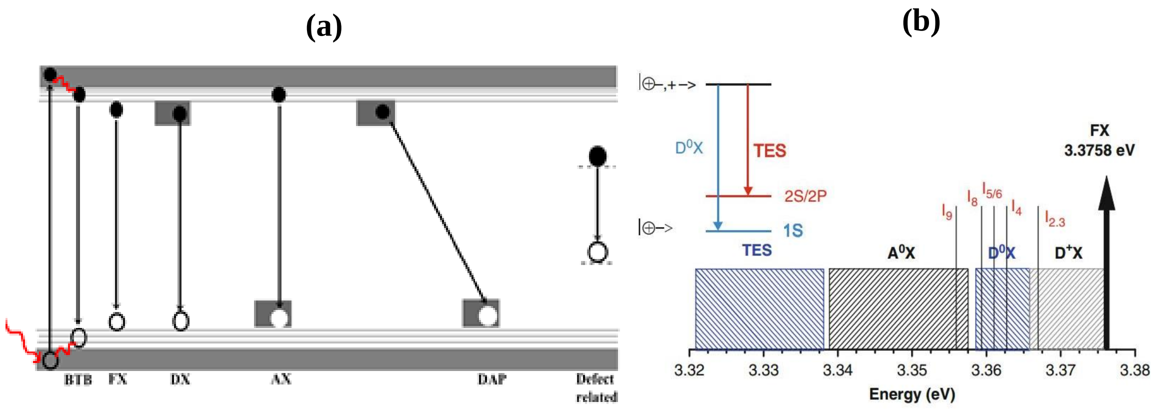

Figure 2.6. (a) Possible mechanisms of e-h recombination; (b) A schematic drawing of the energy ranges (shaded and in colour) where the various bound exciton transitions in ZnO can be found together with the level scheme for the two-electron transitions of the neutral donor bound excitons (20). BTB stands for band-to-band, while other abbreviations are described in the text.

a. Free excitons (FX)

Due to the mutual Coulomb interaction, an excited electron in the CB and a hole in the VB can be bound together and form a hydrogen-like state. Consequently, the Coulomb interaction between the electron and the hole lowers the energy of the e-h pair such that the difference between the electron and hole energies of the coupled pair becomes less than that of the band gap energy E_g (see fig. 2.6). The Coulomb-coupled e-h pair thus formed is called an “exciton”. If it can move freely in the material, it is called a “free exciton (FX)”. The free exciton energy E_{FX} is given by

$$E_{FX} = E_g - E_{FX}^{binding} \qquad 2.3$$

where the binding energy $E_{FX}^{binding}$ of the free exciton is given by

$$E_{FX}^{binding} = -\frac{1}{n^2}\frac{\mu}{m_o}\frac{1}{\kappa_o{}^2}R_H\,. \qquad 2.4$$

The parameter n is the principal quantum number, R_H the Rydberg constant (13.6 eV) for the hydrogen atom, κ_o the static dielectric constant and μ the reduced mass $\frac{1}{\mu} = \frac{1}{m_e} + \frac{1}{m_h}$, where m_e and m_h are, respectively, the electron effective mass and hole effective mass. For ZnO, the ground state (n=1) exciton binding energy is approximately 60 meV [27] (see table I also).

b. Bound excitons (BE)

Excitons can localize at impurities, point defects, other potential fluctuations or even large scale defects such as surfaces [13, 27]. The resulting configuration is called a “bound exciton (BE)”. A transition involving an exciton bound to a neutral donor is denoted (D^o, X); a transition involving an exciton bound to a positively ionised donor is denoted (D^+, X); similarly, (A^o, X) is a transition involving an exciton bound to a neutral acceptor (see fig. 2.6b). The photon energy emitted from any of these transitions is given by:

$$E_{BE} = E_{FX} - E_{loc} \qquad 2.5$$

where E_{loc} is the exciton localization energy, which is the energy required to remove the exciton from the impurity/defect. This localization energy is related to the impurity ionisation energy E_i using Haynes’ empirical rule [28]:

$$E_{loc} = b + cE_i \qquad 2.6$$

where b and c are constants (material dependent) and are determined experimentally.

c. Donor-Acceptor Pair (DAP) Transitions

When donor and acceptor impurities are both present in the material at a close proximity so that their wave functions overlap, a loosely bound donor electron can recombine with a hole on to a neutral acceptor (see fig. 2.6a). This process is called “donor-acceptor pair recombination (DAP)”. The energy of the emitted photon during this type of transition is given by

$$h\nu = E_g - E_{iD} - E_{iA} + \frac{1}{4\pi\varepsilon_o}\frac{e^2}{\kappa R} \qquad 2.7$$

where E_{iD} and E_{iA} are the donor and acceptor ionisation energies, respectively, and ε_o and κ are the permittivity of vacuum and the dielectric constant of the material, respectively. R is the distance between the donor and the acceptor for the specific pair. The bigger the separation of the pair, the smaller the Coulomb interaction is and thus the lower the photon energy. The emission energy should then increase as the pair separation decreases. For partially ionic bonding as in ZnO, DAP transitions cause polarization of the crystal lattice that leads to lattice distortions [24]. Therefore, DAP transitions are always accompanied by phonon replicas due to the relaxation of the lattice. In ZnO, the energy separation between longitudinal (LO) phonon replicas is 72 meV [29].

d. Two electron satellite (TES) transitions

During the recombination of an exciton bound to a neutral donor, the donor final state can be the 1s state (yielding the normal (D^o, X) line in the PL spectrum) or the 2s/2p state, yielding the so-called two electron satellite (TES) transition lines (see the insert in fig. 2.6b). The energetic distance between the (D^o, X) and its TES, is therefore the difference between the donor energies in the 1s and 2s/2p states, which is 3/4 of the donor ionisation energy in the simple hydrogen-like effective-mass-approach (EMA) [20]. The photon energy E_{TES} of the TES is given by:

$$E_{TES} = E_{D^o X} - E_{iD}\left(1 - \frac{1}{n^2}\right) \qquad 2.8$$

For n = 2

$$E_{TES} = E_{D^o X} - \frac{3}{4}E_{iD} \qquad 2.9$$

e. Free-to-Bound Transitions

Free electrons can also recombine (radiatively or nonradiatively) with holes trapped on the acceptors. This happens at sufficiently low temperatures when carriers are “frozen” on impurities. Such transitions, involving a free electron and a hole bound to an impurity, are known as “free-to-bound transitions”. The emitted photon energy in the case of radiative recombination is given by E_g-E_{iA}, where E_{iA} *is* the shallow acceptor ionisation energy [30].

In general, the above mentioned recombination channels in ZnO are grouped into two major energy regions: the near band edge (NBE) region and the deep level emission (DLE) region. Fig. 2.7 is a typical photoluminescence spectrum of solution grown ZnO at room temperature (RT). The NBE region is in the ultra violet spectrum and the DBE region in the visible and near infrared spectral regions.

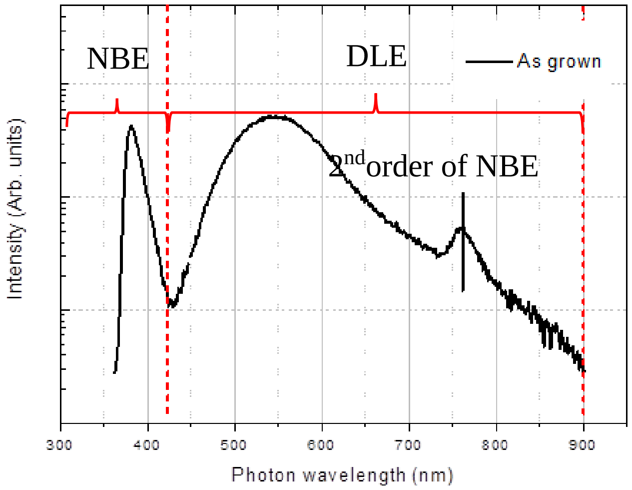

Figure 2.7. Typical photoluminescence spectrum of solution grown ZnO at room temperature.

2.2.2. Low temperature PL characteristic of solution grown zinc oxide nanorods

Solution growth of ZnO nanorods on Si substrate usually consists of two steps: formation of a seed layer followed by the growth (from solution) of nanorods on the seed layer. More details about the chemical bath deposition (CBD) method will be given in chapter 3. Fig. 2.8 shows a typical NBE steady state low temperature PL spectrum of solution grown ZnO. Several lines are observable: those at 3.322 eV, 3.3628 eV and 3.374 eV are ascribed to (e, A^o), (D^o, X), and FX recombination, respectively [13]. The line (e, A°) is followed by its first, second and third phonon replicas at 3.11 eV, 3.18 eV, and 3.25 eV, respectively; phonon replicas of the FX line co-exist with these and are indicated by the arrows in fig. 2.8 [13]. A complete summary of bound exciton related lines in ZnO is given in table III [31]. For a better understanding of the concentrations of defects and their formation energies, as well as the diffusion mechanisms of vacancies and interstitials in ZnO crystals, results from theoretical investigations and relevant experiments are discussed in the next section.

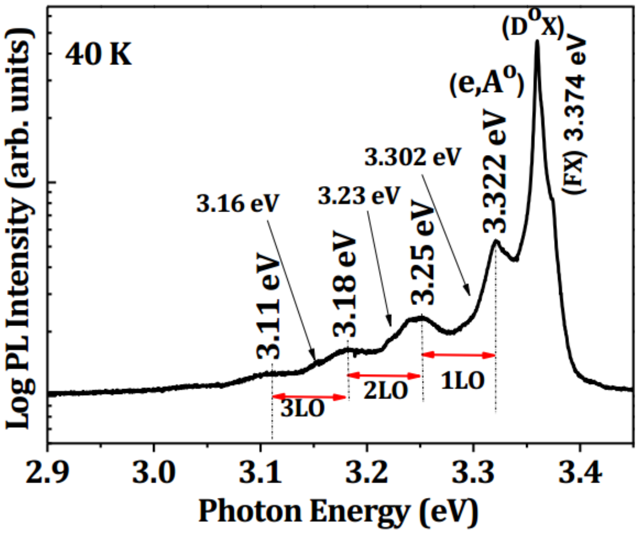

Figure 2.8. Low temperature (40 K) steady state PL spectrum of a sample of solution grown ZnO nanorods annealed at 700 °C [13].

Table III. Energy positions of free and neutral donor–bound exciton recombination lines reported for ZnO at 11 K [31]. The wavelength to energy conversation was done using $E(\mathrm{eV})=1239.7(6)/\lambda$ (nm).

	Line	*Wavelength (nm)*	*Energy (eV)*	*Chemical identity*
ZnO nanorods at 11 K	A_L^a	367.10	3.3770	-
	A_T^a	367.26	3.3759	-
	-	368.44	3.3647	-
	I_4	368.34	3.3628	Hydrogen
	I_5	368.86	3.3614	-
	I_6	368.92	3.3608	Aluminium
	I_{6a}	368.96	3.3604	-
	I_7	369.01	3.3600	-
	I_8	369.03	3.3598	Gallium
	I_{8a}	369.08	3.3593	-
	I_9	369.37	3.3567	Indium
	I_{10}	369.76	3.3531	-
	I_{11}	370.28	3.3484	-

A_L^a is the longitudinal and A_T^a the transversal free A-exciton states.

2.3. Native point defects in zinc oxide: first-principles studies and recent experimental findings

In this section, first principles formalisms and corresponding predictions are reviewed after a brief inventory of native point defects in ZnO. Special attention is given to defect concentrations formation energies, and transition energies, as well as the diffusion mechanisms of vacancies and interstitials in wurtzite ZnO crystals. It is worth knowing that the effects of the association of impurities with intrinsic defects and the interaction between defects have not been taken into account in theoretical investigation reported here. Therefore, all the predictions given below will be interpreted within these limitations and used as an indication of what the behaviour would be if only non-interacting defects were present in the material.

2.3.1 Defects in zinc oxide

Defects are classified into two categories: intrinsic defects (or native defects) and extrinsic defects (or impurities). They disrupt the perfect arrangement of the atoms in the crystal and affect, amongst other, the optical properties of the material. Intrinsic defects are also classified into point defects and extended defects. Point defects usually involve isolated atoms in a localized region, whereas extended defects, on the other hand, can be classified into line, planar and bulk defects. A 2D illustration of vacancies, interstitials and substitutional defects in semiconductors is given in fig. 2.9.

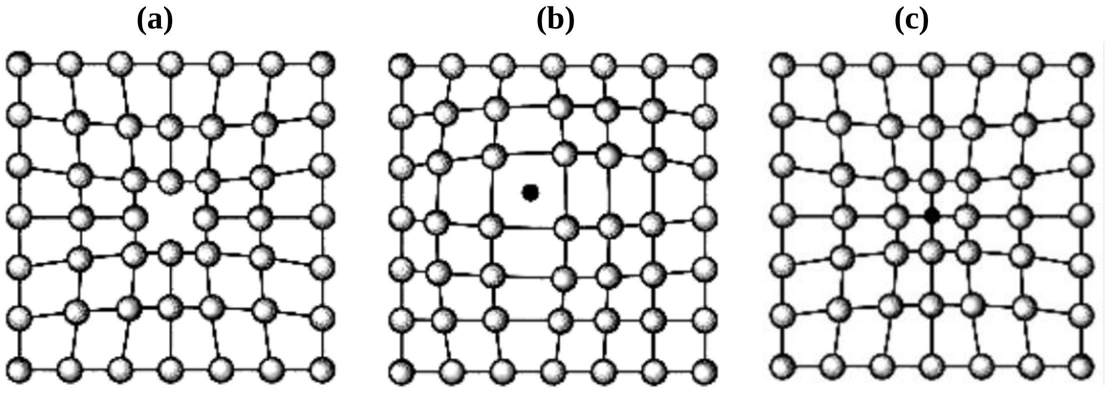

Figure 2.9. Illustration of point defects in a semiconductor: (a) vacancy, (b) interstitial atom and (c) substitutional defect.

In ZnO, possible intrinsic defects are O (Zn) vacancies, denoted as $V_{O(Zn)}$, O (Zn) interstitials (O_i/Zn_i) and O (Zn) anti-sites (O_{Zn}/Zn_O). In the wurtzite structure only two possible interstitial sites exist: the first one is tetrahedrally (tet) coordinated and the second one is octahedrally coordinated [32]. Table IV summarises all possible native defects identified either by their charge state or using the Kroger-Vink notation. In addition to native defects, a combination of one or more point defect(s) and (or) one extrinsic element can form also defects called “clusters or complexes” (e.g. V_OZn_i formed by V_O and Zn_i [33-35]). Species adsorbed on the surface of ZnO, such as ordered ad-layers including carbon IV oxide (CO_2), carbon II Oxide (CO), water molecules (H_2O), hydroxyl (OH) groups and hydrogen (H) atoms are other possible impurities [36, 37].

Table IV. Possible native defects identified either by the charge state or using the Kröger-Vink notation [32].

Defect	**Charge state**	**Kröger-Vink notation**
Zn_i	0	Zn_i^x
Zn_i	+1	$Zn_i^\bullet$
Zn_i	+2	$Zn_i^{\bullet\bullet}$
O_i	-2	O_i''
O_i	-1	O_i'
O_i	0	O_i^x
V_{Zn}	-2	V_{Zn}''
V_{Zn}	-1	V_{Zn}'
V_{Zn}	0	V_{Zn}^x
V_O	0	V_O^x
V_O	+1	$V_O^\bullet$
V_O	+2	$V_O^{\bullet\bullet}$
Zn_O	0	Zn_O^x
Zn_O	+2	$Zn_O^{\bullet\bullet}$
O_{Zn}	-2	O_{Zn}''
O_{Zn}	0	O_{Zn}^x

2.3.2 Formalism and theoretical results

a) Defect concentration and formation energies

The concentration of an isolated defect d (denoted by C_d) in a crystal depends on its free energy of formation ΔG_f. At equilibrium, the defect concentration follows the following Arrhenius behaviour [38]:

$$C_d = N_{sites} e^{-\Delta G_f / k_B T} \quad 2.10$$

where N_{Sites}, ΔG_f, and k_B represent the number of possible sites for the defect d in the crystal per unit volume, the free energy of formation of the defect d, and the Boltzmann constant, respectively. At a given temperature T and a pressure P, the free energy for the formation of a defect is given by [38]

$$\Delta G_f = \Delta E_f - T\Delta S_f + P\Delta V_f \quad 2.11$$

where ΔE_f is the change in the total energy of the system, ΔS_f the change in entropy and ΔV_f the change in volume when a defect is introduced in the system.

At zero Kelvin, the defect formation energy in a given charge state q in ZnO is given by [32, 39]:

$$\Delta E_f = E(\mathrm{N_{Zn}}, \mathrm{N_O}) - N_{Zn}\mu_{Zn} - N_O\mu_O + \mathrm{q}\,\varepsilon_F \quad 2.12$$

where $E(N_{Zn}, N_O)$ stands for the total energy of the system containing N atoms of zinc and oxygen, μ_{Zn} and μ_O are chemical potentials of Zn and O, respectively. The parameter ε_F stands for the Fermi energy taken as the energy of the reservoir from which an electron is removed to form a defect with charge q. Chemical potentials depend on the conditions of growth and determine the off stoichiometry of the system [32].

From equations 2.10, 2.11 and 2.12 it can be seen that amongst other parameters, the concentration of a defect depends also on the chemical potentials set by the growth environment.

b) Diffusion of defects in zinc oxide

Consider again a point defect d. The rate Γ_i^d at which the defect d moves via a migration path i can be described also by an Arrhenius behaviour [40]:

$$\Gamma_i^d = \Gamma_{0,i} e^{-\Delta G_i / k_B T} \tag{2.13}$$

where $\Gamma_{0,i}$ is an attempt frequency. It is frequently approximated by a characteristic frequency such as the Einstein or Debye frequency [40]. The free enthalpy of migration ΔG_i is given by [40]:

$$\Delta G_i = \Delta H_i - T\Delta S_i + P\Delta V_i \tag{2.14}$$

where ΔH_i is the enthalpy of migration (migration barrier), ΔV_i is the migration volume, and ΔS_i the migration entropy. All the other symbols in 2.13 and 2.14 have their usual meaning as defined above.

c) Different first principles predictions

Native defect concentration and formation energies

Formation energies of native point defects and their concentrations have been calculated based on first principles formalism using the plane-wave pseudopotential approach by Kohan *et al*. [32]. The local-density approximation (LDA) was used in order to solve the equation of Schrödinger (see eq. 2.1) during the estimation of the band gap. Even though a useful basic theoretical understanding on the formation and concentration of defects can be obtained from these calculations, the inaccuracy in determining the band gap also introduces uncertainty. Consequently, all results that depend on the accuracy of the theoretical band gap of ZnO compared to the experimentally known value (see table II) such as formation energies, will be affected by the non-accurate prediction of the band gap (~0.91 V) by LDA.

Fig. 2.10 shows the formation energies as a function of Fermi level for the most dominant defects at equilibrium, under (a) Zn-rich conditions and (b) O-rich conditions. Only the lowest formation energies are presented as function of the Fermi level in the case of Zn-rich (or high Zn partial pressure) and O-rich (or low Zn partial pressure) environments. Calculations were done for environments with a temperature of 1000 K (726.85^{o}C) using eq. 2.10 [32]. In fig. 2.10a and b the change in formation energy of a particular charge state is shown for the Fermi energy range where this state has the lowest energy, and the "slope" of the lines corresponds to the charge state of the corresponding defect (see Eq. 2.12).

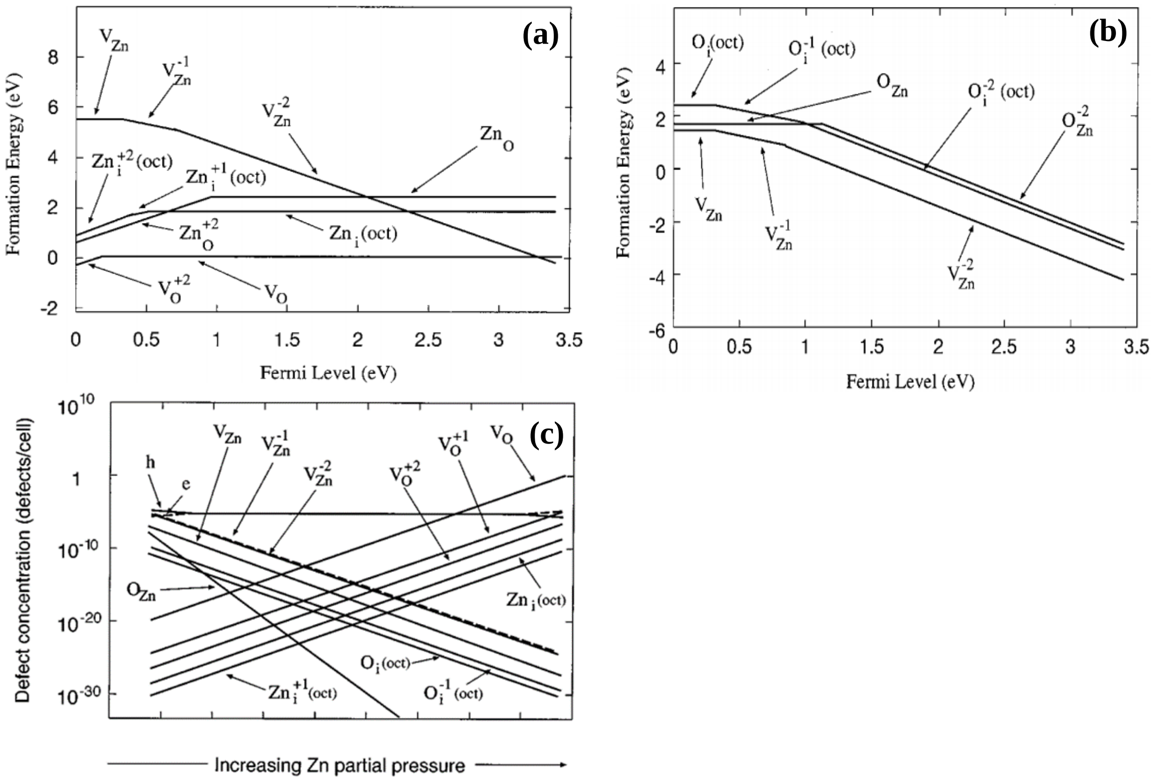

Figure 2.10. Calculated defect formation energies for dominant defects (lowest formation energy values) as function of the Fermi level: (a) when there is Zn in excess; (b) when there is a shortage of Zn. The zero Fermi level is set to the top of the VB. (c) Intrinsic defect concentrations at 1000 K (726.85°C) computed using eq. 2.10 [32].

From fig. 2.10a and 2.10b, it can be seen that V_O and V_{Zn} have the lowest formation energies. It follows that in a Zn-rich environment the most abundant native defect expected to form is V_O, in particular V_O^x and $V_O^{\bullet\bullet}$ due to their lowest formation energies (see fig 2.10a). When there is a shortage of Zn, the most abundant native defects to form are V_{Zn}, in particular V_{Zn}^x, V_{Zn}' and V_{Zn}'' (see fig. 2.10b). Therefore, V_O and V_{Zn} should be the most abundant native defects in ZnO depending on the environmental conditions. Moreover, as can be seen from fig. 10c, which plots intrinsic defect concentrations as function of Zn partial pressure, V_O and V_{Zn} remain the predominant defects at 726.85°C even though O_i and Zn_i defects are present as well. However, when the underestimated band gap predicted by LDA methods is corrected at equilibrium, V_{Zn} dominates in an O-rich environment whereas V_O ceases to be the most dominant defects in a Zn-rich environment – rather, the most dominant defect will be Zn_i (Data not shown here) [32].

Diffusion of oxygen and zinc in zinc oxide

The mobility of most dominant point defects, i.e. their ability to diffuse at certain temperatures, has been predicted through first-principles calculations by Tsurkan e*t al.* [24] and Erhart *et al*. [41]. The shortcoming of the LDA and generalized gradient approximations, in that they underestimate the band gap of ZnO, does not affect the validity of these calculations [41].

Fig. 2.11 presents the charge state dependent enthalpies of migration of some dominant native defects in the case of O-rich and Zn-rich environments. Fig. 2.11a presents the migration barriers for O_i in an O-rich environment whereas fig. 2.11b presents the migration barriers for Zn_i in a Zn-rich environment [41]. Both the in-plane and out of plane migration mechanisms were considered.

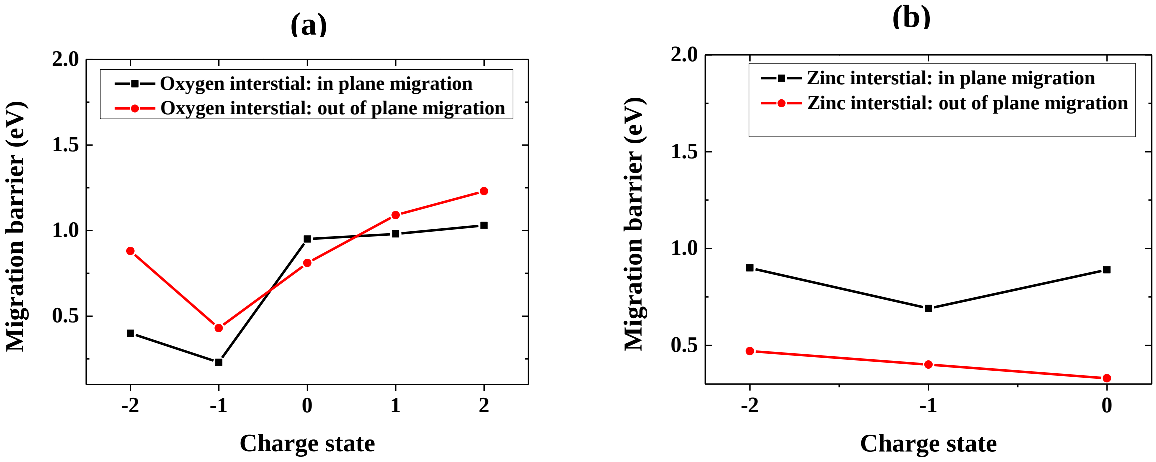

Figure 2.11. (a) Charge state dependence of migration enthalpies of interstitial (a) oxygen and (b) zinc [41].

As can be seen from fig. 2.11a, the diffusion barriers of oxygen interstitials with charge states *q=-1* and *q=-2* in an O-rich environment are very small (≲ 1 eV), hence they are mobile at low temperature [41]. Specifically, Erhart *et al.* [41] found that O_i' diffuses already between -193.15°C and -173.15°C, and O_i'' between -143.15°C and -113.15°C [41]. In the case of a Zn-rich environment, fig. 2.11b shows that for any charge state, the migration barrier for Zn_i is less than 1 eV [41] meaning that at low temperature Zn_i should be mobile. Specifically, it was found that $Zn_i^{\bullet\bullet}$ migration happens between -183.15°C and -163.15°C; $Zn_i^{\bullet}$ between -163.15°C and -143.15; and Zn_i^{x} between -173.15°C and -

153.15°C [41]. At high temperature, Tsurkan *et al.* [24] estimated the annealing temperature above which V_{Zn} and V_O can be mobile. It has been reported that V''_{Zn}, V_O^x and $V_O^{\bullet\bullet}$ start to diffuse through different mechanisms (which are not described here) at 265.85°C, 381.85°C and 635.85°C, respectively, in ZnO [24, 41].

2.3.3 Reported defect related optical transitions in zinc oxide

2.3.3.1 Deep level emission positions in the forbidden band gap

Excited electrons can recombine radiatively or non-radiatively within defect-related levels situated in the forbidden band gap. These levels are called deep centres. Some act as donors and others as acceptors, with energy levels far from the conduction and valence band edges, respectively [27]. The related emission is consequently called “deep level emission (DLE)”.

a) Violet and blue deep level emission

Using PL spectroscopy, Ahn *et al*. [42] investigated the origin of the violet luminescence in ZnO prepared on p-Si substrates by radio frequency magnetron sputtering (RFMS) under different conditions of growth. The thin films were deposited at 680 °C with pure Ar and O_2 gas, and without any low-temperature grown buffer layers. They varied the partial pressures of Ar and O_2 during growth, and observed interesting features in the corresponding luminescence spectra: when the partial pressures of Ar and O_2 during growth were equal, a violet luminescence band centered at 3.1 eV (~400 nm) was measured at low temperatures (<100 K). However, in samples grown with different partial pressures of O_2 and argon, the violet luminescence quenched when the pressure of O_2 was higher than that of Ar. Consequently, the authors concluded that the only possible defect whose concentration could decrease under such growth conditions was Zn_i. This assignment was justified by the assumption that ZnO grown in Ar-rich and extreme O-rich environments by RFMS will predominantly contain Zn_i and (or) V_{Zn} as intrinsic defects. In addition, by taking into consideration predictions from the full potential linear muffin-tin orbital calculations, the violet DLE centered at ~400 nm was attributed to transitions involving Zn_i [42].

Fang *et al.* [43] also studied the source of blue luminescence from ZnO grown by RFMS. ZnO films were produced by sputtering pure zinc metal at room temperature onto silicon substrates with a mixture of O and Ar present in the chamber (the O/Ar pressure ratio equalled 2/3). It was reported that only a blue DLE band centered at 430 nm was observed from as-grown samples. Furthermore, annealing at high temperatures (250 ^{o}C, 600 ^{o}C and 800 ^{o}C) in air for 1 hour resulted in the reduction of the intensity of the blue band, a decrease in the concentration of free carriers and an increase in the resistivity of ZnO films. Based on these observations and on theoretical calculations of the energy levels of intrinsic defects in undoped ZnO films using the full-potential linear muffin-tin orbital method, Fang e*t al.* [43] assigned the blue luminescence to electron transitions from the Zn_i level to the valence band. The assumption made was that the free carrier concentration in ZnO is primarily dominated by electrons generated by oxygen vacancies and Zn_i. Hence, if Zn_i are the source of the blue DLE, a decrease in the concentration of Zn_i will likely be caused by the evaporation of Zn at high temperature and by the diffusion of Zn_i through vacancies left behind by evaporated atoms of Zn [43].

b) Green, yellow and red deep emission level bands

Using PL spectroscopy Børseth *et al.* [33] studied the origin of the green and yellow luminescence bands in hydrothermally grown single crystal ZnO. Samples were annealed in different environments such as air, O-rich and Zn -rich atmospheres, and in the presence of ZnO powder at different temperatures. Annealing in Zn-rich and O-rich atmospheres was performed in sealed quartz ampoules in order to alter the concentration of intrinsic defects. The authors reported that after annealing above 800 ^{o}C in different environments, significant changes in both the peak positions and intensities were observed. The following assumptions were made: “competing non-radiative channels play a negligible role, and the concentrations of optically active defects are homogeneous through the layer”. Experimentally the following results were obtained from PL spectroscopy: an increase in the concentration of V_{Zn} through annealing of ZnO in a Zn-poor environment (this was accompanied by an enhancement of the band centered at 2.35 eV (~527.60 nm)) and an increase in the concentration of V_O through annealing in an O-poor environment (this was accompanied by an enhancement of the band centered at 2.53 eV (~490.06 nm)); a reduction in the concentration of V_{Zn} through annealing in a Zn-rich environment (this was accompanied by a decrease in the intensity of the band centered at 2.35 eV) and a reduction in the concentration of V_O through annealing in an O-rich environment (this was accompanied by a decrease in the intensity of the band centered at 2.53 eV). The authors therefore attributed the 2.35 eV DLE to V_{Zn} and the band at 2.53 eV to V_O. For the samples annealed in the presence of ZnO powder, only a yellow DLE band, centered at 2.17 eV

(~571.36 nm), was observed and attributed to Li, a well-known impurity in hydrothermally grown ZnO [33].

Likewise, Knutsen *et al*. [44] also studied the characteristic of the green and red DLE of melt-grown undoped ZnO using positron annihilation (PA) and photoluminescence spectroscopy. The concentrations of radiative intrinsic defects were altered by means of variable energy electron irradiation and thermal processing in O-rich and Zn-rich environments. One set of samples was subjected to thermal annealing at 800 ^{o}C for 30 minutes in Zn- and O-rich environments, respectively, whereupon several samples were cross annealed (sequentially annealed in different environments), and probed by PL spectroscopy; another set was electron irradiated at 300 K using different energies and fluences, and subjected to PA and to PL spectroscopy studies. The authors reported that annealing in an O-rich environment leads to a significant increase of the DLE intensity compared to the as-grown samples. On the other hand, annealing in a Zn-rich environment caused an overall decrease in the luminescence intensity of the NBE emission, the green DLE band, and the red DLE. However, by swopping the environments, a close to full recovery from the effects first introduced by the initial anneal in oxygen (or zinc) was observed. Additionally, upon electron irradiation, the same green and red bands centered at 2.45 eV (~510 nm) and 1.75 eV (~680 nm) were distinguished. While the green emission gradually quenched with increasing electron energy, the red emission increased, reaching its highest intensity. Based on these observations, Knutsen *et al*. [44] reported that the origin of the two emission peaks is related to single point defects. Specifically, the red band was attributed to V_{Zn} and the green band to V [44].

Gorelkinskii *et al*. [45] studied the in situ diffusion of interstitials created by low temperature electron irradiation at 4.2 K, using PL spectroscopy and optically detected electron paramagnetic resonance. The temperature dependence of defect mobilities from 4.2 K up to room temperature was also reported [45]. The samples studied were undoped ZnO single crystal wafers grown by two methods: chemical vapour transport and a melt process. Irradiation produced new prominent DLE bands centered at 680 nm (~1.8 eV), 750 nm (~1.6 eV) and 900 nm (~1.3 eV). Sequential thirty minute anneals between 110 K and room temperature caused a systematic quenching of the bands centered, respectively, at 750 nm and 900 nm. The authors attributed these observations to the migration of one, or possibly both, of the host interstitial atoms (Zn_i and O_i), because it had been established in previous studies that vacancies are stable in the temperature range studied [45].

In summary, at ambient pressure and temperature, the thermodynamically stable phase of ZnO is the hexagonal wurtzite structure, which has a direct band gap. Calculated and measured energy gaps E_g are 3.437 eV (LDA-SIC-PP) and 3. 3714 eV (ASA–LMTO within the LDA), respectively. It is worth noting that the lowest CB is formed from the empty 4s states of Zn^{2+} or the antibonding sp^3 hybrid states, whereas the VB originates from the occupied 2p orbitals of O^- or from the bonding sp^3 orbitals. Furthermore, the most abundant native defects in ZnO are V_{Zn}, V_O, O_i, Zn_i as well as their related complexes, such as V_OZn_i, etc. It is understood that thermal treatment can activate these defects at different temperatures, depending on the nature of the environment, and that Zn_i and O_i can diffuse at very low temperatures (even below RT). No consensus has been found concerning the origin of the visible luminescence bands in ZnO: the violet luminescence (~400 nm (~3.0 eV)) has been attributed to transitions involving Zn_i and the blue luminescence (430 nm (~2.8 eV)) to electron transitions from the Zn_i level to the valence band. On the other hand, both the DLE bands centered at ~527.5 nm (2.35 eV) and ~680 nm (~1.8 eV) have been attributed to V_{Zn}, while bands at ~490.0 nm (2.53 eV) and ~510 nm (2.45 eV) have been ascribed to V_O. The yellow DLE band, centered at 2.17 eV (~571.36 nm), was attributed to Li, a well-known impurity in hydrothermally grown ZnO. Details of the methods of characterisation used in this study, as well as the reasons for the choice of each method, are provided in the next chapter.

3. GROWTH METHOD AND CHARACTERISATION TECHNIQUES

This chapter briefly describes the growth method used to produce the ZnO nanorods and the characterization techniques employed in this study. The characterization techniques include: X-ray diffraction (XRD), Scanning Electron Microscopy (SEM), Photoluminescence (PL) Spectroscopy, X-ray Photoelectron Spectroscopy (XPS), Auger Electron Spectroscopy (AES), and Secondary Ion Mass Spectrometry (SIMS). The basic theory underlying these characterization techniques is described in each subsection. The necessary calibrations and correction procedures related to the detectors and lenses used in the PL setup are also explained.

3.1. Zinc oxide nanorods synthesis

The growth of nanorods by chemical bath deposition (CBD) consists of two steps: deposition of a ZnO seed layer on a cleaned silicon substrate (001) and growth of the nanorods on the pre-treated substrate. Before the deposition of the seed layer, the substrate was cleaned sequentially using trichloroethylene (TCE), acetone, methanol, and de-ionized (DI) water and blown dry in nitrogen gas. A well agitated ethanolic solution made of 5 mM of zinc acetate dihydrate ($Zn(CH_3COO)_2{\bullet}2H_2O$) and 0.01 g of polyvinylpyrrolidone (PVP) was spun five times onto the pre-cleaned substrate using a spin coater. The spin rate and spin time were, respectively, 3000 revolution per minute and 30 seconds. Then the spin coated substrate was annealed in an oxygen environment for 30 min at 300 ^{o}C at atmospheric pressure. This spin coating and annealing process was repeated twice in order to control the density of the seed layer. For the formation of the nanorods, the seeded substrate was immersed into the growth solution, which was a mixture of aqueous solutions of zinc nitrate hexahydrate ($Zn(NO_3)_2{\bullet}6H_2O$)) and hexamethylenetetramine (hexamine) ($C_6H_{12}N_4$). The Table V summarises the measured pH during and after growth of the growth chemical solutions as function of temperature. It can be seen that the ZnO nanorods grew in an acidic environment at ~85 ^{o}C. The growth step lasted 90 minutes at a temperature of 85 ^{o}C. The precursors, zinc acetate dihydrate, zinc nitrate hexahydrate and hexamine were obtained from Sigma Aldrich, and used as received. The zinc nitrate hexahydrate contained less than 50 mg/kg of Ca, Cd, Co, Cu, Fe, Cl, Ni and Pb, and also less than 100 mg/kg of sulfate, K and Na. The solvents used were ethanol (98%) and doubly de-ionized (DI) water ($\rho = 18.2$ MΩ.cm).

Table V. Summary of the measured temperature and pH of the chemical bath in which ZnO nanorods were deposited, both during and after growth.

Chemical solution		***Temperature (^{o}C)***	***pH***
Hexamethylenetetramine 0.1 M		22.5	7.53
Zinc nitrate 50 mM		22.4	4.93
Hexamethylenetetramine (0.1 M) and Zinc nitrate 50 mM mixed together.	During growth	61.2	5.66
		68.8	5.77
		70.8	5.73
		75.4	5.65
		80.5	5.57
		84.7	5.51
	After growth	45.2	5.98
		35.0	6.16
		29.0	6.38

3.2. X-ray diffraction

X-ray diffraction (XRD) is a powerful non-destructive technique for characterizing crystalline materials. In this study, the technique has been used in order to determine the crystalline quality of the solution grown ZnO nanorods on Si substrate. The type of phases present and the orientation of the rods with respect to the substrate surface were also determined from the analysis.

X-rays directed onto a sample are scattered elastically by the electronic clouds of atoms present in the material. If the material is crystalline, this elastic scattering results in signal maxima and minima in the diffracted intensity spectrum according to Bragg’s law:

$$n\lambda = 2d\sin\theta \tag{3.1}$$

The parameter n is an integer (1 in the present case), λ the wavelength of the X-ray beam, d the distance between crystal lattice planes and θ the diffraction angle. Fig. 3.1shows a 2-dimensional scattering scheme of X-rays by a crystalline material.

During an XRD scan, the angles of incidence and detection, often known as 2θ, are scanned. Hence, an X-ray diffraction pattern is obtained when the intensities of the detected X-rays is plotted as a function of angle θ. The observable series of peaks in intensity are due to constructive interference of diffracted waves from different layers constituting the lattice. In this study, a Bruker D8 Discover X-ray Diffractometer with a Cu-$K\alpha$ x-ray source (λ = 1.5405 Å) was used. No filter was used.

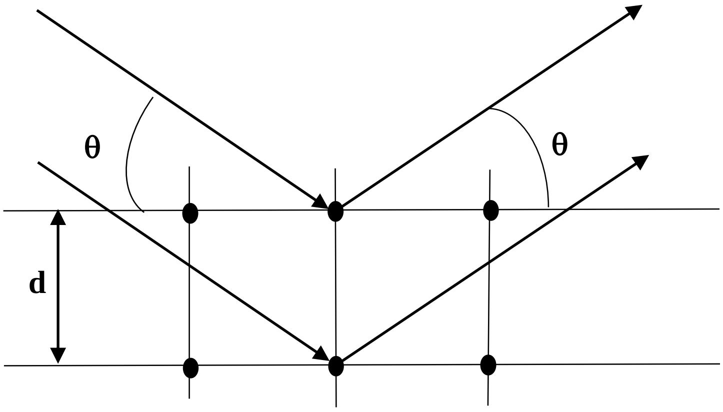

Figure 3.1. Schematic representation of diffraction of X-rays in a crystalline material.

3.3. Scanning Electron Microscopy

In order to investigate the morphology, amongst other details, of the nanorods, Scanning Electron Microscopy (SEM) was used. This technique is non-destructive and is commonly used for surface analysis.

In SEM an electron beam is used to trace over the sample, creating an exact replica of the original sample on a monitor giving a 3-dimensional image. The beam of electrons is controlled by means of scanning coils, which create a magnetic field using a fluctuating voltage in order to manipulate the electron beam direction and to focus it on the desired section of the sample [46]. The smaller the selected section is, the bigger the magnification will be. The interaction of the beam of electrons with the surface of the sample results in a variety of particles (radiation) such as backscattered and secondary electrons, characteristic x-rays, continuous x-rays, and Auger electrons [46]. A suitably-positioned electron detector and other sensors detect most of these scattered particles and, depending on the number of detected particles from a particular feature of the object, the levels of brightness on a monitor are set. A Jeol JSM-7001F Field Emission SEM (FESEM) has been used in this study.

3.4. Photoluminescence Spectroscopy

Due to the fact that PL spectroscopy is a very efficient, contactless, and non-destructive characterisation technique, it has been used for the analysis of optical properties of semiconductors materials for many years, especially in the detection of defect and impurity levels involved in the radiative emission.

A preliminary investigation of the optical properties of ZnO was conducted using a mini-PL UV Laser System 5.0 (Photon Systems, USA), which employs a NeCu laser with excitation wavelength of 248.6 nm. Throughout the text it will be called “Mini PL”. However, due to the fact that this Mini PL is less sensitive to visible and near infrared light than to UV light, another PL system which is sensitive to the entire spectrum, from the UV to the near infrared range, was used. This second PL system will be called “Big PL”. The schematic diagram of the “big PL” is shown in Fig. 3.2; it consists of the following major parts: a 325 nm He-Cd laser source (cw), a chopper, a set of lenses and mirrors, a computer controlled monochromator equipped with a photomultiplier tube and a lock-in amplifier.

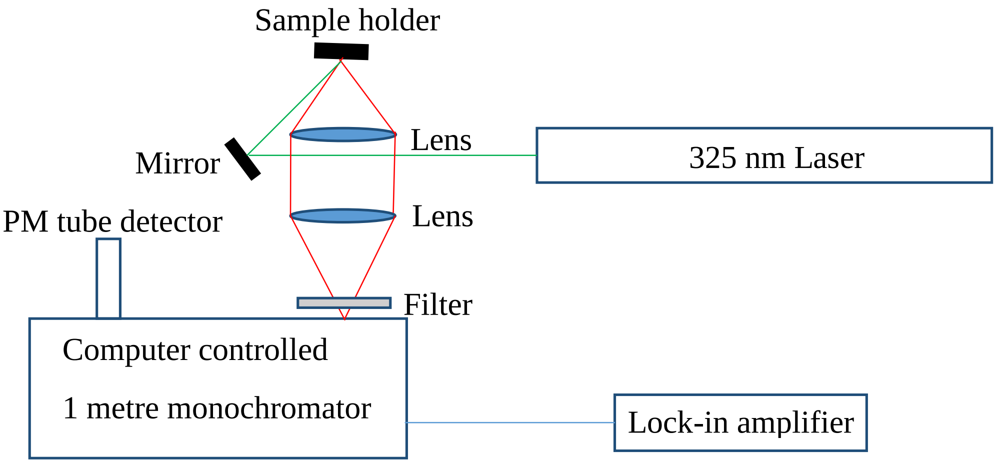

Figure 3.2. Schematic diagrams of the experimental set-up for PL measurements using a photomultiplier tube (PM Tube).

A sample is excited by a focused laser beam that has energy greater than the band gap of the sample. The collected emissions, focused onto the entrance slit, are measured as a function of wavelength (or energy). The luminescence was filtered with high pass filters (GG385 and KV450) depending on the wavelength range of interest, in order to avoid artefacts stemming from laser radiation and higher order diffractions. The main part of the PL spectrometer that makes possible this measurement is the monochromator, which is equipped with detectors that are sensitive in the wavelength range of interest. The detected signal was amplified with a lock-in amplifier connected to a mechanical chopper.

Laser specifications

Based on the band gap of ZnO, which is around 3.37 eV (~367.9 nm) at RT (24) (13), an IK-series He-Cd laser source (from KIMMON) with a wavelength of 325 nm (3.9957 eV) was used as an excitation source. It has 15 mW of initial power and a beam diameter of 1.2 mm. Fig. 3.3a shows the penetration depth of ZnO as function of the excitation wavelength. From a transmission measurement for high quality single crystal epitaxial zinc oxide thin films grown by pulsed laser deposition on c-plane sapphire substrates determined by Muth *et al.* [47], the room temperature absorption coefficient α(λ) for ZnO is shown as insert in fig. 3.3(a). From this graph the penetration depth profile for ZnO at room temperature as a function of wavelength is shown in fig. 3.3(a). From this figure the penetration depth for the He-Cd laser source (325 nm laser) is ~63 nm. As compared to the length of the nanorods in this study (about 1.1 µm, see the typical cross-sectional image shown in fig. 3.3(b)), the penetration depth is only ~ 6 % of the average length of the rods.

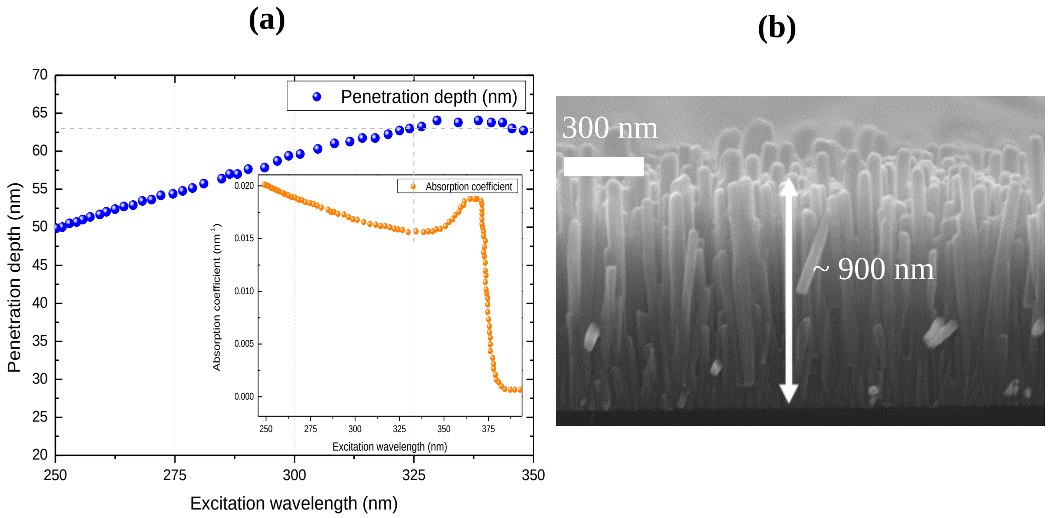

Figure 3.3. (a) Penetration depth of ZnO deduced from the work of Muth *et al*. [47]; (b) cross-section SEM image of ZnO nanorods.

Monochromator specifications

A monochromator of high accuracy (Horiba FHR1000), throughput and resolution has been used in order to scan over a wide spectral range, extending from the UV range to the near IR. Table VI shows key specifications of this monochromator when it is equipped with a 1200 grooves/mm (gr/mm) grating. Due to the fact that the visible and near IR emission are the wavelength range of interest, the following gratings have been carefully chosen: a 1800.48 gr/mm grating of 400 nm blaze wavelength and a 1200.28 gr/mm grating of 750 nm blaze wavelength. They are more efficient, respectively, in the following wavelength ranges: ~270-720 nm and 500-1350 nm. For the remaining discussion these gratings are called grating 1 and 2, respectively.

Table VI. Monochromator specifications

Focal length	1 m
Grating size	80 mm × 110 mm
Wavelength position accuracy	±0.03 nm
Scanning range	0-1500 nm

To complete the setup, a suitable detector that is sensitive over the mentioned extended range of wavelengths was used: a Hamamatsu R3896 photomultiplier tube (PMT) with a GaAs photocathode.

Spectral sensitivity of the system

The spectral sensitivity of the various system components had to be calibrated in order to correct the measured PL spectra. In order to do this, the radiation from a quartz tungsten halogen lamp (50 W QTH - short filament – colour temperature 3300 K) was scanned using the PM tube and all possible combinations of the gratings and high pass filters mentioned above. The measured spectra were normalised and compared to the calculated black body spectrum (for a source with colour temperature of 3300 K) in the same wavelength range of the scan. The final calibration curves (normalised blackbody spectrum divided by measured spectrum for the tungsten lamp) are given in fig.3.4. Fig 3.4a shows the calibration curve for the PL system with grating 1 and with the GG385 filter used. When grating 1 is replaced by grating 2, the calibration curve is shown in fig3.4b. Fig 3.4c shows the calibration curve when grating 1 and the KV450 filter are used. Again when grating 1 is replaced by grating 2 the relevant calibration curve is shown in fig 3.4d. Dotted lines in fig. 3.4c and d show the cut-off wavelengths of the filters used.

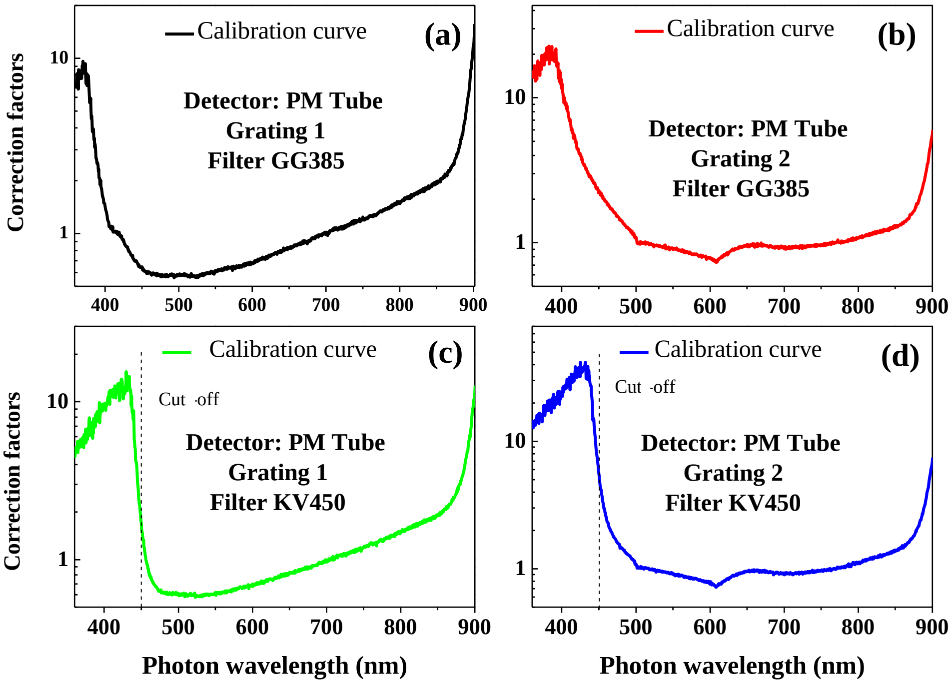

Figure 3.4. (a) Calibration curves for the PL set-up including the PM tube, grating 1 and GG385filter, (b) PM tube, grating 2 and GG385filter, (c) PM tube, grating 1 and KV450 filter, and (d) PM tube, grating 2 and KV450 filter.

All other optical components were kept the same during these measurements. The measured PL spectra were multiplied by these calibration curves in order to obtain corrected results. Moreover, in order to avoid over correction, correction factors exceeding 10 were not taken into account.

3.5. X-ray Photoelectron and Auger Electron Spectroscopy

In order to investigate the formation of different kinds of surface-related defects, to identify surface-adsorbed impurities in ZnO, and to study the effect of annealing temperature and environment, X-ray Photoelectron (XPS) and Auger Electron Spectroscopy (AES) were used. The investigations were accomplished by irradiating a sample with either mono-energetic soft X-ray photons (XPS) or an electron beam (AES) and analysing the electrons emitted after the interaction between the primary beams and the sample. Therefore, atoms in the sample are ionised, and electrons are liberated from the surface, either as a result of the photoemission process (XPS), or of the Auger electron emission process (AES). The photoelectric process and Auger process are schematically illustrated in fig. 3.5 for the emission of an electron from the 1s shell of an atom. Electrons leaving the sample are detected by an electron spectrometer. Specifically, the analyser functioning as an energy window accepts only electrons that have the energy fixed within its range of detection referred to as the pass band. Then the number of electrons detected for a given detection time and given is stored and digitally treated.

On one hand, photoelectrons are emitted with the following kinetic energy [48, 49]:

$$KE = h\nu - BE - \phi , \tag{3.2}$$

where $h\nu$ is the energy of the incident photon (X-ray), BE is the binding energy of the atomic orbital from which the electron originates, and ϕ represents the spectrometer work function, which is to a first approximation the difference between the energy of the Fermi level and the energy of the vacuum level.

On the other hand, Auger electrons are emitted due to relaxation of the energetic ions left after photoemission. In this process, in fig. 3.5b, an outer electron falls into the inner orbital vacancy, and a second electron is emitted, carrying off the excess energy. The kinetic energy (KE) of Auger electrons is equal to the difference between the energy of the initial ion and the doubly charged final ion. The KE is independent of the mode of the initial ionisation. The amount of electrons escaping from the sample without energy loss is typically measured. The data is represented as a graph of intensity against electron energy and the pattern exhibits several types of peaks, some being fundamental to the technique and others depending upon the exact physical and chemical nature of the sample [50]. A quantitative analysis of obtained spectra reveals the identity of adsorbed impurities in ZnO and provides the sample stoichiometry ratios using the following relationship:

$$S_{i,j} = \frac{C_i}{C_j} = \frac{I_i / S_i}{I_j / S_j} \tag{3.3}$$

where C_i and C_j are the concentrations of the identified elements, I_i and I_j the background corrected intensity of the photoelectron peaks, and S_i and S_j the atomic sensitivity factors for photoionization of the i^{th} and j^{th} elements. This formula is only valid for homogenous elemental distributions in the sample [50].

The system used for X-ray Photoelectron analysis is a “PHI 5000 Versaprobe-Scanning ESCA Microprobe”. XPS surveys were done with a 100 μm diameter, 25 W, 15 kV Al monochromatic X-ray beam, and sputtering processes were done with an Ar ion gun (2 kV, 2 µA beam, 1x1 mm raster area) at a rate of about 18 nm/min. The X-rays penetrate the sample up to 2 µm in depth, but the detected photoelectrons come from the first 3 to 5 monolayers from the surface. The Auger electron system used is a "PHI 700 Scanning Auger Nanoprobe". AES surveys were done with 25kV and (1 or 10) nA electron beam, using an Ar ion gun (2 kV, 2 µA beam, 1x1 mm raster area) at a rate of about 22 nm/min. Line profiles were done with an electron beam of 25 kV and 10 nA. The energy resolution of both instruments is of 0.5 eV and the margin of absolute error for the detector of photoelectrons and Auger electrons from an angle of incidence of 45 degrees is 2 %.

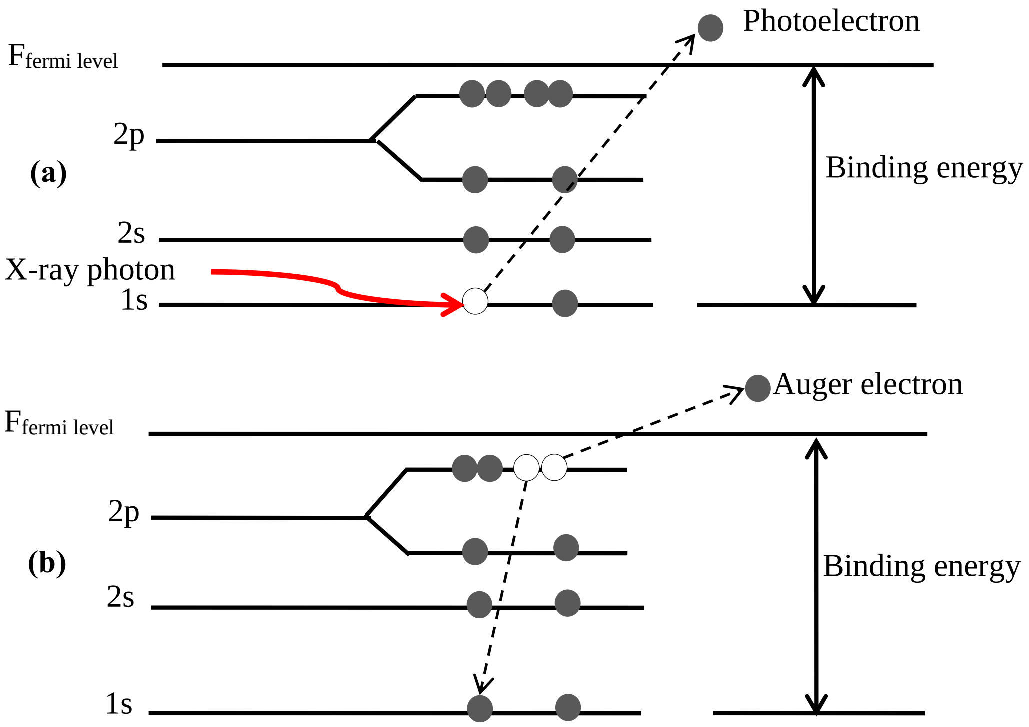

Figure 3.5. Schematic representation of (a) the photoelectric process and (b) Auger process.

3.6. Secondary Ion Mass Spectrometry with Time of Flight mass analysis

Further analysis of the non-modified surface composition of ZnO nanorods, and the depth profile surveys have been done by Secondary Ion Mass Spectrometry (SIMS) with Time of Flight mass analyser (ToF). ToF-SIMS is a destructive technique of characterisation, because particles are removed from atomic monolayers on the surface.

During ToF-SIMS analysis, a solid surface is bombarded by primary ions of some keV energy in order to trigger an outgoing scattering of surface atoms and molecular compounds called "secondary ions". The primary ion energy is transferred to target atoms via atomic collisions and a collision cascade is generated. Most of the emitted particles carry negative, positive, and neutral charges. The dimensions of the collision cascade are rather small and particles are emitted within an area of a few nm in diameter. The secondary ions formed are then accelerated by an electrostatic field to a common energy and travel over a drift path to the detector through ToF mass spectrometry. Normally the sample is at ground and the tip of the accelerator is set either at a positive or negative voltage. If this voltage is positive only negative secondary ions will be accelerated; if it is the opposite, positive secondary ions will be accelerated. For both types of secondary ions (positive or negative), the lighter ones arrive before the heavier ones and a mass spectrum is recorded, while for each ion the measured flight time is recorded for the determination of its mass. During the drift time of the secondary ions, the extraction field is switched off and low energy electrons are used to compensate for any surface charging caused by primary or secondary particles.

The ToF-SIMS set up used is the same as in [19]. It is worth noting that depth profile investigations were done at ultra-high vacuums of ~ 10^{-8} mbar for positive secondary ion polarity and 10^{-9} mbar for negative secondary ion polarity. In order to acquire ion distributions in 2D and 3D, a 30 keV pulsed Bi^{1+} ion beam (~5 µm diameter) with a frequency of 10 kHz, and ~1 pA (30 nA DC) target current ion in spectroscopy mode were used. Only an area of 100 x 100 μm^2 was analysed from a 300 x 300 μm^2 sputter area in order to avoid edge effects. Sputtering was done in the positive mode by an oxygen gun (1kV, 250 nA) and in the negative mode by a cesium gun (2kV, 130 nA). All surface-sensitive experimental results for solution-grown ZnO nanorods are presented and discussed in the next chapter.

4. RESULTS AND DISCUSSION

As discussed in subsection 2.3.3, ZnO grown by various methods exhibits different visible luminescence (green/yellow/orange/red) bands at RT. In this regard, the main quest of this chapter is on the understanding of the origin of the luminescence properties of ZnO nanorods grown by CBD. The term “nanorods” will be frequently used in the place of “ZnO nanorods”. Different characterisation techniques described in the previous chapter are employed. In particular, the effect of annealing temperature and environment on the optical and structural properties, chemical composition and surface adsorbed impurities are examined using PL, XRD, XPS, AES, and ToF-SIMS. Section 4.1 gives a brief description of the nanorod growth and annealing experiments. Section 4.2 presents the results from each of the characterization techniques employed.

4.1 Sample preparation and annealing experiment description

As described in section 3.2, the nanorods were grown by chemical bath deposition (CBD) on 2×2 cm^2 silicon substrates. After growth the nanorods were cleaned with DI water and blown dry in nitrogen gas. For further treatment and different investigations the samples were cleaved into several pieces and kept in clean non-sealed containers. Annealing experiments were conducted in a horizontal quartz tube at different temperatures and in different environments at atmospheric pressure. Controlled flows of Ar, N_2, O_2, and a mixture of Zn vapour and Ar were used to create the desired annealing environments.

4.2 Results and discussion

4.2.1 Effect of annealing temperature and environment on the morphological properties using Scanning Electron Microscopy

As-grown nanorods

Fig. 4.1 shows top view SEM micrographs of as-grown nanorods at different magnifications. In fig. 4.1a relatively large area is shown, whereas fig.4.1b presents an image taken at higher magnification. It can be seen from these micrographs that the rods are uniformly distributed on the substrate and exhibit a hexagonal shape.

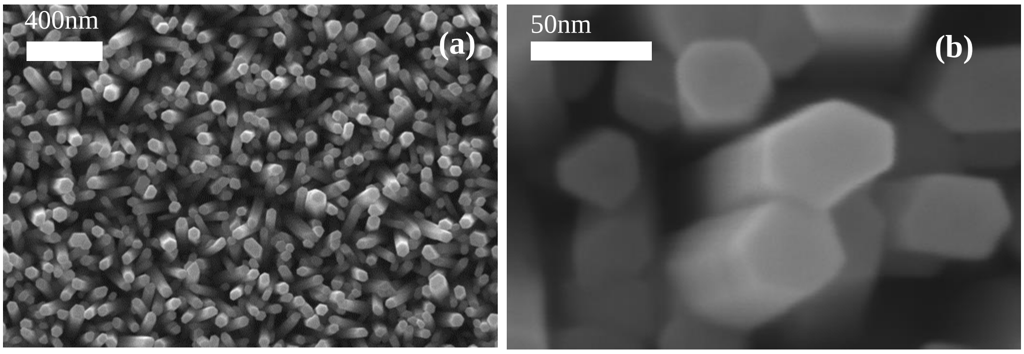

Figure 4.1. Top view SEM micrograph of as-grown ZnO nanorods at different magnifications; (a) lower magnification image; (b) higher magnification.

The average "corner-to-corner diameter" and "flat side-to-flat side diameter" are, respectively, ~52 nm and ~40 nm. Depending on the precursor concentration used, Urgessa *et al.* showed that ZnO nanorods grown using the same method can have diameters ranging from ~30 to ~150 nm [51].

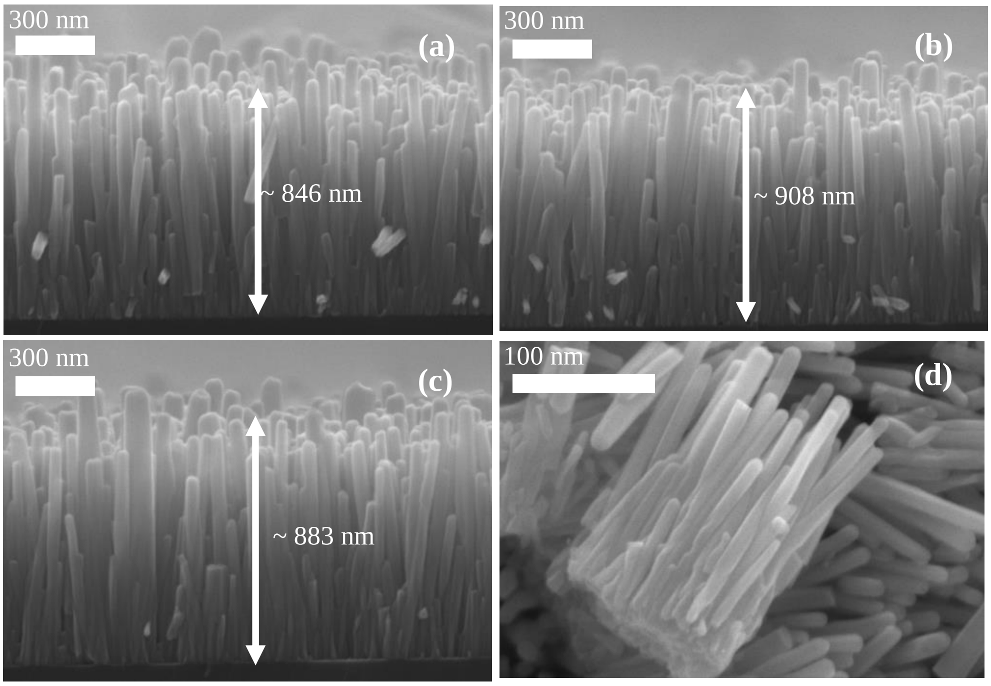

Figure 4.2. (a-c) Cross-sectional SEM views of ZnO nanorods taken from randomly chosen regions of an as-grown sample. (d) Cluster of nanorods broken off from the substrate.

Cross-sectional SEM views, randomly chosen from different regions of an as-grown sample are shown in fig. 4.2. Fig. 4.2a-c illustrate the average length of the rods and their orientation with respect to the substrate. As can be seen from these micrographs, the average length is ~900 nm and the nanorods are reasonably well aligned perpendicular to the substrate. As reported by Urgessa *et al*. [51], the length of the nanorods depends on the concentration of the precursors used. Fig. 4.2d shows a cluster of nanorods broken off from the substrate during cleaving. It illustrates that the rods are attached to one another at their base (close to the substrate) and are more sparsely spaced towards the top surface of the sample (see fig. 4.1b). The formation of nanorods attached at the base is caused by the high density of the seed layer coating prior to the growth of the nanorods [13]. As indicated in reference [51] a high density seed layer yields thin films on the substrate.

Effect of annealing temperature and environment (N_2 and O_2)

In this section the effects of annealing in controlled flows of N_2 and O_2 at different temperatures for 30 minutes are presented. Two different sets of samples cleaved from the same reference were used and each sample was annealed at a different temperature. Note, therefore, that each sample was annealed once and not sequentially.

High magnification, cross-sectional SEM micrographs of nanorods annealed in N_2 and O_2 at 300 ^{o}C, 600 ^{o}C, and 850 ^{o}C are shown in fig. 4.3. The effect of annealing at lower temperature (300 ^{o}C) in N_2 and O_2 are shown in fig.4.3a-b, respectively. The case of samples annealed at 600 ^{o}C in N_2 and O_2 are shown in fig. 4.3c-d respectively, while samples annealed at higher temperature (850 ^{o}C) in N_2 and O_2 are depicted in fig. 4.3e-f, respectively. Regardless of the annealing environment there are no noticeable morphological changes for sample annealed at temperatures up to 600 ^{o}C (see fig. 4.3a-d). However, from fig.4.3e-f, it can be seen that morphological properties changes significantly after annealing at 850 ^{o}C. In particular, voids can be seen at the interface with the substrate. Although the melting point of ZnO is 1975 ^{o}C, the rods appear to have “melted” into one another. The large voids at the interface may be due to vacancy formation and migration, as well as a form of Ostwald ripening causing neighbouring rods to merge. Annealing at higher temperatures affects the morphology of the rods irrespective of the chosen annealing environment. In the next section, XRD results will be discussed as function of annealing temperature.

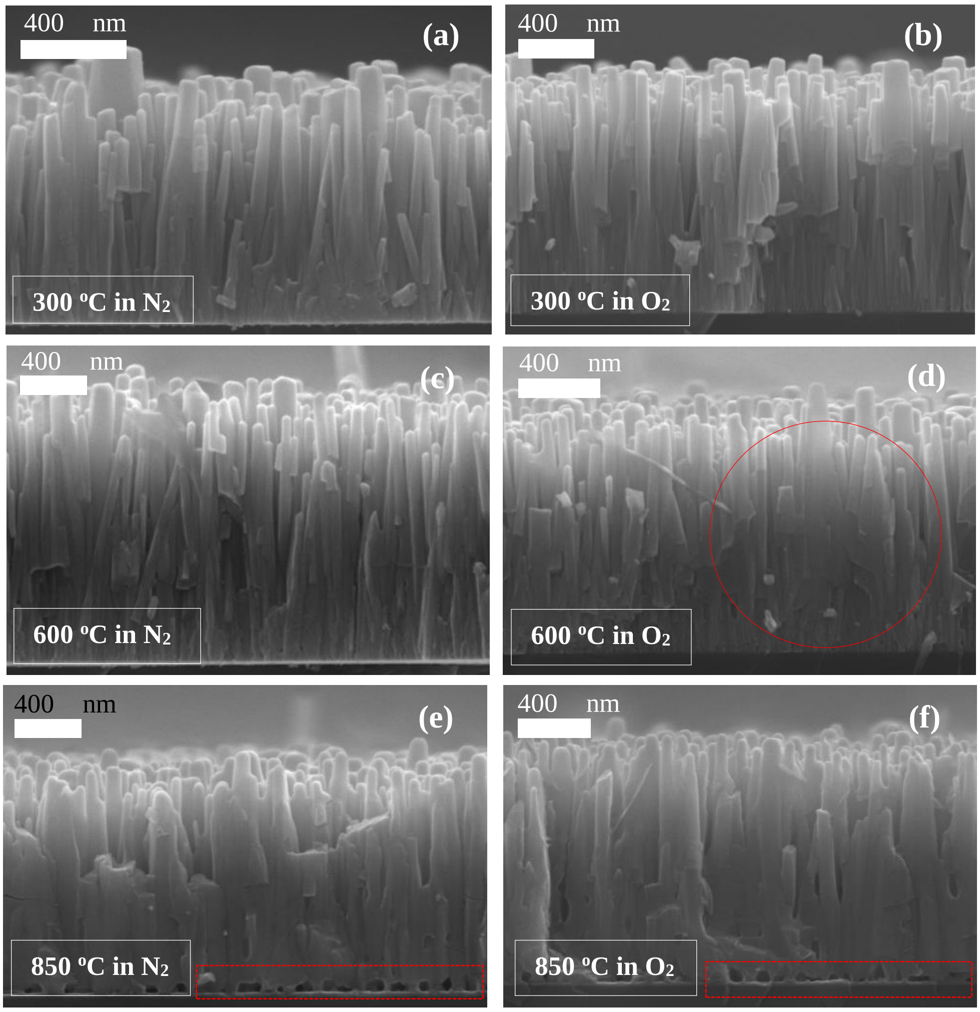

Figure 4.3. Cross-sectional SEM micrographs of ZnO nanorods annealed in N_2 and O_2 at different temperatures. The annealing temperature and environment are shown on each image.

4.2.2 X-ray diffraction of annealed samples

In order to inspect the effect of annealing on the crystallinity of the nanostructures, an XRD study was conducted as a function of annealing temperature. For this study, a 2 cm x 1 cm sample was prepared on Si substrate. The XRD spectrum of the as-grown sample was recorded as a reference. It was then annealed at 300 °C for 30 min in flowing O_2 gas and the XRD spectrum was retaken. Similarly, the XRD spectrum was recorded after sequential anneals (30 min; flowing O_2) of the same sample at 500 °C, 600 °C, 700 °C and 850 °C. With sequential annealing it was possible to trace by XRD the effect of temperature on the phase and crystallinity of the nanorods. Results from a similar XRD investigation of nanorods annealed in N_2 are not reported here due to their similarity to XRD results from the sample annealed in O_2.

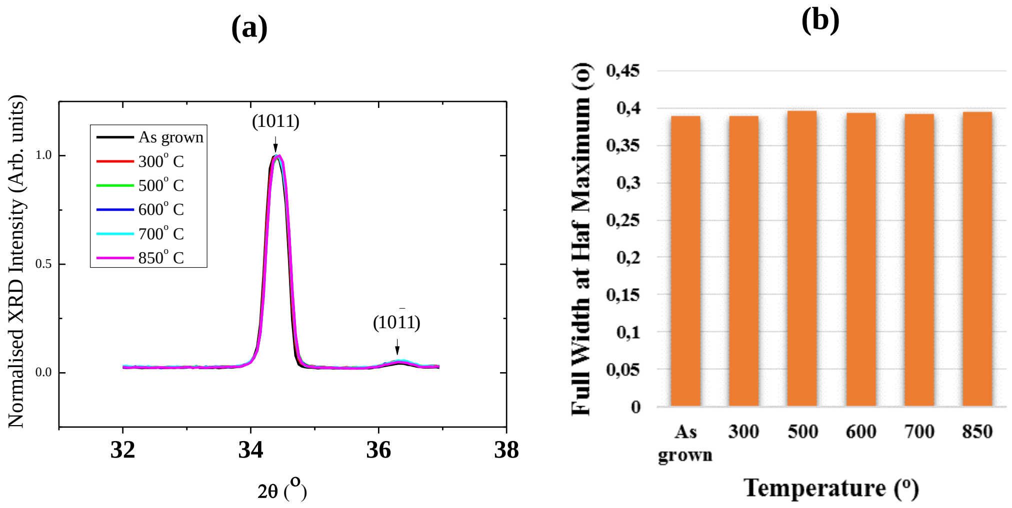

Figure 4.4. (a) Normalised XRD spectra of ZnO nanorods annealed in oxygen at different temperature for 30 minutes. (b) Full width at half maximum of the (0002) peak as function of annealing temperature.

Fig. 4.4a presents normalised XRD spectra of a sample, as-grown and sequentially annealed at 300 °C, 500 °C, 600 °C, 700 °C and 850 °C for 30 min in O_2. Irrespective of the annealing temperature, a strong diffraction peak at 34.4° 2θ from the (0002) plane of wurtzite ZnO is observed, as well as a peak from the (10$\bar{1}$1) plane of ZnO (at2θ = 36.25°). In addition, the full widths at half maximum (FWHM) of the (0002) diffraction peak presented in fig. 4.4b show no change upon annealing. Hence, annealing under the present conditions has no noticeable effect on the crystal orientation or crystallinity of the nanorods. Furthermore, there isn't any significant shift in the position of the (0002) peak, the spacing between adjacent (0002) lattice planes is found to be unaffected by annealing.

In summary, the ZnO nanorods are reasonably well aligned with the c-axis perpendicular to the substrate, and having an average corner-to-corner diameter, flat side-to-flat side diameter and average length of ~52 nm, ~40 nm and 900 nm, respectively. Annealing above 850 °C for more than 30 minutes degrades the nanorods. Regardless of annealing environment there is no noticeable morphological change for nanorods annealed at temperatures up to 600 °C. The morphological properties are affected by a 30 minute thermal treatment at high temperature. However, the SEM and XRD experimental results show that under the specified annealing conditions, the orientation of the nanorods does not change. In the next section, experimental results related to surface defects and impurities adsorbed on the nanorods are discussed, as well as the effects of annealing temperature and environment on these.

4.2.3 Surface chemical characterisation

As described in section 3.5, both XPS and AES are surface sensitive analytical techniques. For these experiments samples cleaved from the same reference were annealed in different environments and the results from annealed samples are compared with those of the as-grown sample. The annealing temperatures were 300 ^oC, 600 ^oC, and 850 ^oC and the annealing time was 30 minutes. Note that annealing was not sequential. It is also worth noting that both XPS and AES studies were not performed in-situ. Hence, recontamination of the surface from the ambient environment during transferring the annealed samples from the annealing furnace to the XPS or AES facility was inevitable. In an attempt to circumvent this problem, the sample surfaces were Ar-sputtered and for both XPS and AES measurements, spectra were recorded before and after sputtering. Samples characterised by XPS were sputtered for 30 seconds at a rate of 18 nm/min, whereas those characterised by AES were sputtered for 1 minute at a rate of 22 nm/min. All detected photoelectrons and Auger electrons originated from approximately the first 3 to 5 monolayers from the surfaces of the rods (see section 3.5). In the case of XPS depth investigations were carried out parallel to the c-axis (i.e. from the top) of the samples, whereas the AES measurements were performed on the "cleaved sides" (perpendicular to the c-axis) of the samples. Samples were all kept in non-sealed containers (for 12 hours) before commencement of the XPS and AES investigations.

4.2.3.1 X-ray photoelectron spectroscopy

<u>XPS survey results</u>

As shown earlier by the XRD investigations, the majority of nanorods are oriented perpendicular to the substrate. Consequently, according to the XPS system configuration, photoelectrons are expected to originate mostly from the top surfaces of the nanorods. This situation is illustrated in fig. 4.5, showing the part of nanorods that was characterised by XPS. XPS scans were not done on a single nanorod, naturally, but rather on a multitude of rods within the beam diameter of 100 µm.

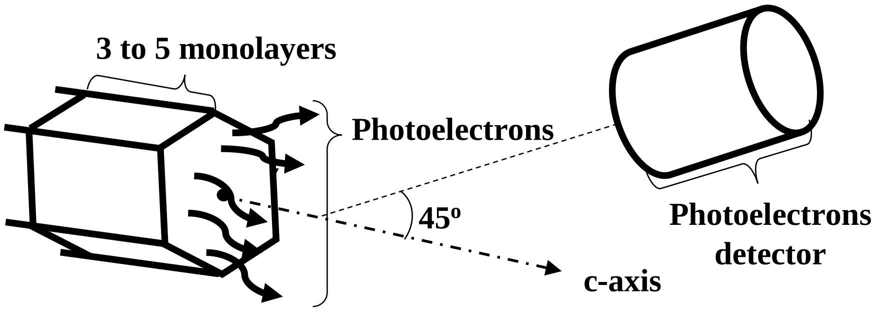

Figure 4.5. Sketch of the top view of a nanorod showing approximately the part of a rod from which photoelectrons electrons originated. The angle of detection was ~45°.

As-grown nanorods

Fig. 4.6a-b show XPS survey scans from as-grown nanorods both before and after sputtering. In fig. 4.6a the binding energy peaks can only be ascribed to carbon (C), Zn and O, as labelled. But after removing a surface layer of ~9 nm by sputtering, it can be seen in fig.4.6b that the carbon-related signature is below the detection limit. This implies that most of the C-related contaminants are surface-related and adsorbed from the ambient atmosphere and/or from the growth solution. Thus, C is the dominant impurity on the surface of the as-grown sample.

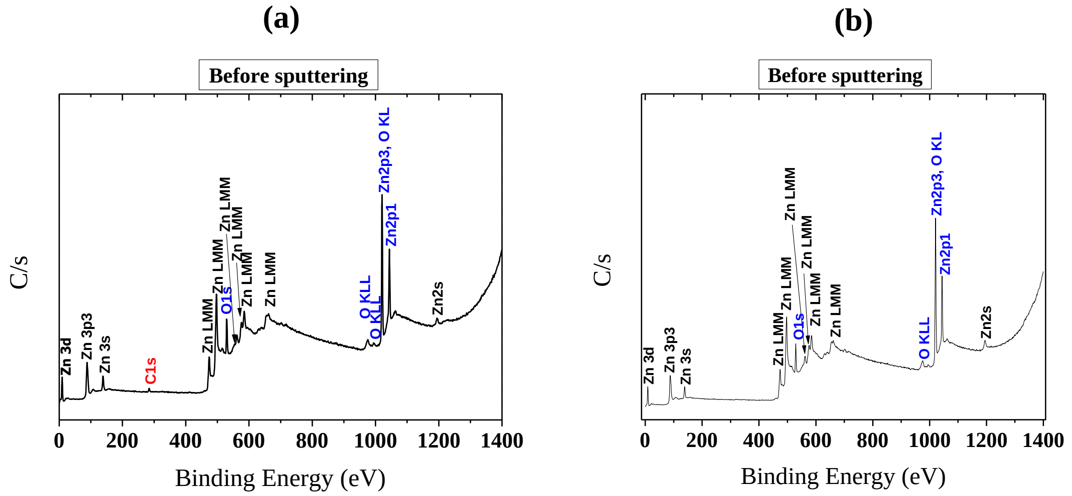

Figure 4.6. Broad XPS survey scans on the as-grown sample surface: (a) before sputtering and (b) after sputtering. The labels on each spectrum indicate the origins of the corresponding peaks.

Annealed nanorods

The XPS results of samples annealed in N_2 at different temperatures are shown in fig. 4.7. Fig. 4.7a-b, c-d, and e-f present representative broad XPS survey scans of samples after annealing, respectively, at 300 °C, 600 °C, and 850 °C. As in the case of the as-grown sample, in all the annealed samples carbon is observed before sputtering and is subsequently removed by the sputtering process, indicating that C is actually absorbed from the ambient during the transferring of the annealed samples to the XPS facility. In addition to Zn, O and C the XPS spectra for the samples annealed at 600 °C and 850 °C (fig. 4.7e-f) also indicate the presence of Si.

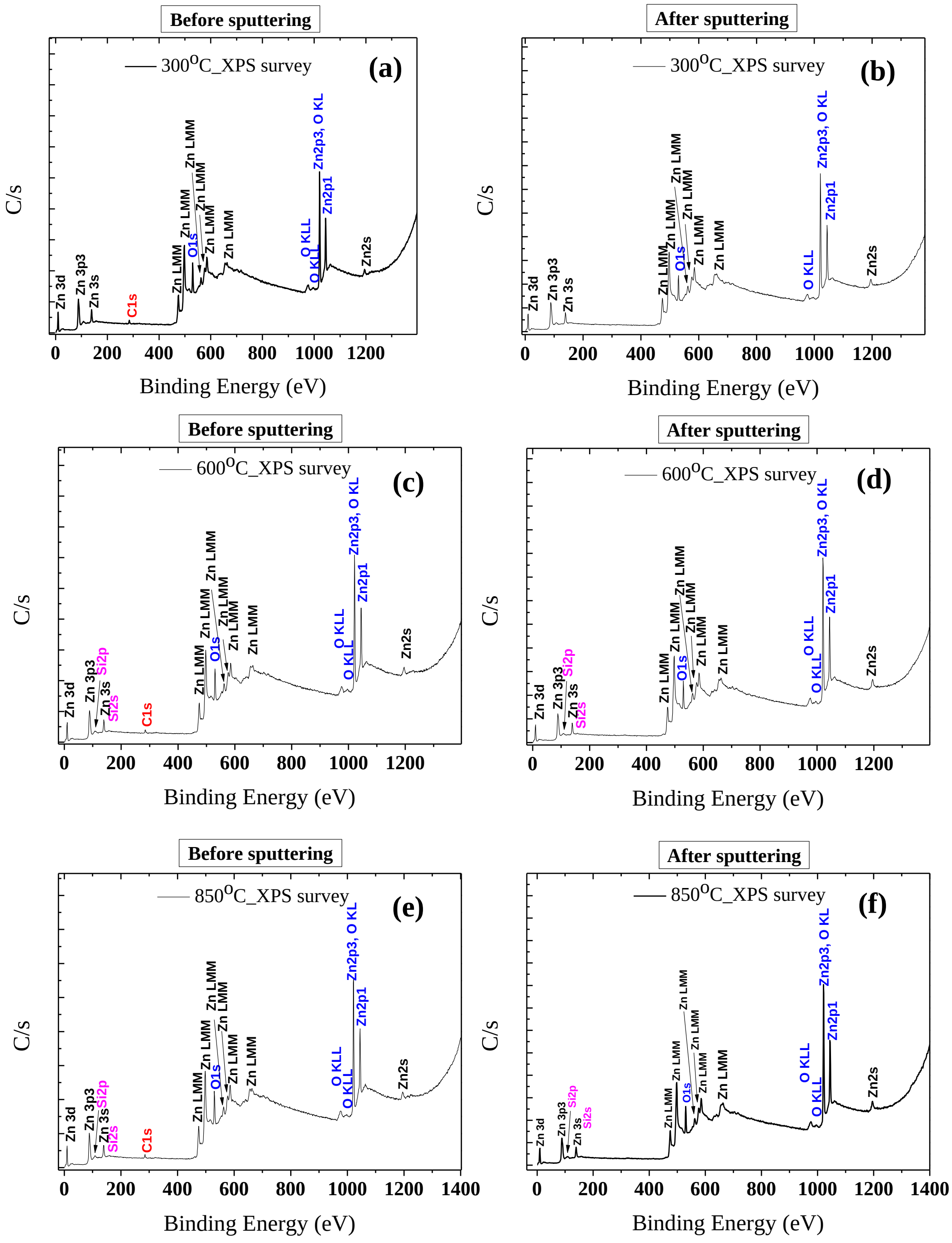

Figure 4.7. XPS survey spectra before and after sputtering of nanorods annealed in N_2 at 300 °C (a-b), 600 °C (c-d), and 850 °C (e-f). The labels indicate the elemental origin of the corresponding peaks.

Fig. 4.8 presents XPS survey scans, before and after sputtering, of samples annealed in O_2. Fig. 4.8a-b, c-d, and 24e-f were obtained from samples annealed at 300 °C, 600 °C, and 850 °C, respectively.

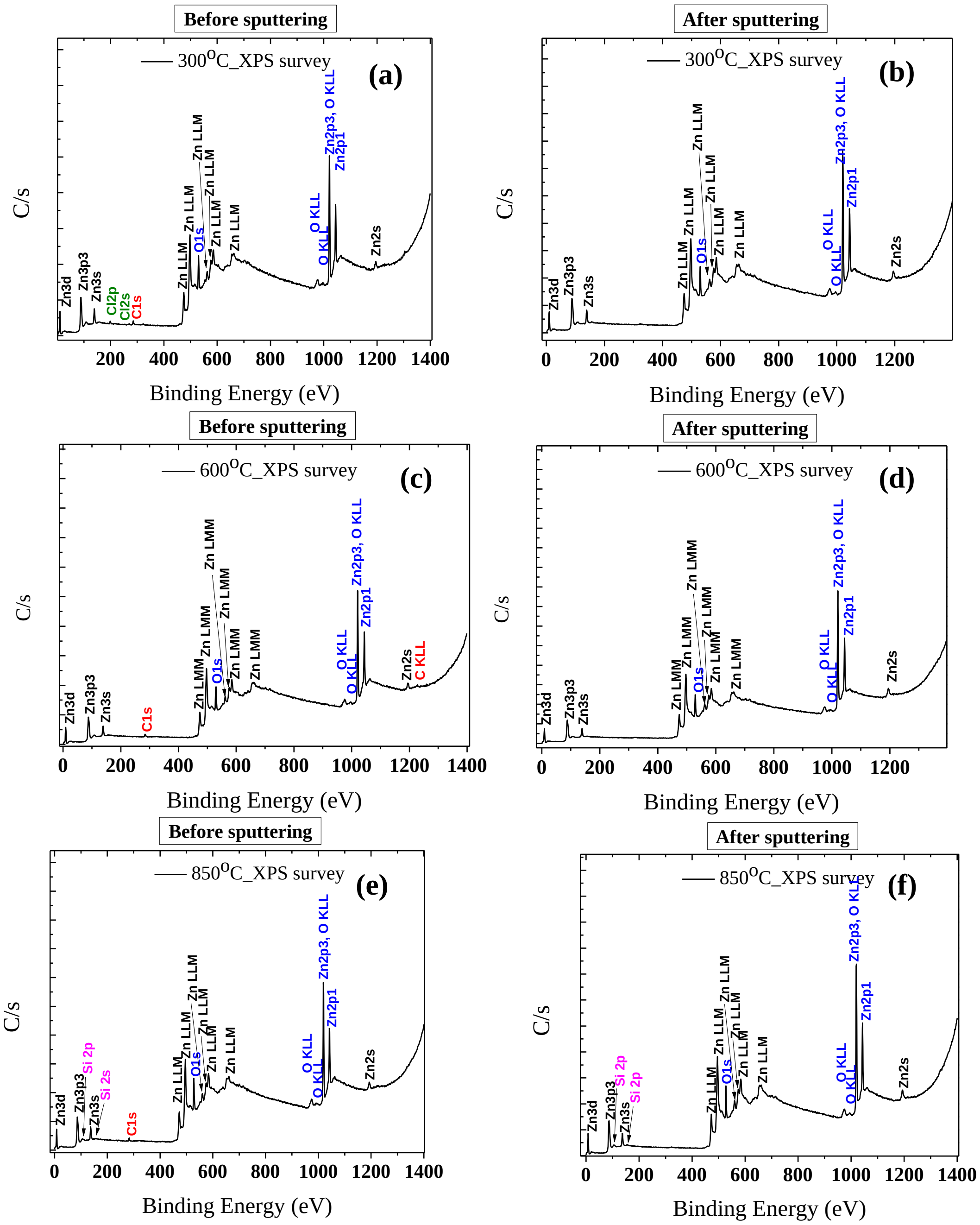

Figure 4.8. XPS survey spectra before and after sputter of samples annealed in O_2 300 °C (a-b), 600 °C (c-d) and 850 °C (e-f). The labels indicate the origins of the corresponding peaks.

Like in the case of samples annealed in N_2, XPS survey scans from samples annealed in O_2 reveal the presence of the same elements, namely O, Zn and C (before sputtering). The only exception is the detection of chlorine (Cl) in the sample annealed at 300 °C. Since this element is removed from the surface by sputtering, Cl is counted among the surface impurities. Chlorine is probably incorporated during growth, since the zinc nitrate hexahydrate (Zn $(NO_3)_2 \cdot 6H_2O$)) and hexamethylenetetramine (hexamine) ($C_6H_{12}N_4$) used as precursors contained 50 mg/kg of Cl and 100 mg/kg of sulfate (see section 3.1). At higher temperature (850 ^oC), the presence of Si was again detected before and after sputtering (See fig. 4.8e-f). Based on the removal of C and Cl after sputtering, it is concluded that both are surface-adsorbed impurities.

Considering the results presented above, it is concluded that solution-grown ZnO nanorods contain C and Cl as impurities within the first ~10 nm below the top surfaces of the samples. In the next section the stoichiometry of the nanorods is discussed.

ZnO stoichiometric ratios as function of annealing temperature and environment

A quantitative analysis of the Zn and O XPS peaks was done in order to study the ZnO stoichiometry before and after annealing. The following relationship as given in section 3.5 was used to calculate those ratios:

$$S_{\mathrm{Zn},O}{}^{X} = \frac{C_{Zn}}{C_O}$$

where C_{Zn} and C_O are, respectively, the concentrations of Zn and O. X stands for the environment of annealing or the type of sample (e.g. as-grown). The margin for error in the measured concentrations of Zn and O is about 2 % as mentioned in chapter 3. For quantification purposes the Zn $2p_{3/2}$ and O 1s XPS peaks were used.

Fig 4.9 presents the ZnO stoichiometric ratios ($S_{Zn,O}$) in sputtered ZnO nanorod samples annealed in N_2 and O_2. Only atomic concentrations measured after sputtering were calculated and considered in order to avoid dealing with impurity-related issues. Straight dotted lines were added to the figure to guide the eye. For annealing in nitrogen, it is clear that all stoichiometric ratios are above 1, regardless of the annealing temperature. Hence, these nanorods were rich in Zn. At 300 ^oC, the ZnO stoichiometry is unchanged, due to the fact that at this temperature there is no significant creation of intrinsic defects at concentrations that are detectable by XPS. Furthermore, the highest stoichiometric ratio $\left(S_{\mathrm{Zn},O}{}^{N_2}\right)$ deviation is observed for the sample annealed at 600 ^oC. For annealing in oxygen, the same trend in stoichiometric ratios $\left(S_{\text{Zn},O}{}^{O_2}\right)$ is observed, implying that the most abundant intrinsic defects in solution grown ZnO nanorods are oxygen vacancies (V_O).

The high concentration of Zn is not ascribed to Zn_i (Zn interstitials), since there is no source of zinc available during annealing to increase the concentration of zinc in the lattice. Also, Gorelkinskii *et al*. [45] concluded from the rapid quenching of electron-induced interstitial-related PL bands (even at RT) that interstitials will only exist at RT in the form of clusters and/or complexes. This suggests that in a N_2 environment, at temperatures around 600 °C, the creation of V_O related-defects is enhanced.

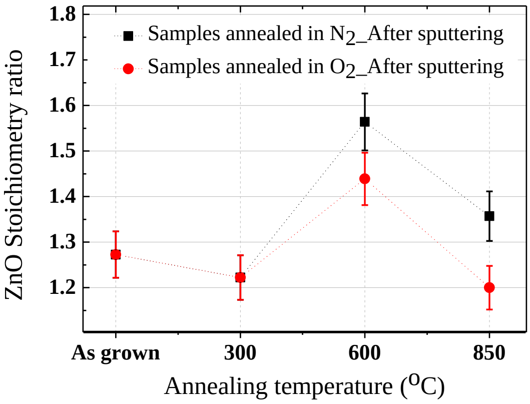

Figure 4.9. Stoichiometric ratios between Zn and O for samples annealed in N_2 and O_2 as function of annealing temperature.

Theoretical predictions by Kohan *et al*. [32] related to Zn-rich ZnO (see subsection 2.3.2) agree with the above observations. It was predicted that in a Zn-rich environment, V_O forms abundantly at 1000 K (726.85 °C), because of their lower formation energy. The reduced ratio (relative to a 600 °C anneal) in the case of the sample annealed at 850 °C is ascribed to the simultaneous loss of O and Zn atoms at this temperature, but at different rates. Furthermore, a clear effect of annealing environment and temperature on ZnO stoichiometry is also observable. As indicated in fig. 4.9 no difference is observed for the samples annealed at 300 °C ($S_{\text{Zn},O}{}^{N_2} \approx S_{\text{Zn},O}{}^{O_2}$), which suggests no significant creation of vacancies at this temperature. However, for higher annealing temperatures it appears that more oxygen vacancies are generated in a N_2 environment. N_2 is expected to be an inert gas and should not react with ZnO. As a result, annealing at higher temperatures in a N_2 environment should result in a relatively high concentration of V_O due to enhanced oxygen evaporation. Furthermore, a comparison of the stoichiometric ratios of Zn and O in samples annealed at

600 ^{o}C and 850 ^{o}C reveals an interesting result. The difference between $S_{\mathrm{Zn},O}{}^{N_2}$ and $S_{\mathrm{Zn},O}{}^{O_2}$ increases at 850 ^{o}C. The reduction of creation of V_O after annealing in O_2 environment is suggested to be as a result of the incorporation of oxygen from the annealing environment.

In summary, the surface of as-grown nanorods is Zn-rich. Annealing at and above 600 ^{o}C in both N_2 and O_2 resulted in the formation of V_O. However, annealing in O_2 at 850 ^{o}C again improved the stoichiometric ratio of Zn to O due to the inhibition of oxygen evaporation from the nanorods. The next section is dedicated to the analysis of high resolution of O 1s, Zn 2p1/2 and 2p3/2 XPS spectra.

High resolution XPS spectra

The binding energies in high resolution XPS spectra for different core level lines have been calibrated by taking that of C 1s as reference. Fig. 4.10 presents non-calibrated and calibrated XPS C 1s spectra collected from all the samples annealed in N_2 and O_2. Notice the poor signal to noise ratio of the spectra. Fig. 4.10a_1 and b_1 show, respectively, the binding energy spectra of C 1s in samples annealed in N_2 and O_2 as recorded clearly, the maxima of these lines do not occur at the same binding energy. Using the C-C binding energy of 284.8 eV [52] the calibrated C 1s spectra are shown in fig. 4.10a_2 and b_2. The same calibration process was subsequently applied to the O 1s and Zn $2p_{1/2}$ and $2p_{3/2}$ for all the XPS spectra recorded at high resolution. Taking into account the poor quality of the C 1s spectra used for binding energy calibration and the uncertainty related to the XPS apparatus, the estimated binding energy error is ± 0.35 eV.

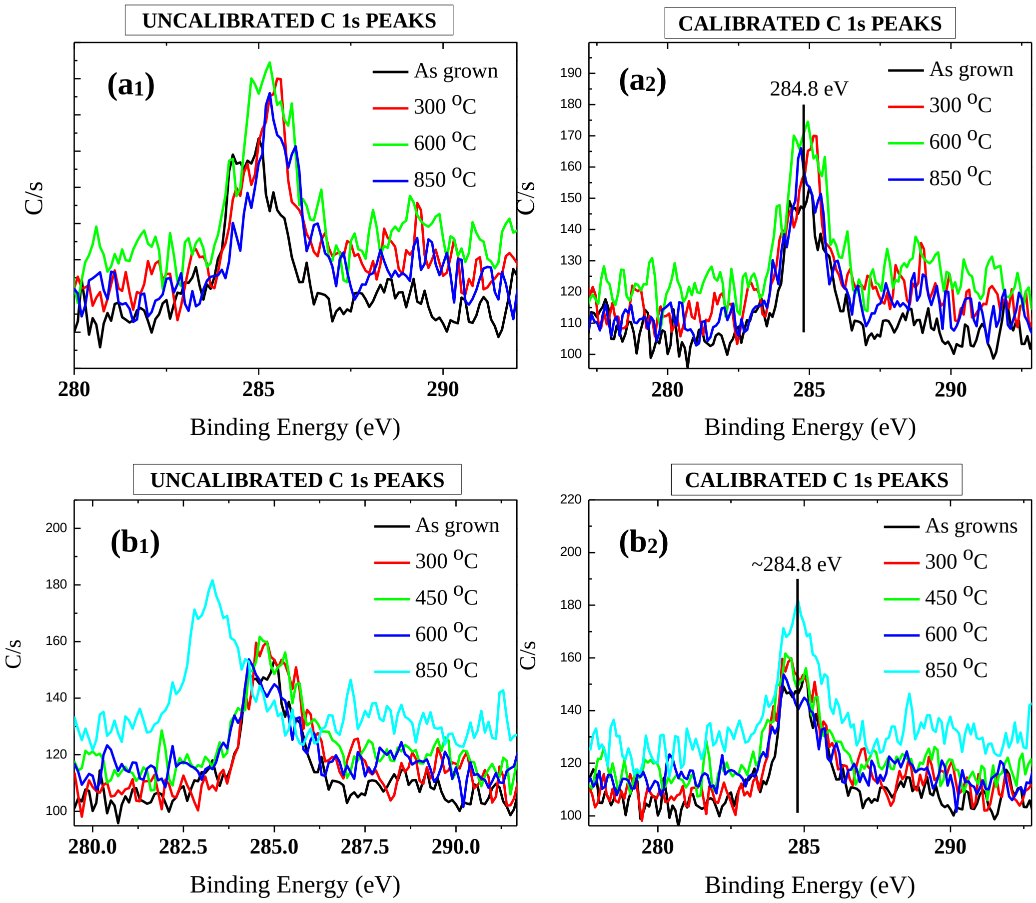

Figure 4.10. C 1s XPS spectra for as-grown nanorods and nanorods annealed in N$_2$ and O$_2$ at different temperatures: (a$_1$) N$_2$ before calibration, (a$_2$) N$_2$ after calibration, (b$_1$) O$_2$ before calibration, (b$_2$) O$_2$ after calibration.

O 1s, Zn 2p$_{1/2}$ and 2p$_{3/2}$ XPS spectra

Highly resolved O 1s and Zn 2p (Zn 2p$_{1/2}$ and 2p$_{3/2}$) XPS spectra from all samples annealed in N$_2$ and O$_2$ are summarised in fig. 4.11. The spectra collected after sputtering are shown in black in each figure.

Fig. 4.11a$_1$ and a$_2$ present the O 1s XPS peaks in the as-grown sample and samples annealed in N$_2$ and O$_2$, respectively. Irrespective of the annealing environment, two distinct peaks centered around 530.0 ± 0.35 eV and 531.5 ± 0.35 eV can be clearly seen. They are respectively called O1 (530.0 ± 0.35 eV) and O2 (531.5 ± 0.35 eV). Irrespective of the annealing temperature and environment the intensity of O2 is similar before and after sputtering. Yang *et al.* [14] also reported these two peaks at 530.35 ± 0.3 eV and 531.5 ± 0.35 eV from ZnO nanorods grown by CBD.

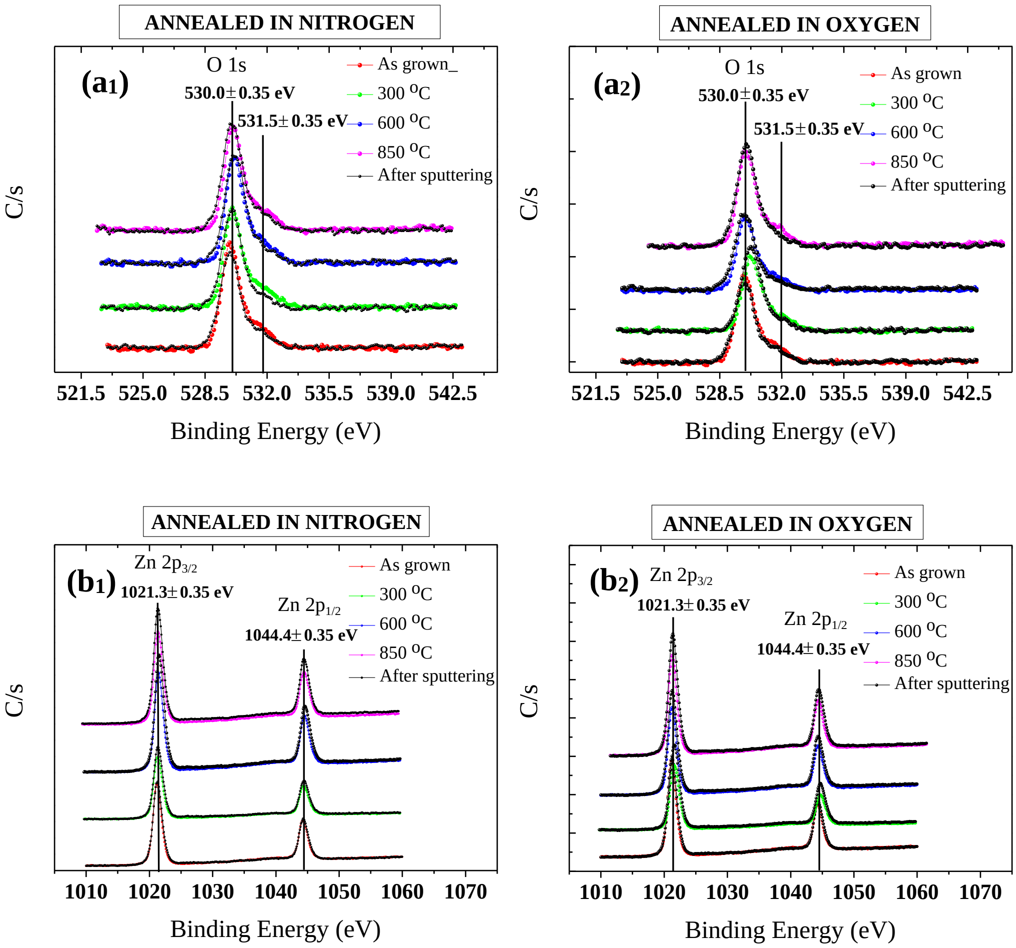

Figure 4.11. XPS spectra before and after sputtering for core level O 1s and Zn 2p (Zn $2p_{1/2}$ and $2p_{3/2}$) from as-grown nanorods and samples annealed at 300 °C, 600 °C and 850 °C in N_2 and O_2. (a_1) O 1s - N_2 annealed (a_2) O 1s - O2 annealed (b_1) Zn $2p_{1/2}$ and $2p_{3/2}$ - N2 annealed (b_2)) Zn $2p_{1/2}$ and $2p_{3/2}$ - O_2 Annealed.

The O1 line centered at 530.35 ± 0.3 eV is associated with O^{2-} ions in the wurtzite structure, surrounded by Zn atoms having their full complement of nearest-neighbour O^{2-} ions [14, 53]. O2 is generally attributed to O-atoms in a zinc deficient local environment and/or to O-atoms bound to H-species [53]. However, based on the acidity of the growth solution (pH~5.5) from which the nanorods were grown (see table VII in subsection 3.1), it is strongly suggested that the O2 peak originates from O atoms bound to H. This assignment will be confirmed later through ToF-SIMS investigations. Kunat *et al.* [54] also studied the surface characteristics of ZnO using XPS and convincingly showed that the line observed at 531.5 ± 0.35 eV is associated with OH. In the samples annealed at higher temperatures (≥ 300 °C), the presence of H near the top surface may have come mostly from exposure of nanorods to air [31]. Fig. 4.11b_1 and b_2 present the Zn 2p (Zn $2p_{1/2}$ and $2p_{3/2}$) binding energy spectra for the as-grown sample and samples annealed in N_2 and O_2, respectively. The annealing temperatures are shown in each figure. Only doublets at 1021.3 ± 0.35 eV (Zn $2p_{3/2}$) and 1044.4 ± 0.35 eV (Zn $2p_{1/2}$) are seen. The lack of any significant asymmetry in these signals may be an indication of a relatively lower concentration of Zn-related defects in the rods. In agreement with these results, V. Kumar *et al.* (53) observed this doublet at 1021.3 ± 0.3 eV (Zn $2p_{3/2}$) and 1044.4 ± 0.3 eV (Zn $2p_{1/2}$), respectively. It is associated with Zn^{2+} ions in the wurtzite structure, surrounded by O atoms with their full complement of nearest-neighbour Zn^{2+} ions [14, 53]. Any change in the intensity of this doublet is strongly connected to a variation in the concentration of Zn atoms in a fully oxidised stoichiometric surrounding.

A further investigation of the Zn $2p_{3/2}$ XPS spectra obtained from nanorods annealed in N_2 and O_2 is given in fig. 4.12a and 4.12b, respectively. It can be seen that the intensity of the peaks for annealed samples is enhanced by sputtering, especially for the two highest temperatures (600 °C and 850 °C). This simply means that the near-surface region is less stoichiometric, probably due to the out-diffusion of oxygen at higher temperatures.

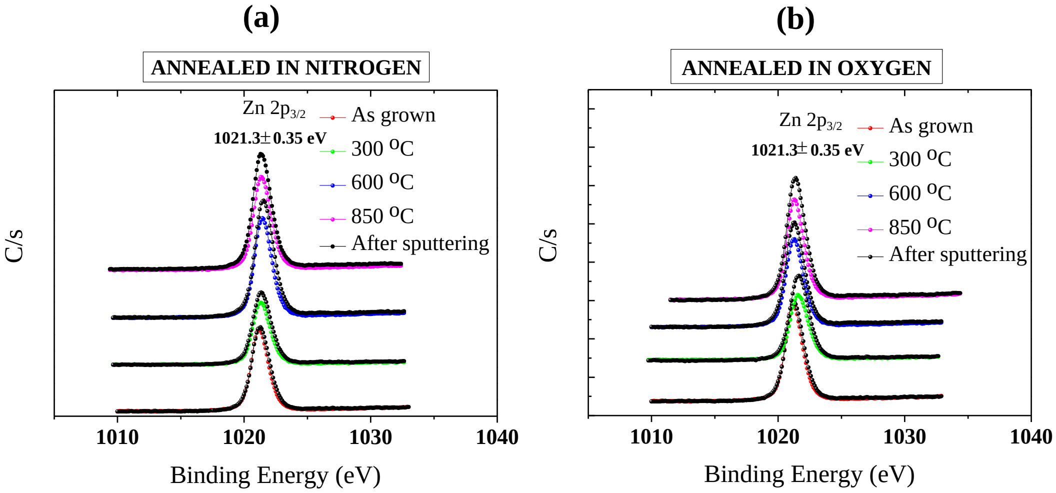

Figure 4.12. Zn $2p_{3/2}$ XPS spectra obtained from nanorods annealed in N_2 (a) in O_2 (b).

In summary, Zn and O atoms are, respectively, in their Zn^{2+} and O^{2-} oxidation states in ZnO. From the observations made above, it can be concluded that the surface of nanorods contain a significant amount of OH-related defects (indicated by the presence of the O2 peak in the O 1s XPS spectra). This is true even after annealing and is independent of the environment in which the samples were annealed.The stoichiometry along the lateral surfaces of nanorods is discussed below, as well as the effect of thermal treatment on the ZnO/Si interface.

4.2.3.2 Auger electron spectroscopy

The sketch given in fig. 4.13 shows the parts of nanorods that were characterised by Auger spectroscopy. The c-axis is perpendicular to the plane of the paper. Note the following: the AES excitation beam diameter was around 10 to 12 nm, and on all SEM micrographs presented in this section the positions from which the Auger signal was collected on the cross sections of the samples are indicated by straight blue lines.

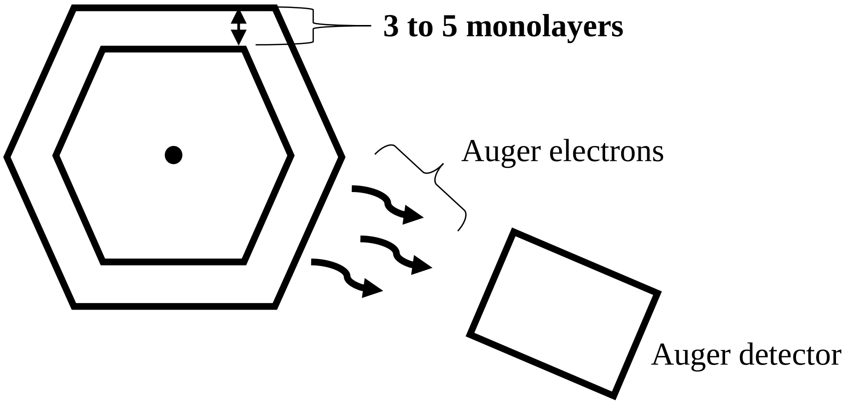

Figure 4.13. Sketch of the top view of a nanorod, showing approximately the parts of the nanorods from which the Auger electrons originated.

As grown nanorods

Fig. 4.14a_1 presents Auger derivative spectra for as-grown nanorods at two different positions, before sputtering. The two positions where the scans were taken are indicated as positions 1 (in the substrate) and 2 (middle of the rods) in the corresponding cross-sectional SEM micrograph shown in fig. 4.14a_2. The weak signal related to Zn and O in region 1 (substrate) might be caused by ZnO residue on the cleaved side of the substrate resulting from cleaving, since the diffusion of Zn or O into the substrate is not expected at this temperature. From fig. 4.14a_1, the Si-related signal is the most dominant in the Si region (region 1) before sputtering, whereas Zn and O related signals dominate in region 2. However, C is present in both regions. As in the case of XPS, the only measurable elements by AES are C, Zn, O and Si.

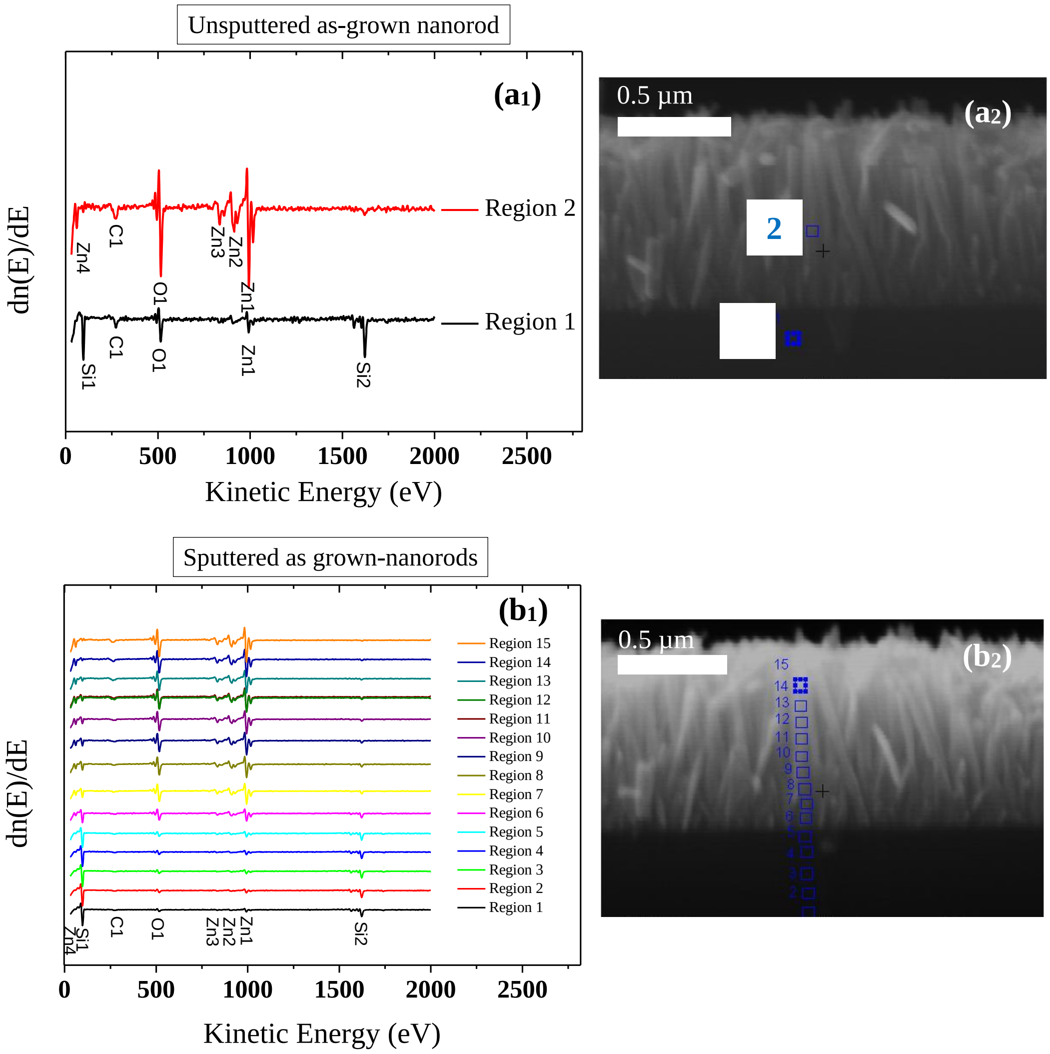

Figure 4.14. (a_1, b_1) AES survey scans on a cross-sectional surface of an as-grown sample before and after sputtering. (a_2, b_2) SEM micrographs of scanned regions.

The full cross-sectional scan results for this sample after sputtering for 1 min, is shown in Fig. 4.14b_1. Notice that sputtering removes approximately 22 nm. The scan positions are shown in the corresponding cross-sectional SEM micrograph in fig. 4.14b_2. Again the only measurable elements by AES are C, Zn, O and Si, even after sputtering. Starting from the substrate, in regions 1 to 5 (all from the substrate), the Si-related signals dominate the spectra. These decrease with distance from the substrate. For regions 6 to 14, taken from the nanorods, the most prominent signals are Zn- and O-related. C (surface-adsorbed) is the only impurity detected on the lateral faces of the as-grown nanorods. For comparison, the concentrations of all detected elements before and after sputtering are given in table VII. As expected, close to the substrate (positions 1 to 4) the dominant element is Si. Near the interface between the substrate and the rods (positions 5 to 7) the percentage of Si drops significantly and those of Zn and O start to increase. Far away from the substrate (positions 8 to 14) the signal is dominated by Zn and O. The percentage of C is found to be almost constant throughout the scan region. It is suggested therefore, that the lateral faces of the rods and the cleaved side of Si were contaminated by C during the sputtering process.

In a more continuous mode, AES results from a line scan (after 1 min argon sputtering of a 1 x 1 mm^2 region) along the side facet of an as-grown rod, from near its tip all the way into the substrate, is presented in fig. 4.15a$_1$. The corresponding SEM micrograph showing the scan line is presented in fig. 4.15a$_2$. Dashed lines have been inserted into fig. 4.15a$_1$ for discussion purposes.

Table VII. Atomic concentrations of elements detected before and after sputtering by AES (see fig. 4.14) from an as-grown sample in cross section, as expressed in %. The margin of error is 2%.

Scan region		1	2	3	4	5	6	7	8	9	10	11	12	13	14	15
Unsputtered nanorods	Si2				*59*					*8*						
	C1				***17***					***16***						
	O1				*16*					*41*						
	Zn1				*8*					*35*						
Sputtered nanorods	Si2	75	73	72	*69*	65	38	20	19	*16*	13	12	11	10	7	5
	C1	**9**	**9**	**8**	***9***	**10**	**9**	**8**	**9**	***10***	**9**	**11**	**13**	**14**	**16**	**12**
	O1	8	9	11	*12*	13	29	38	38	*41*	40	39	40	40	42	42
	Zn1	8	9	9	*10*	12	24	34	34	*36*	37	37	37	36	37	41

As can be seen from fig. 4.15a$_1$, C constitutes 80 % of the detected elements at the beginning of the scan. This indicates that all the C detected is from the chamber. It can be seen also that C is present all along the lateral surfaces. This is seems to be in disagreement with the observation made from XPS results related to C. After sputtering (i.e. the removal of ~9 nm from the top surface of the sample) the C-related XPS signal was not detected. In fact, AES is a technique often described as more sensitive than XPS. The difference in sensitivity is primarily due to the differences in electron kinetic energies [48-50]. It is evident that Zn and O are present on the substrate side, and that Si is detected from the film side. This strongly suggests cross-contamination of the surface due to the rather crude (macroscopic) sputtering process. It is worth noting that the Zn and O atomic concentrations reach their maximum values ~150 nm from the start of the scan. The difference between their normalised concentrations, however, starts to increase ~300 nm into the scan (see fig. 4.15a$_1$), meaning that the ZnO stoichiometric ratios may not be uniform along the lateral surfaces. This fact will be carefully investigated later as function of annealing temperature and environment.

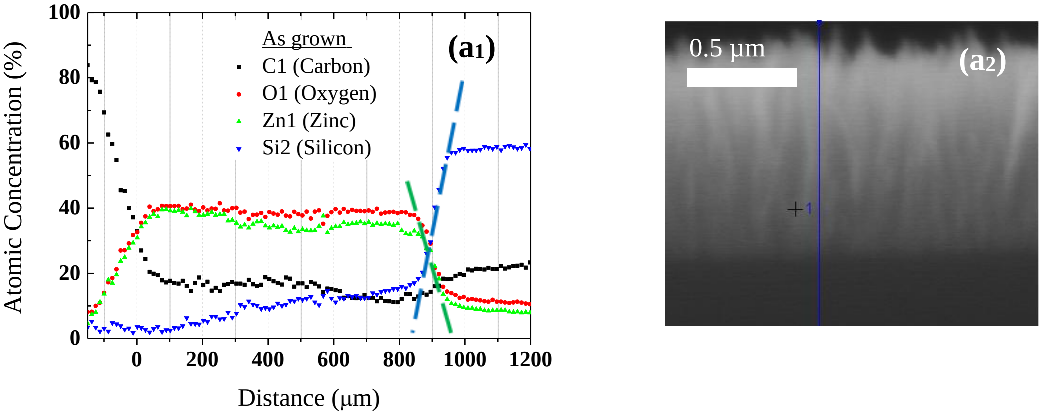

Figure 4.15. (a$_1$) Atomic concentrations of Si, C, Zn and O along the side facet of an as-grown nanorod, after removal of ~22 nm by sputtering. (a$_2$) SEM micrograph of the targeted nanorod.

Annealing in N_2 and O_2 at different temperatures

Results of AES investigations done on sputtered lateral surfaces of the nanorods annealed at 300 ^{o}C and 850 ^{o}C in N_2 and O_2 are presented in fig. 4.16 and 4.17, respectively. The atomic concentrations of Si, C, Zn and O from the sample annealed in N_2 at 300 ^{o}C are given in fig. 4.16a$_1$ while fig.4.16a$_2$ shows the corresponding SEM micrograph and the line along which the sample was scanned. For the sample annealed in N_2 at 850 ^{o}C, the atomic concentrations are given in fig. 4.16b$_1$and the corresponding SEM micrograph in fig.4.16b$_2$. The atomic concentrations of Si, C, Zn and O for the samples annealed at 300 ^{o}C and 850 ^{o}C are, respectively, presented in fig. 4.17a and c, while fig. 4.17b and d are the SEM micrographs indicating the positions of the scan lines. It is again evident that regardless of the annealing temperature and environment, C is present on the lateral surfaces, even in the Si region (as seen before in fig. 4.15). Fig. 4.17e presents the Si concentrations extracted from the Si2 AES signals (see fig. 4.16 and fig. 4.17). The concentrations were normalised to 1 to facilitate a direct comparison of the “rate of change” of the silicon concentration in the interfacial region. From this figure it can be deduced that no significant diffusion of silicon into the ZnO rods took place under the present annealing conditions – the slope of the data in the circled interfacial region remains unchanged, even upon high temperature annealing. Comparing the AES results with XPS, in terms of the Si signals detected, in particular the presence of Si detected by XPS on the top surface of some sputtered samples (see fig. 4.7d and f, and fig. 4.8f), it is concluded also that the Si-related photoelectrons (remember that the beam diameter is 100 µm) originated directly from regions of the sample where the ZnO rods do not cover the substrate completely. However, in the case of the AES results, the persistent presence of a Si signal is ascribed to surface adsorption that could have taken place during cleaving (for unsputtered surfaces) and during the sputtering process (for sputtered surfaces) as already mentioned.

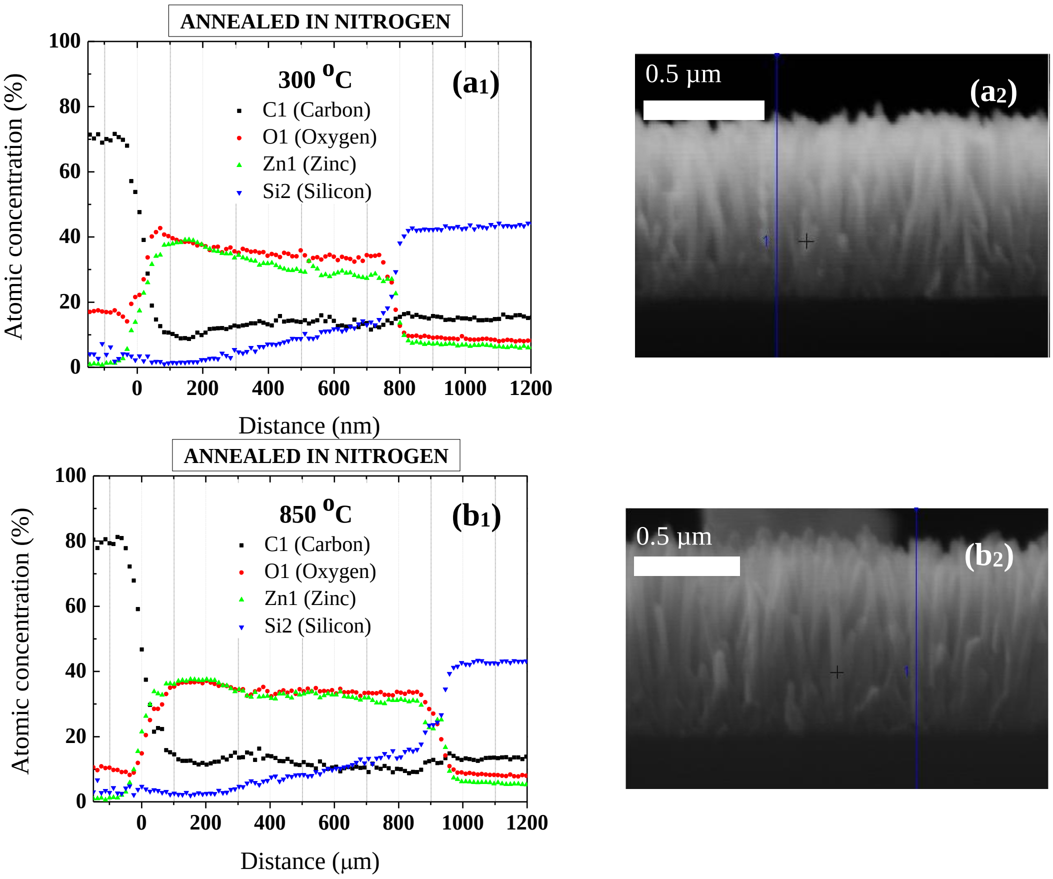

Figure 4.16. Atomic concentrations of Si, C, Zn and O from AES analysis of cross sections of samples annealed in N_2 at 300 °C (a_1) and 850 °C (b_1). The corresponding SEM micrographs showing the regions where the scans were performed are in a_2 and b_2, respectively.

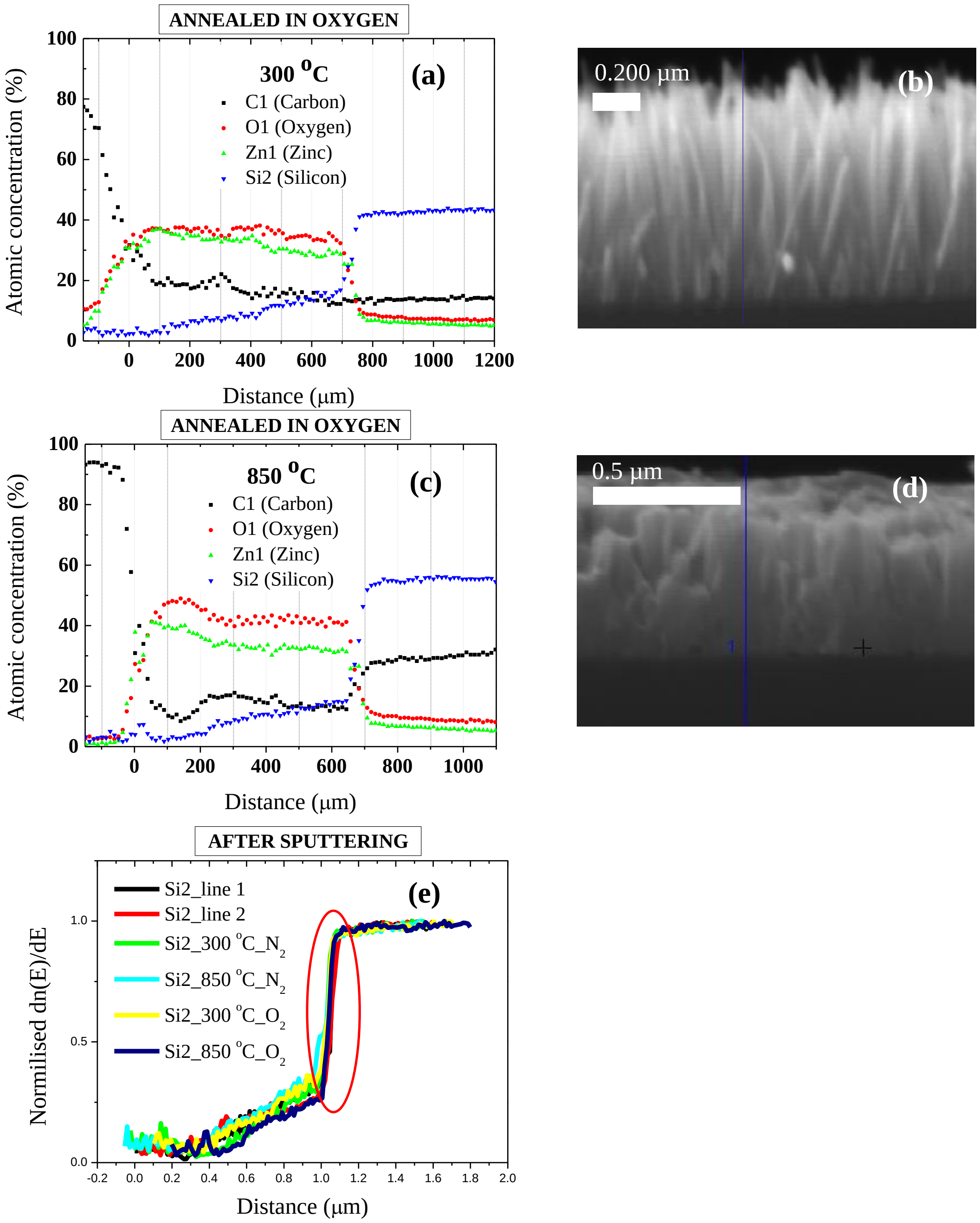

Figure 4.17. Atomic concentrations of Si, C, Zn and Zn along cross sections of the nanorods annealed O_2 at different temperatures: (a) 300 °C and (c) 850 °C. (b, d) Corresponding SEM micrographs. (e) Normalised Si-related AES concentrations.

The ZnO stoichiometric ratios were extracted from the data given in fig. 4.15 to 4.17 in order to study the effect of the environment of annealing at 850 °C on the stoichiometry of the rods. These ratios are summarised in fig. 4.18. Fig. 4.18a presents the stoichiometric ratios as function of the distance from the top surface of the nanorods annealed in N_2, while fig. 4.18b presents the ratios for the samples annealed in O_2. Fig. 4.18c compares the stoichiometric ratios of nanorods annealed in N_2 and O_2 at 850 °C to emphasize the effect of the ambient at this temperature. It can be seen that sputtered as-grown nanorods are nearly stoichiometric. But after annealing at 850 °C in N_2 and O_2, the lateral faces become richer in Zn, especially in the part of nanorods located ~100 nm below the top surface of the sample (i.e. $(000\bar{1})$ surface). Elsewhere, annealing at 850 °C caused the rods to become stoichiometric in the case of annealing in N_2 and O-rich in the case of annealing in O_2. This simply indicates that the effect of the annealing environment and temperature is more pronounced in the first ~100 nm below the top surface. It is suggested that most V_O-related defects are created during annealing at 850 °C (irrespective of the environment) in the first ~100 nm from the top surface, and that an O_2 environment reduces the rate of creation of these defects.

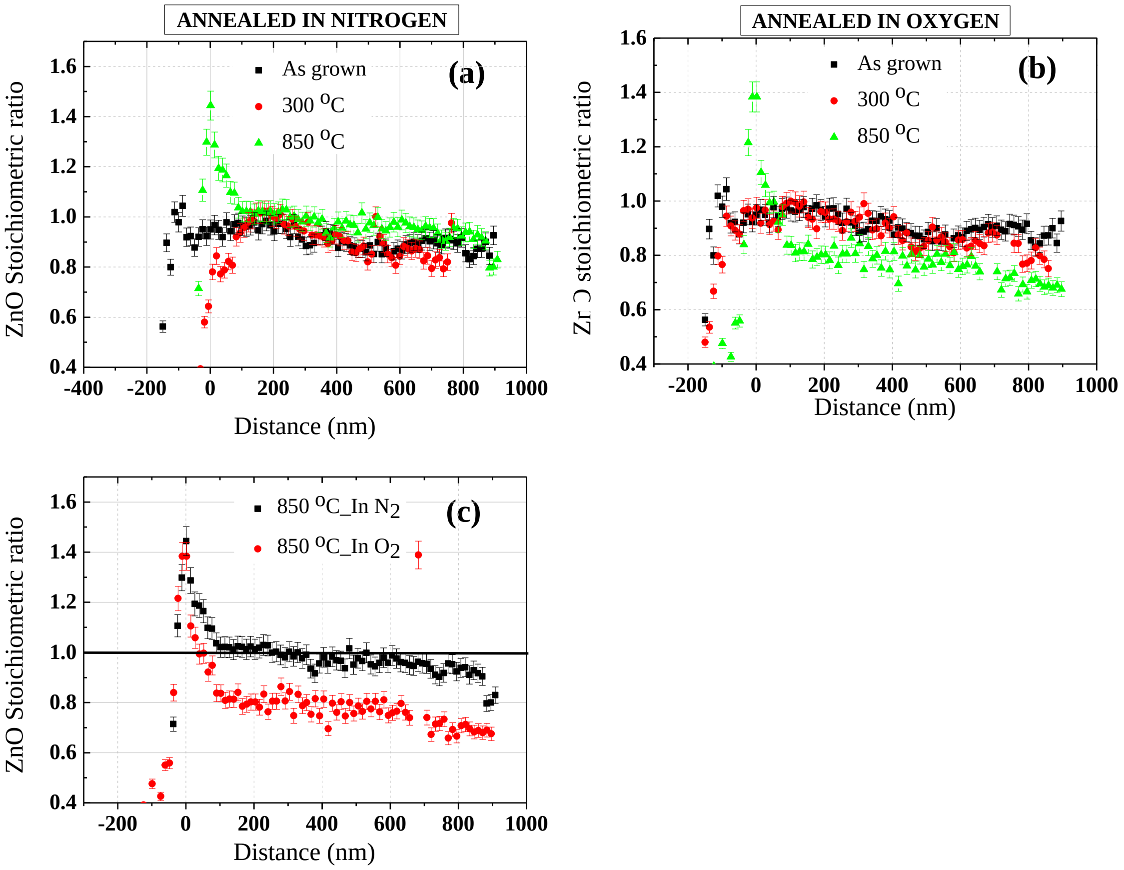

Figure 4.18. ZnO stoichiometric ratio in lateral faces as function of annealing temperatures and environments. (a) ZnO stoichiometric ratio of nanorods annealed in N_2; (b) ZnO stoichiometry ratio of nanorods annealed in O_2; and (c) ZnO stoichiometric ratio of nanorods annealed in N_2 and O_2 at 850 °C.

In conclusion, Si does not diffuse in ZnO at 85 °C during growth. Even at high temperature (~ 850 °C), no diffusion of Si could be concluded from these experiments. Furthermore, the effects of thermal treatment are more pronounced in the first ~100 nm from the top surface of the samples. In particular, V_O-related defects are created following annealing at 850 °C, irrespective of the ambient, in this region of nanorods. Finally, an O_2 flow during annealing reduces the creation of V_O-related defects in the rods, as seen by XPS. The complete chemical composition of nanorods from the top surface up to the substrate level is discussed in the next section.

4.2.3.3 Surface composition of ZnO nanorods by Time-of-Flight Secondary Ion Mass Spectrometry as function of annealing

In this section, ToF-SIMS studies on the as-grown nanorods and samples annealed in N_2 and O_2 at 850 °C are presented and discussed. During the scan, a 300 x 300 µm^2 area of each sample was randomly selected and sputtered. In order to avoid edge effects, information was collected only from 100 x 100 µm^2 within the sputtered region. Fig. 4.19 shows a typical top view video clip image of one of analysed samples. Fig. 4.19 a_1 shows a randomly selected area of a sample to be scanned, while fig. 4.19 a_2 shows the same area but after sputtering. It can be seen that sputtering took place over an area of 300 x 300 µm^2. Only the area marked by a red block in fig.4.19a_2 (100 x 100 µm^2) was scanned.

In order to obtain depth profiles and the distribution of ions in the material, scans were done gradually from the top surface of each sample. In fact, primary ions were shot at an interval of 15 sec, removing 2 to 3 monolayers from the rods. Then a scan was carried out as explained in subsection 3.6, followed by a pumping out of all analysed ions from the analyser. The same process was repeated many times until the substrate was reached. Fig. 4.20 illustrates this process, showing the sequential removal of layers of nanorods by sputtering.

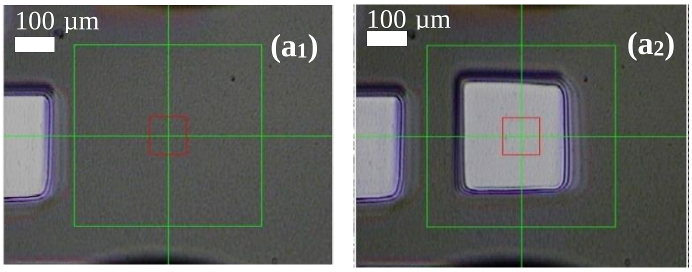

Figure 4.19. Two video clip images of analysed areas during ToF-SIMS measurements: (a_1) shows a selected area before sputtering, while (a_2) shows the same area as in (a_1), but sputtered. Secondary ions were analysed from the smaller region indicated by the red blocks.

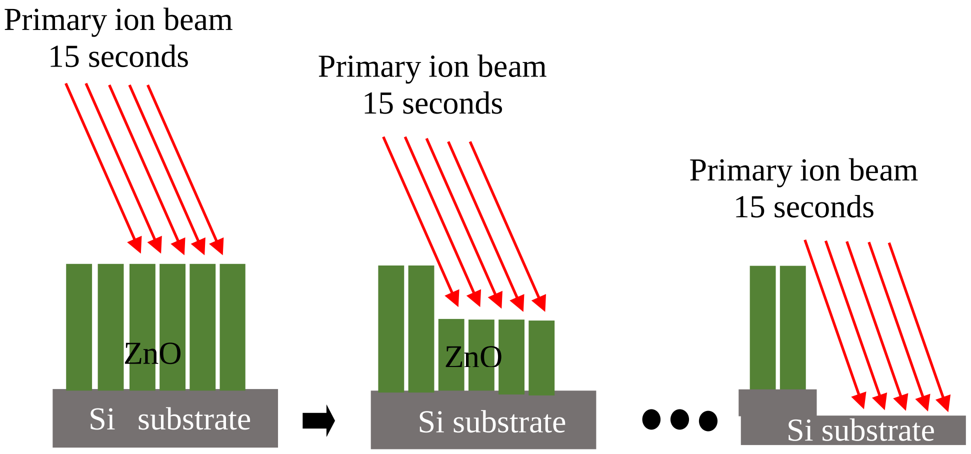

Figure 4.20. Schematic image showing how ZnO nanorods were analysed by ToF-SIMS as function of penetration depth.

4.2.3.4 Depth profile surveys

It is worth mentioning that in the following analysis attention was given to the identification of species in the nanorods, rather than their concentrations. Figs. 4.21 shows the chemical analysis versus depth from the as-grown nanorods with different primary ion sources: (a) positive ions (oxygen primary beam) and (b) negative ions (cesium primary beam). It should be pointed out that depth profiles were recorded as function of sputter time, which is defined as the number of the scan *multiplied* by the sputter interval. For example, in fig. 4.21a the total number of scans is 120, while in (b) it is 90. In all cases the sputtering interval was 15 sec. Hence the total sputter time is 1800 s in (a) and 1350 s in (b).

From fig. 4.21a, it can be seen that H^+, CH_3^+, ZnO^+, ZnH^+ and $ZnOH^+$ species were detected in the secondary beam. It is important to emphasise that the growth precursors are made from zinc nitrate hexahydrate ($Zn(NO_3)_2{\bullet}6H_2O$)) and hexamine ($C_6H_{12}N_4$). The mixed solution has a pH of ~5.5 at 85 °C. Hence the hydrogen-containing species (H^+, ZnH^+ and $ZnOH^+$) are suggested to result from hydrogen incorporation during growth. Carbon could result from adsorbed species from the ambient, but could also incorporate from the hexamine during growth.

From fig. 4.21b it can be seen that negative secondary ions like C^-, OH^-, F^-, S^-, and Cl^- are also detected from the as-grown sample. The origin of C is the same as that of the hydrocarbons seen in fig. 4.21a. In addition, contamination by Cl and S also is suggested to be from the precursors, as zinc nitrate hexahydrate ($Zn (NO_3)_2{\bullet}6H_2O$)) contained 50 mg/kg of Cl and 100 mg/kg of sulfate. However, the origin of F is still unknown. In summary, it is clearly shown that H, F, S, and Cl are the main contaminants in the as-grown sample.

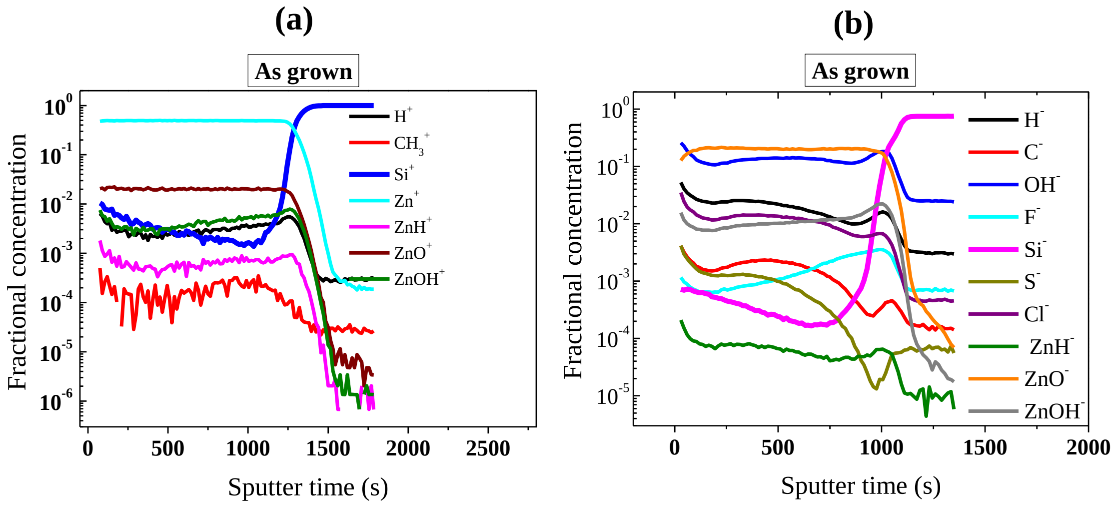

Figure 4.21. SIMS depth profile survey from the as-grown nanorods with different primary ion sources: (a) positive ion spectroscopy using cesium as a primary beam and (b) negative ion spectroscopy using oxygen as primary beam.

The effect of annealing ambient (i.e. O_2 or N_2) on the chemical composition of the nanostructures was also studied. Fig. 4.22a and b presents the ToF-SIMS depth profiles from samples annealed at 850 °C in N_2 and O_2, respectively. The results from positive ion spectroscopy are shown in a_1 and b_1, while those from negative ion spectroscopy are shown in a_2 and b_2. As can be seen from these figures, the same elements were observed as in the as-grown nanorods. Table VIII summarizes the chemical species detected from the ToF-SIMS studies.

An increase of H^-, OH^-, $ZnH^{-/+}$, and $ZnOH^{-/+}$ species is observable in the first ~120 sec, as seen for example in fig. 4.21b and fig. 4.22a_2 and b_2, confirming that hydrogen was adsorbed in the “near surface region” of the nanorods. In order to illustrate the effect of annealing on the distributions of these impurities, depth profiles of H^- and OH^- in the as-grown and 850 °C-annealed samples are compared in fig. 4.23a and b, respectively. From these spectra the following observations can be made: (i) the H^- and OH^- signals increase in the “near surface region” of the as-grown samples; (ii) these signals decrease in the bulk after annealing, but are still observed; (iii) the accumulation of hydrogen near the substrate interface reduces after annealing in nitrogen only.

Table VIII. Summary of chemical found in ZnO nanorods grown by CBD in the as grown sample and sample annealed in N_2 and O_2 at 850 °C.

Species name	Chemical symbol of detected species
Oxygen, hydroxyl group, and hydrogen	OH^-, $H^{-/+}$
Carbon	C^-
Hydrocarbons	CH_3^+ and $C_2H_3^+$
Fluorine, Suflur, and Chlorine	F^-, S^-, Cl^-
Zinc oxide	$ZnO^{-/+}$
Zinc hydride	$ZnH^{-/+}$
Zn hydroxide	$ZnOH^{-/+}$

The accumulation of hydrogen near the surface of as-grown nanorods has been observed by many research groups. For example, Yang *et al* [14], using XPS, deduced the presence of H in the "near surface region" from the O-H-related O1s peak at 531.5 eV. An excitonic recombination line (I_4) attributed to H in oxygen vacancies (H_O) was observed in the PL of as-grown nanorods grown in our laboratory (see [18]), which disappeared after annealing at 450 °C, irrespective of the annealing environment. As stated above (see (ii)) a significant decrease in the SIMS signal from hydrogen-containing ions in the "the near surface region" and in the bulk of the samples after annealing indeed confirms the out-diffusion of hydrogen species. The observed hydrogen "accumulation" in the "near surface region", in the annealed nanorods is ascribed to adsorption from the ambient (i.e. hydrogen containing species adsorbing to the polar surfaces in the time between annealing and SIMS analysis). As a result of sputtering (to produce the depth profiles) the surface morphology of the samples will change, resulting in an effectively smaller polar surface area as the sample surface evens out/flattens.

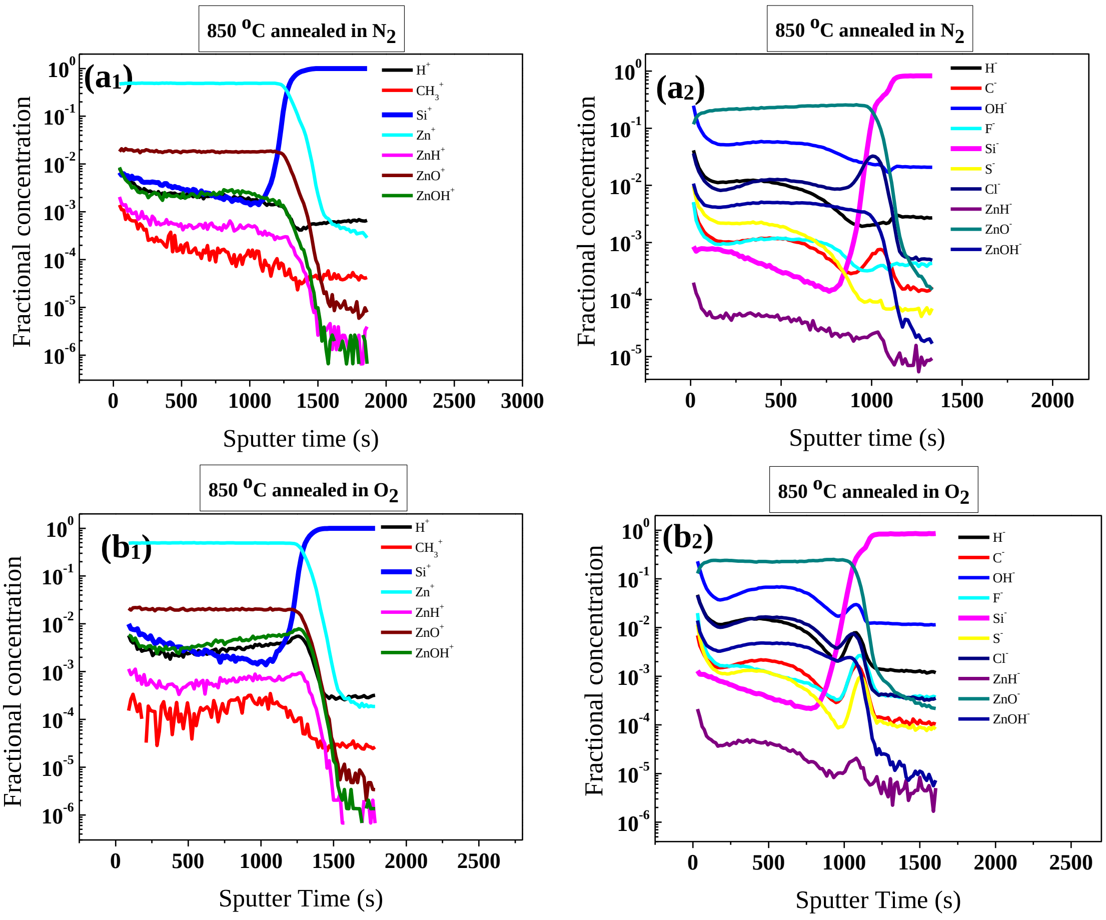

Figure 4.22. ToF-SIMS depth profiles of secondary positive ions (a_1) and negative ions (a_2) from a sample annealed in N_2 at 850 °C. ToF-SIMS depth profiles of positive ions (b_1) and negative ions (b_2) from a sample annealed in O_2 at 850 °C.

Based on comparisons of time decays of excitons in as-grown and 500 °C-annealed nanorods, Yang *et al.* [14] suggested the existence of remnant H bound to O (O2 peak in XPS) near the surface, even after 1 h of annealing. Thus, the observed accumulation of hydrogen-related species near the top surface of the rods might in part result from hydrogen diffusion from the bulk region of the sample. The detection of H-containing ions throughout the entire thickness of the samples, even after annealing at 850 °C, seemingly contradicts PL data that confirmed a complete out-diffusion of H_O and H_{BC} from bulk ZnO [55] and nanorods [18] after annealing at high temperatures. PL probes the "near surface" of the sample, rather than the "bulk region", and may therefore not be sensitive to hydrogen in the bulk. Furthermore, hydrogen atoms may combine to form molecules upon annealing, which will contribute to the SIMS signals but not to the excitonic PL spectrum for ZnO.

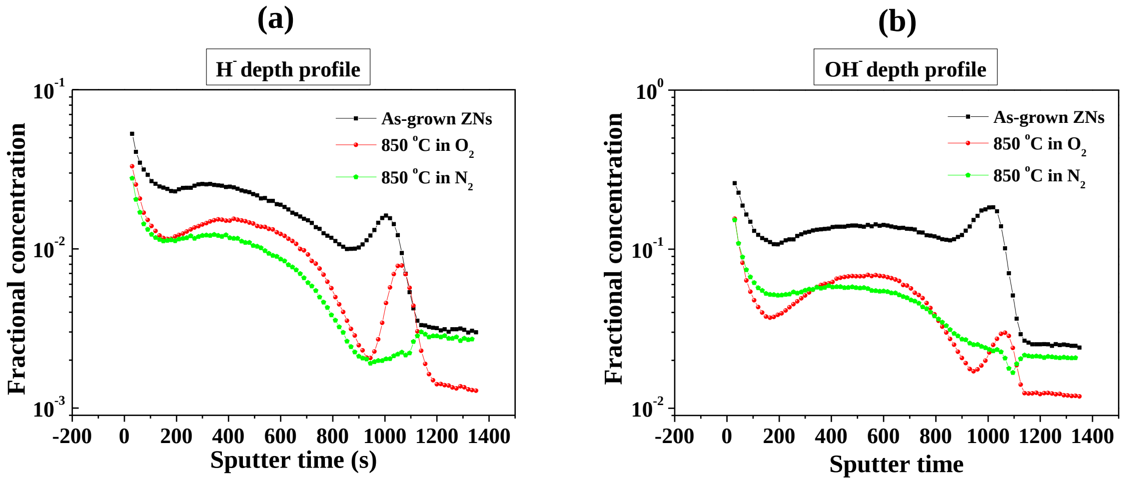

Figure 4.23. TOF-SIMS depth profiles of (a) H^- and (b) OH^- species in as-grown ZNs and annealed at 850 ^{o}C respectively in O_2 and in N_2.

4.2.4 Effect of annealing temperature, environment and time on optical properties using Photoluminescence Spectroscopy

In this section, the effect of annealing environment and time on the optical properties of the nanorods at “room temperature” is investigated. A preliminary study of the effect of annealing temperature was conducted using a mini-PL UV Laser System 5.0. For full specifications concerning this photoluminescence set-up, refer to section 3.4. It is important to note that this PL system is more sensitive to UV emission than to visible and near infrared emission. In a typical experiment a sample was cleaved into smaller pieces and annealed in oxygen ambient for 30 min at temperatures ranging from 200 °C to 900 °C in increments of 25 °C. Fig. 4.24a-b display the effect of annealing temperature on the UV emission and deep level emission (DLE) intensity as a function of annealing temperature, respectively. As can be seen from this figure, for annealing temperatures below 300 ^{o}C a strong increase in the intensity of the UV emission and a concomitant decrease in the DLE intensity can be seen. Between 300 ^{o}C and ~500 ^{o}C the intensity of the UV emission decreases rapidly, whereas the DLE intensity increases significantly. Between 500 ^{o}C and 700 ^{o}C no significant change is observed in the intensity of the UV emission; however, the DLE intensity now decreases. Above ~700 ^{o}C, both the intensity of the UV emission and DLE increase significantly.

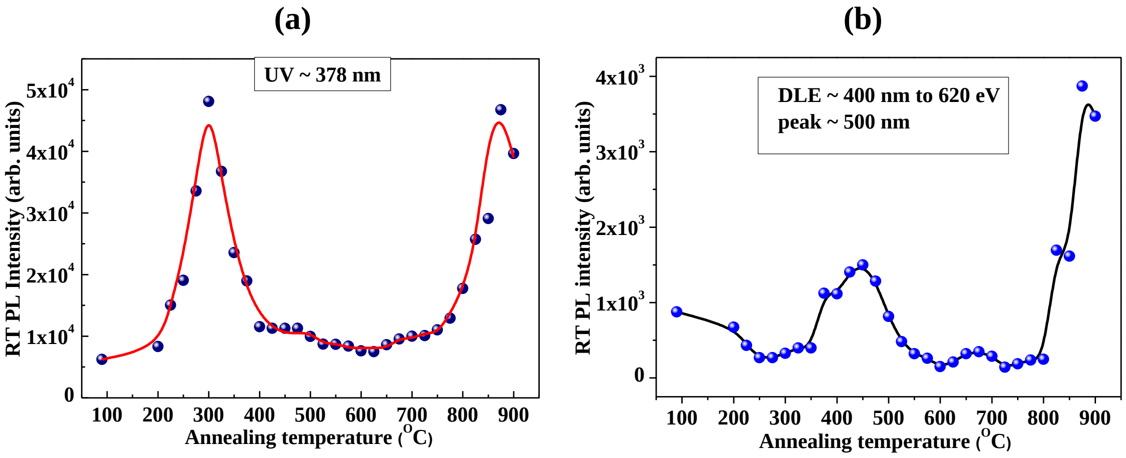

Figure 4.24. Effect of annealing temperature on the UV and deep level emission (DLE) intensity as a function of annealing temperature: (a) UV (b) DLE. The lines connecting data points are guides to the eye.

As this mini PL system is not sensitive enough to the DLE from ZnO, which is the main objective of this study, the Big PL system was used for the remaining investigations discussed below. For full specifications concerning this set-up, refer to section 3.4. The results that follow were obtained with a 1800.48 gr/mm grating, blazed at 400 nm. A PMT with GaAs photocathode was used for all the measurements. The spectral response of the PMT covers the UV, the visible and the near infrared region up to ~ 850 nm.

4.2.4.1 Effect of annealing temperature

For this study, segments were cleaved from an as-grown sample, one of which was subsequently used as a reference. Before annealing, a PL spectrum was taken from different pieces in order to confirm the uniformity across each sample. Starting at 300 °C, a single piece of a sample was annealed for 30 min in O$_2$ ambient. This was followed by a PL measurement, a further 30 min anneal at an increased temperature of 400 °C, and a subsequent PL measurement. This process was repeated, with the annealing temperature ramped up in increments of 100 °C before subsequent PL measurements. The highest annealing temperature was 900 °C. This process will subsequently be referred to as sequential annealing. The same procedure was repeated for a N$_2$ ambient. Irrespective of annealing ambient, it was found that 30 min is long enough to enhance/supress the UV/deep level emission (for more details see [56]). As a result, the duration of each annealing step was fixed to 30 min.

a. As-grown nanorods

Fig. 4.25 shows typical normalized RT PL spectra of as-grown nanorods from different cleaved pieces of a sample. As can be seen, the spectra are very similar, indicating the uniformity of the rods. In all cases the PL spectra of the nanorods exhibit a UV emission at around 379.5 nm and a broad DLE. The UV emission is attributed to band-edge emission associated with free excitons (FX). The broad visible bands are generally attributed to intrinsic defects in ZnO (see section 2.3.3), which are often called DLE. The peak observed at ~759 nm is the second order of the NBE. The apparent PL band (encircled) at around 850 nm is induced by the detection limit (cut off) of the detector. In addition, the small sharp peak at around 440 nm is from the laser plasma and will therefore not be discussed.

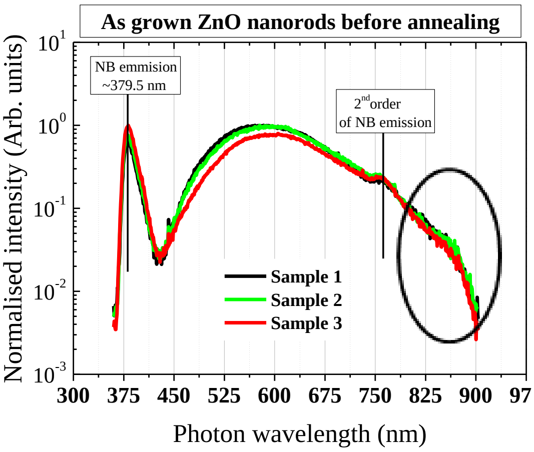

Figure 4.25. Typical room temperature PL spectra of as-grown ZnO nanorods from three different pieces of a sample.

b. Optical properties of nanorods annealed in controlled flows of N_2 and O_2

Fig. 4.26 shows RT PL spectra of samples sequentially annealed at different temperatures in (a) N_2 and (b) O_2. As can be seen from these spectra the intensity of both the UV emission and DLE significantly varies with annealing temperature. In particular, the highest UV emission intensity, irrespective of annealing ambient, is observed from nanorods annealed at 300 °C. When compared with the as-grown nanorods, the intensity of the DLE is slightly decreased after annealing at this temperature. For higher annealing temperatures (greater that 300 °C) the intensity of the UV emission is lower than that of the 300 °C annealed sample. In addition the position of the dominant DLE band changes with annealing temperature. Based on the change in the peak position of the DLE and decrease in the intensity of the UV emission following annealing, the effect of annealing temperature can be classified into two ranges: 300 °C to 600 °C and from 600 °C to 900 °C. This can be seen more clearly in fig. 4.27, where spectra for the lower temperature range are shown in a_1 (N_2) and b_1 (O_2) and those collected after annealing in the higher temperature range are shown in a_2 (N_2) and b_2 (O_2). The dotted lines are Gaussians indicating the positions and widths of the three bands believed to contribute to the DLE following annealing at 900 °C.

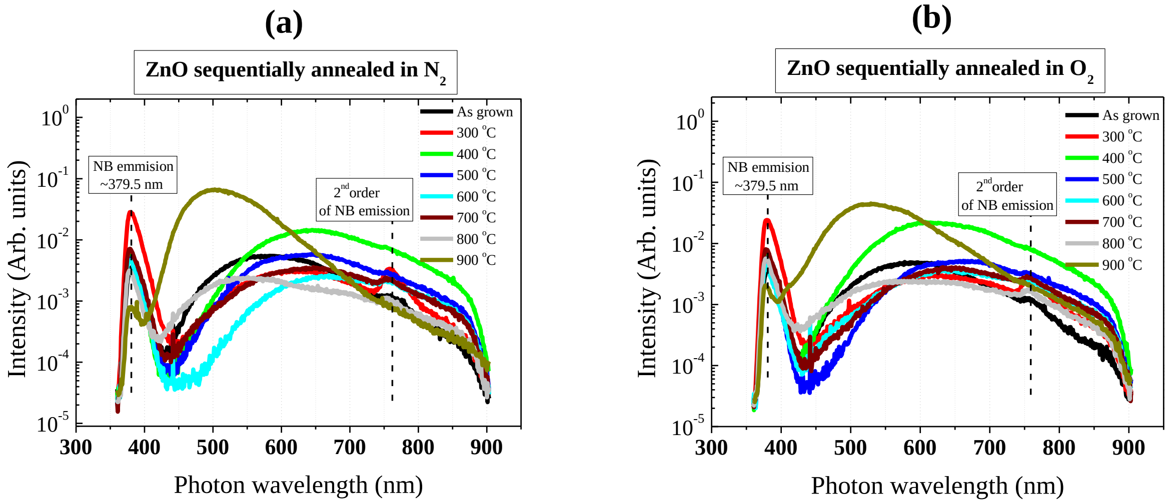

Figure 4.26. ZnO nanorods annealed sequentially for 30 minutes in controlled flows of (a) N_2 and (b) O_2.

From studying the PL as function of annealing temperature, the following remarks can be made: (i) there is an increase in the UV intensity and a concomitant decrease in the DLE intensity after annealing at 300 °C, irrespective of the annealing environment (see fig. 4.27a_1 and b_1); (ii) an overall increase in the DLE intensity is observed after annealing at 400 °C and a simultaneous decrease in the UV intensity occurs (see fig. 4.27a_1 and b_1); (iii) a quenching of the DLE is seen above 400 °C (up to 600 °C), irrespective of the ambient, while the UV emission intensity weakly fluctuates (see fig. 4.27a_1 and b_1); (iv) based on the spectral changes of the DLE with annealing temperature, the DLE is deduced to be composed of at least two wavelength regions: blue-green (with the highest energy band at ~500 nm) and yellow-red (with the highest energy band at ~650 nm); and (v) a significant increase in the intensity of the DLE in the blue-green region is evident after annealing at temperatures above 800 °C (see fig. 4.27a_2 and b_2). The influence of annealing ambient is minimal.

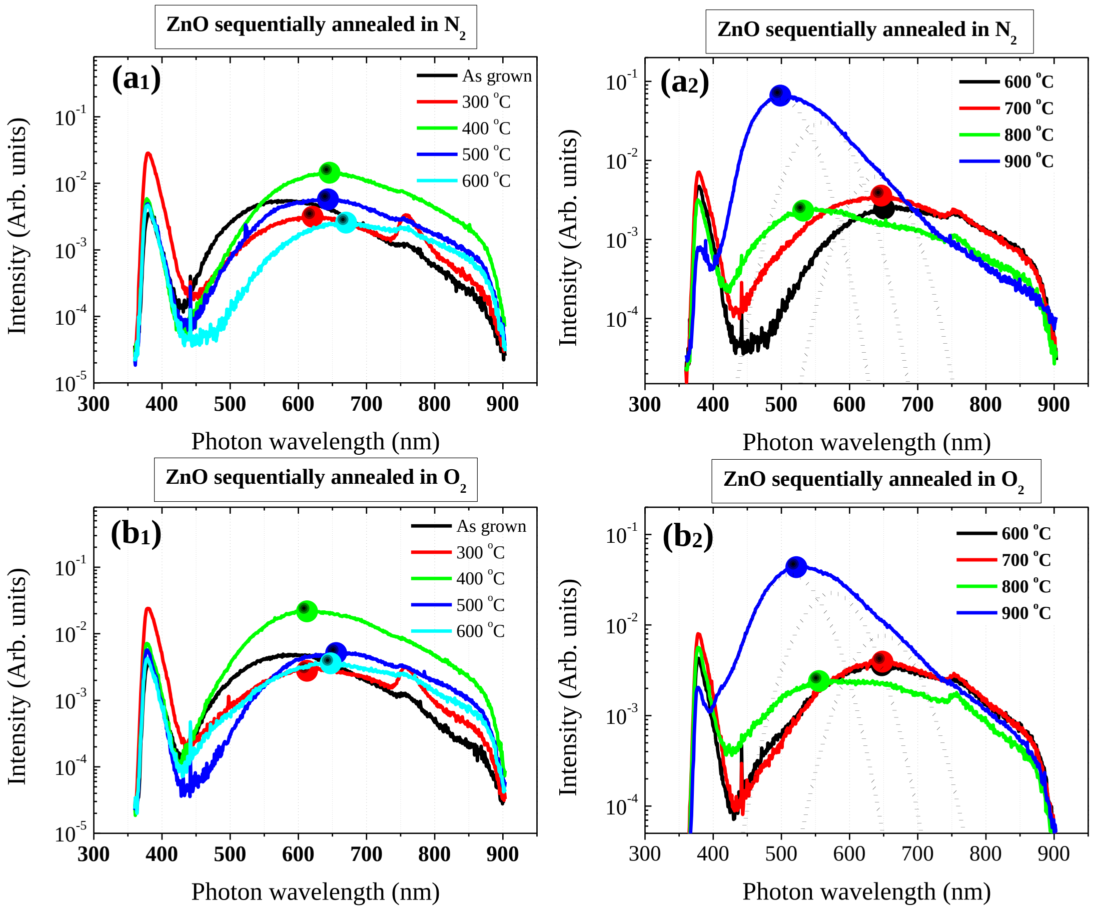

Figure 4.27. (a_1, b_1) RT PL spectra of samples sequentially annealed between 300 °C and 600 °C in: (a_1) N_2 and (b_1) O_2 flow. (a_2, b_2) RT PL spectra of samples annealed between 600 °C and 900 °C in (a_2) N_2, and (b_2) O_2 flow. The maximum intensity of the DLE was taken at the spherical dots shown in the figures. Dotted lines in a_2 and b_2 are Gaussians indicating the positions and widths of the three emission bands deduced to contribute to the visible PL after a 900 °C anneal.

As indicated in remark (i) and pointed out previously (see fig. 4.24), the highest UV emission intensity, irrespective of annealing ambient, is observed from the nanorods annealed at 300 °C. It is important to notice that while annealing significantly enhances the UV emission, the DLE intensity is barely changing at this temperature. To illustrate this effect, the UV to DLE intensity ratios and positions of the maximum intensity of the DLE are shown in fig. 4.28a and b, respectively, as a function of annealing temperature. The intensity of the DLE was taken at the wavelengths indicated by the circular dots in fig. 4.27. As can be seen from fig. 4.28a, the highest and lowest UV to DLE intensity ratios are observed for nanorods annealed at 300 °C and between 400 °C and 500 °C, respectively. The observed increase in the ratio for nanorods annealed at 300 °C is due to the significant increase in the UV emission and a slight decrease in the intensity of the DLE. In contrast, the decrease in the ratio for the rods annealed between 400 °C and 500 °C is caused by a combination of a decrease in the UV emission and a significant increase in the DLE. For clarity, the RT PL spectra from nanorods annealed at 300 °C and 400 °C, together with those of as-grown nanorods, are re-plotted in fig. 4.29. The decrease (300 °C) and increase (400 °C) in the intensity of the dominant DLE are highlighted by the arrows.

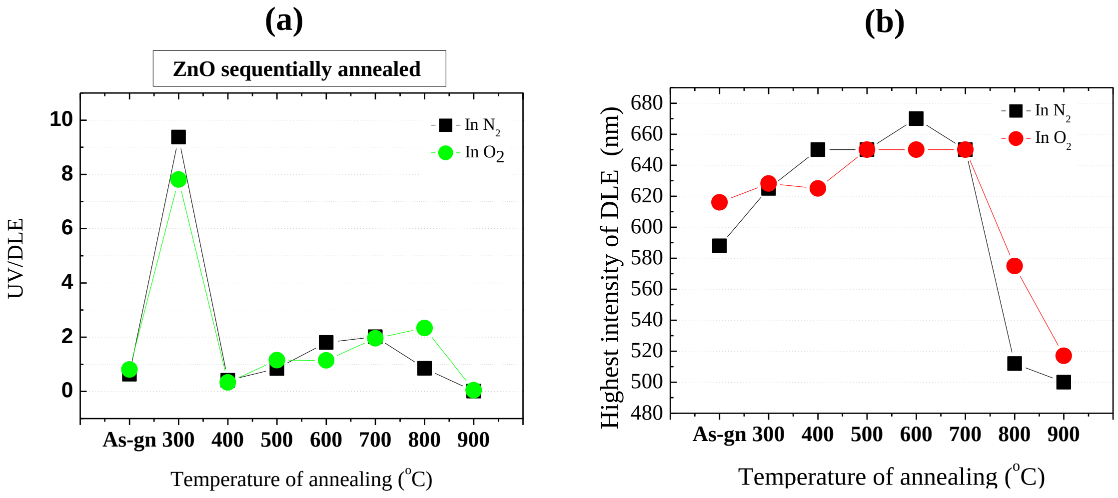

Figure 4.28. (a) Ratios of intensities between the UV emission and the dominant DLE as a function of annealing temperature. (b) Positions of DLE maximum as function of annealing temperature. Both sets of data were extracted from fig. 4.26.

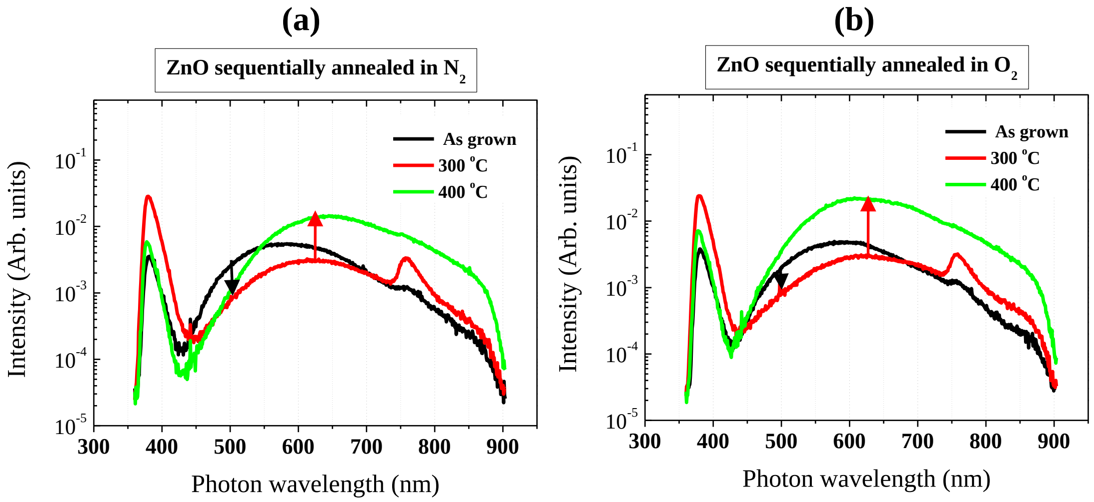

Figure 4.29. Comparison of RT PL spectra of ZnO nanorods sequentially annealed in different environments between 300 °C and 400 °C: (a) in N_2 and (b) in O_2.

The increase in the UV emission intensity and suppression of the defect-related emission following annealing has been observed in solution grown ZnO nanostructures and is typically attributed to the removal of surface-adsorbed impurities [56-58]. As shown from the XPS and ToF-SIMS results in previous sections, hydrogen is the most abundant surface-adsorbed impurity. It has been suggested to introduce band bending near the surface and therefore influence the PL properties of ZnO [59-60]. Hence it is natural to associate the increase in the UV intensity after annealing at 300 °C with their removal or out-diffusion (see remark (i)).

Another reason for the increase in UV emission is the defect passivation effect of hydrogen [61-63]. For example, Dev *et al.* [61] observed an enhancement of the near-band-edge emission and a concomitant quenching of the deep level emission at room temperature in ZnO nanowires following hydrogen plasma treatment. The authors related the observed enhancement of the near-band-edge emission and decrease in DLE to a large amount of hydrogen incorporated on interstitial sites, providing additional radiative channels for bound-exciton recombination and the passivation of deep centres, respectively [61]. Furthermore, in hydrogen plasma-treated ZnO, the formation of H_{Zn} and H_O [62-63] and the possibility of trapping of H_i in vacancies [55] has been already reported. It has also been reported that hydrogen can form complexes with zinc vacancies ($V_{Zn}H_2$) and with oxygen vacancies (V_OH_2) during hydrogenation [64-65]. As indicated by the XPS and ToF-SIMS results, hydrogen is part of the nanorods in this study. In addition, we have clearly illustrated the presence of hydrogen in oxygen vacancies (H_O), which gives rise to a low temperature PL line (often labelled as I_4) that is significantly reduced after annealing at 450 °C (18). The same observation was reported by Herklotz *et al.* (55). Furthermore, a closer look at the RT PL spectra of the nanorods annealed at 300 °C (fig. 4.29), reveals that the decrease in the DLE intensity after annealing at 300 °C (remark (i)) happens in a specific region of the spectrum (see the arrows in fig. 4.29). It is therefore concluded that annealing at 300 °C does not increase the concentration of new deep centers, but rather causes passivation, which quenches the DLE as noticed. This conclusion is in agreement with the XPS results which indicated no change in stoichiometry upon annealing at low temperatures (section 2.2.3.1). Given the relatively low annealing temperature (300 °C), and based on the abundance of H related-defects in as-grown nanorods, the enhancement of the UV intensity and the slight quenching of the DLE irrespective of the annealing ambient is also ascribed to the effect of the passivation of hydrogen.

As the annealing temperature increases further from 300 to 400 °C, previously H passivated defects (H_O and/or H_{Zn}) will be activated, resulting in an enhancement of the DLE and a decrease in the UV emission intensity (remark (ii)). As indicated above, the out-diffusion of H has been also confirmed by the disappearance of the low temperature PL line (I_4) after annealing at ~450 ^{o}C (18). Additionally, the removal of hydrogen-related defects in hydrogenated ZnO after annealing at 450 ^{o}C was also deduced from RT PL in Ref [64].

Another contributing factor to the increase in DLE after annealing at 400 ^{o}C is the dissociation of existing complexes, such as V_OZn_i [66] into V_O and Zn_i. Theoretical investigations have shown that under Zn rich conditions Zn_i and V_O can interact and form stable V_OZn_i complexes (at RT) that contribute to the n-type conductivity of undoped ZnO [66]. Kim *et al*. [66] investigated the interaction of a zinc interstitial (Zn_i) with an oxygen vacancy (V_O) in order to understand the origin of native n-type ZnO by using density functional theory with the hybrid functional. The authors found that the V_OZn_i complex has a lower formation energy than of the sum of the individual point defect formation energies, and that it creates a shallow donor with +1 charge state[66]. Given the fact that as-grown nanorods are Zn-rich (see fig. 4.9 on page 46), the existence of these complexes in as-grown material is quite likely. Hence, the overall increase in the DLE intensity upon increasing the annealing temperature from 300 ^{o}C to 400 ^{o}C, is suggested to result from a combination of the out-diffusion of hydrogen in vacancies (V_{Zn} or/and V_O) and the dissociation of complexes such as V_OZn_i.

The quenching of the DLE following annealing at a temperatures between 400 ^{o}C and 600 ^{o}C (remark (iii)) can be associated with the activation of "hidden" interstitial H_2 [65] or H_2 molecules kinetically trapped in the oxygen vacancy [67], that convert into atomic hydrogen during annealing. By combining local mode and free carrier infrared (IR) absorption measurements, Shi *et al.* [67] studied the effect of annealing on as-received hydrothermally grown ZnO substrate. They reported an IR line at 3326.3 cm^{-1} (at 4 K) which was activated only after annealing near 400 ^{o}C. The intensity of this line increased with annealing temperature between 400 ^{o}C and 500 ^{o}C and then vanished upon annealing at 600 ^{o} [67]. The same line could be produced after hydrogenation at 725 ^{o}C and subsequent quenching to RT. The donor was unstable, annealing out at 150 ^{o}C, but could be reactivated (presumably from the dissociation of "hidden" molecular hydrogen) by annealing near ~450 ^{o}C and above. It was suggested therefore, that there exists a reservoir of hydrogen molecules which thermally dissociate between ~400 ^{o}C and ~600 ^{o}C into H related-defects; and a kind of cyclic hydrogen passivation effect takes place causing the observed quenching of the DLE.

Finally, the increase in DLE intensity upon high temperature annealing (remark (v)) is associated with the degradation of the sample (i.e. the creation of new point defects). D'art [68] has studied the evaporation rate of ^{64}Zn from ZnO as a function of annealing temperature (between ~150 ^{o}C and ~900 ^{o}C), both with and without electron bombardment, using a mass spectrometer. In his experiments the author detected two ion peaks with mass 64 amu (atomic mass units) corresponding to Zn, and with mass 80 amu corresponding to ZnO. Because ^{64}Zn is the most abundant in nature and in order to avoid any possibility of varying background contamination, the evaporation of ZnO was followed by measuring the ^{64}Zn ions produced. It was found that without electron bombardment Zn atom starts to evaporate at ~700 ^{o}C [68]. An exponential increase in evaporation rate was reported for temperatures up to ~900 ^{o}C [68]. This indicates that annealing near this temperature (~900 ^{o}C) results in the formation of new Zn and O related-defects (V_{Zn}, V_O, Zn_i…). Based on these findings, the overall observed increase in the intensity in the blue-green part of the PL spectra following annealing between ~700 ^{o}C and ~900 ^{o}C, irrespective of annealing ambient, is associated with the effect of the degradation of the ZnO.

In summary, the increase in the UV intensity after annealing at ~300 ^{o}C, irrespective of the ambient, is ascribed to the removal of surface adsorbed impurities and an increased effect of hydrogen passivation. The quenching of the DLE at this annealing temperature is ascribed to hydrogen passivation. The overall increase in the intensity of the DLE after annealing at ~400 ^{o}C reflects indirectly the out-diffusion of hydrogen trapped in vacancies and the dissociation of point defect complexes. Furthermore, annealing between 300 ^{o}C and 600 ^{o}C activates defects that are radiatively active in the yellow-red part of the PL spectrum.The quenching of the DLE from ~400 ^{o}C to ~600 ^{o}C, irrespective of the environment of annealing, is suggested to be due to the activation of “hidden” interstitial or substitutional hydrogen molecules that are converted into atomic hydrogen. At high temperatures (>700 ^{o}C), the nanorods are degraded. Annealing between 800 ^{o}C and 900 ^{o}C creates an abundance of point defects that are radiatively active in the blue-green region of the spectrum.

Unfortunately under the conditions of annealing as specified, RT PL spectroscopy of the nanorods does not reveal effectively the effect of the ambient. The failure to observe the effect of the environment on the DLE emission at RT under these conditions does not necessary implys that the ambient has no effect. Studies on the surface stoichiometry showed that the ambient does indeed affect the creation of native defects in the rods. The results discussed next summarise efforts made in order to trace the effect of the ambient on the DLE of sequentially annealed nanorods.

4.2.4.2 Effect of annealing environment on the optical properties of nanorods

A number of annealing studies have been undertaken, and it was reported that an application of different annealing atmospheres may readily indicate if an increase or decrease in the concentration of a specific intrinsic defect correlates with the PL intensity and position of DLE bands [18, 33, 44, and 58].

As indicated in the previous section high temperature (~800 ^{o}C - ~900 ^{o}C) annealing generates high densities of radiative intrinsic defects. As the main objective of the study is the understanding of the defect-related luminescence in these nanorods, the effect of annealing time on the generation of defects during annealing in nitrogen, oxygen and an environment containing Zn vapour was investigated. For this purpose, different pieces of samples were prepared and annealed at ~900 ^{o}C in the different ambients and for different times. Note that the annealing times given below refer to the times that the samples were kept in the hot zone of the furnace.

The effect of annealing time in nitrogen and oxygen

Fig. 4.30 shows RT PL spectra of nanorods, as-grown and after annealing at 900 ^{o}C in controlled flows of (a) N_2 and (b) O_2 for different times. The rods were sequentially annealed and the times indicated in the figure are the total annealing time before the corresponding RT PL spectrum was recorded. The sample deposited on a clean quarts spoon was introduced into a quartz tube of the furnace under the desired flow of gas and annealed for the set time.

It can be seen that with sequential annealing in N_2 and O_2 at atmospheric pressure the DLE intensity increases in different spectral ranges, depending on the ambient. Specifically, from fig. 4.30a it is seen that the DLE is weakly enhanced in the yellow-red region of the spectrum up to a total annealing time of 4 minutes (see the green spectrum). A further increasing in annealing time to 8 minutes causes a decrease in the DLE intensity in this spectral range (see blue and cyan spectra), and an increase in the green DLE band. After 12 minutes there is an overall increase in the DLE intensity (magenta spectrum). Finally, after 18 minutes, the red DLE band quenches completely, while the green band dominates the DLE (dark yellow spectrum). The behaviour depicted in fig. 4.30b can be summarised as follows: to the DLE in the yellow-red region of the spectrum quenches after a 2-minute anneal in O_2 (red spectrum). Upon a further increase in annealing time the DLE intensity increases (blue spectrum). An overall increase of the DLE intensity compared to previous DLE intensities after 8 minutes of annealing in O_2 flow is observed (cyan spectrum). Furthermore, the DLE shifts with increasing annealing time as indicated in fig. 4.30b (by the orange arrow).

From the above remarks one important fact is worth noticing, namely the strong increase in the blue-green emission after prolonged annealing, at 900 °C, regardless of the ambient (N_2 or O_2).

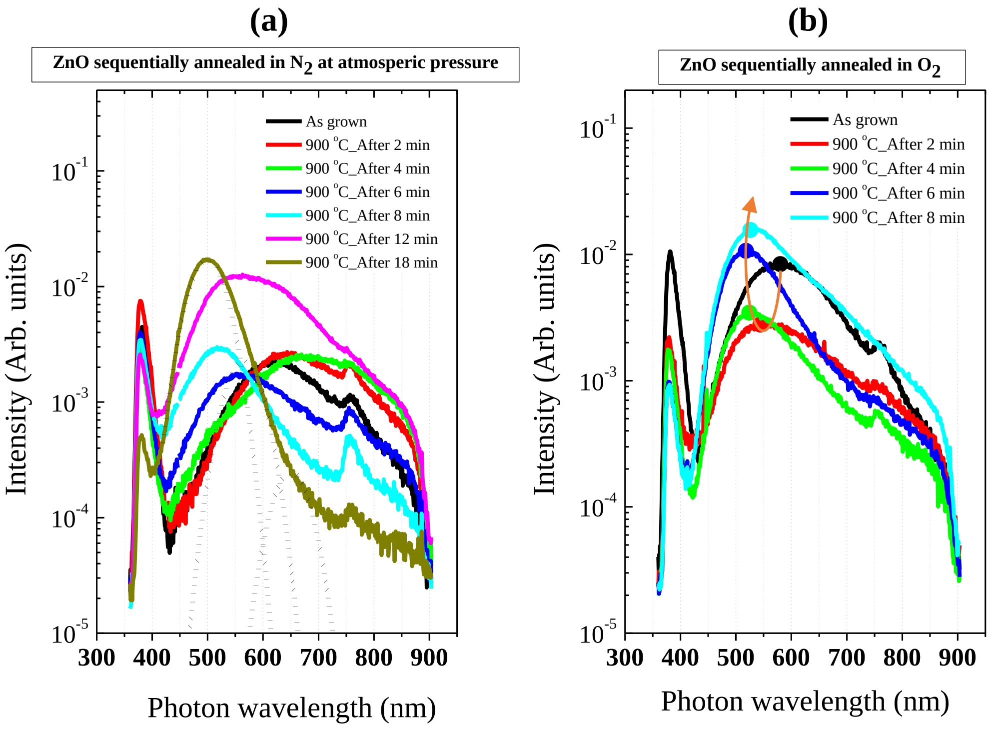

Figure 4.30. Evolution of DLE in the RT PL spectra upon thermal treatment at 900 °C in (a) N2 and (b) O_2. Dotted lines indicate the positions and widths of the visible emission bands. The orange arrow connecting the spherical dots shown in b is a guide to the eye.

The remarkable quenching of the red DLE is attributed to the degradation of the nanorods, causing a decrease in the concentration of radiative defects contributing in this region of the spectrum. The overall increase of the DLE intensity observed after 12 min of anneal (see magenta spectrum in fig. 4.30a) and 8 min anneal (see cyan spectrum in fig. 4.30b) is suggested to result from the “degradation of nanorods” following high temperature annealing. It is primarily suggested that an O_2 ambient does not affect the green luminescence of the nanorods, specifically the deep emission band centered at ~500 nm. Concerning the red band, it is suggested to result from recombination involving V_O–related defects (eg. Zn_iV_O) even though there is not any experimental evidence so far. This assignment is in agreement with recent results from Wang *et al.* [69]. By implanting Zn^+ ions into undoped ZnO single crystals in order to induce Zn interstitials and oxygen vacancies, the authors observed a broad red DLE band at ~630 nm, with a nearly perfect Gaussian lineshape and associated it to a "self-activated" optical transition between a shallow donor and the defect centre of the Zn_iV_O complex or $V_{Zn}V_O$ di-vacancies, based on the configurational coordinate (CC) model [69]. Finally, the shifts observed as function of annealing time can be an indication the activation of V_{Zn}- and V_O-related defects does not necessarily happen simultaneously.

The quenching of the UV emission observed after annealing in O_2 flow (and not in N_2 flow) is attributed to "band bending" in the "near surface of nanorods" rather than to "the degradation of nanorods". It was shown by Liu *et al.* [70] that the exposure of ZnO rods to air (containing O_2) causes the adsorption of O_2 molecules on the surface. The authors showed that the adsorbed O_2 molecule can capture an electron to form a superoxide anionO_2^-, which causes a band bending near the surface. First-principles total-energy calculations done by Yanfa *et al.* [71] confirms this idea. It is thus suggested that under O_2 flow, O_2 molecules adsorb on the surfaces of the rods, resulting in a "residual" electric field near the surface that causes the reduction in intensity of the UV emission.

The effect of Zn environment on the DLE

Fig. 4.31 shows normalised RT PL spectra of nanorods annealed for 30 minutes at 900 ^oC in different environments: (a) a controlled flow of Ar and (b) a controlled flow of Ar, with Zn vapour from a pure Zn plate upstream from the sample. Fig. 4.31c shows normalised RT PL spectra of the annealed nanorods from fig. 4.31a and b. It is worth also noting that the melting point of Zn is 419.53 °C and the boiling point ~907 °C [72]. From fig. 4.31a, it is seen that annealing in an Ar flow caused a significant activation of defects, predominantly radiating in the blue-green part of the spectrum.

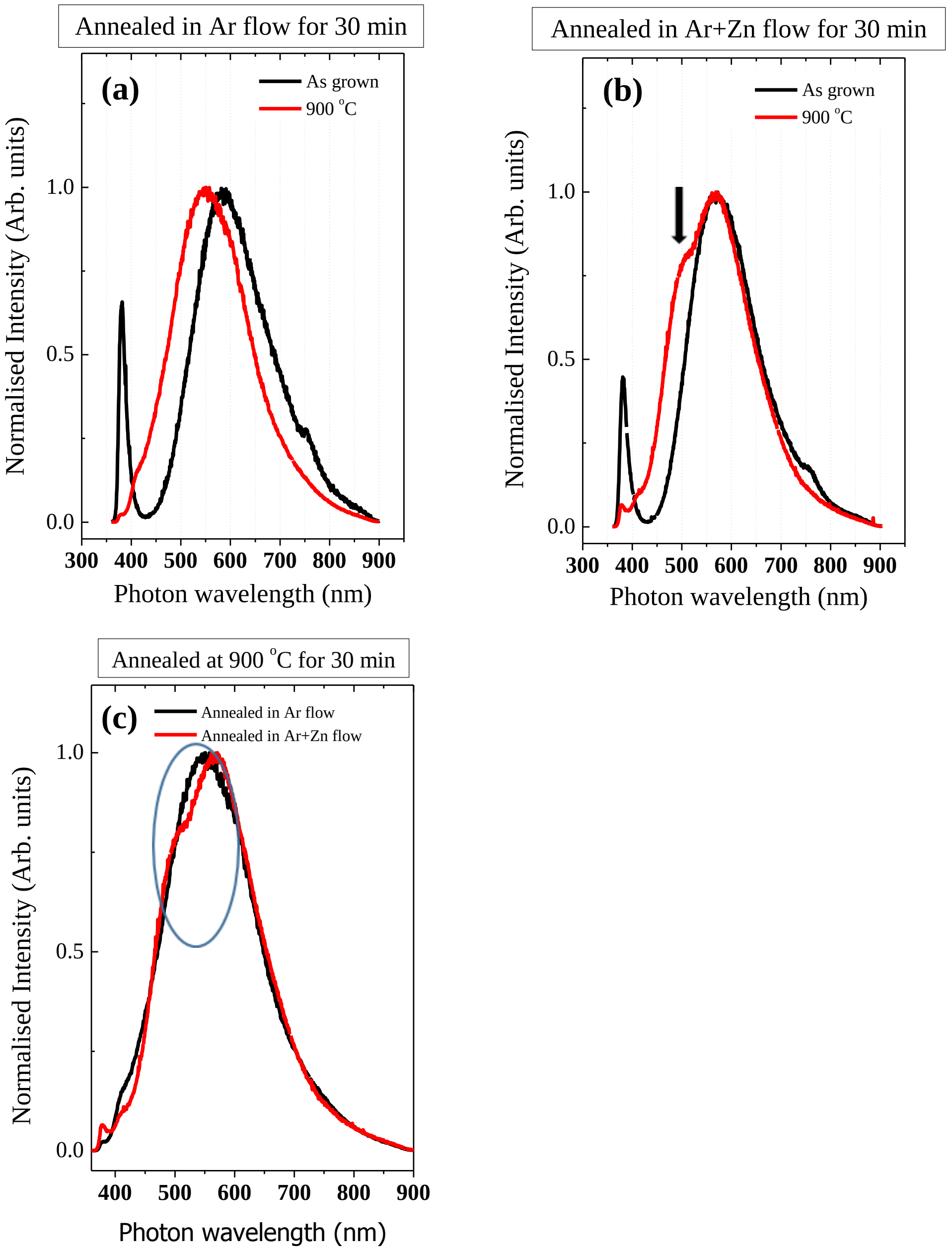

Figure 4.31. (a) RT PL spectra for samples annealed in Ar. (b) RT PL spectra for samples annealed in Ar and Zn vapour. (c) RT PL spectra extracted from (a) and (b) for comparison purposes.

From fig. 4.31b it is seen that the addition of Zn vapour during annealing caused the same effect, but with a slight difference: the activation of the defects emitting in the blue-green part of the spectrum was slowed down. This finding is more clearly depicted in fig. 4.31c (see encircled region). It is thus concluded that the presence of Zn during annealing at 900 °C primarily affects the green deep emission band (~500 nm), which is suggested to involve V_{Zn} related-defects. The same assignment of the green luminescence activated at 900 °C was made recently by Wang *et al.* [73]. Using positron annihilation spectroscopy, the authors showed that the introduction of the green luminescence (~500 nm) in undoped ZnO grown by pulsed laser deposition is correlated with the formation of Zn vacancies at 900 ^{o}C.

In order to confirm the above assignment, another annealing experiment was conducted at 900 ^{o}C, in which the aim was to passivate V_{Zn} related-defects. Fig. 4.32a presents RT PL spectra of nanorods sequentially annealed in different environments and at different temperatures. For comparison purpose the same spectra given in fig. 4.32a have been normalised and plotted in fig. 4.32b. Firstly, the rods were annealed in an Ar flow for 30 minutes at 800 ^{o}C, in order to activate intrinsic defects. As a result the DLE was enhanced (see red spectrum in fig. 4.32a). The sample was subsequently annealed for another minute in the same Ar flow, but with Zn vapour also present in the flowing gas stream. After 1 min of annealing, the DLE was quenched and partially resolved while the UV emission was enhanced (see the green spectrum in fig. 4.32a). Unnumbered arrows in fig. 4.32b indicate the partially resolved bands. In order to confirm the authenticity of these bands, a filter with 450 nm cut-off wavelength (KV450) was used. The quenching of the green band observed previously (see fig. 4.31b or c) is again evident in these figures. The enhancement in UV emission intensity is presumably due to the annihilation of V_{Zn} by Zn atoms. Therefore, it is strongly suggested that the observed green DLE band results from V_{Zn}-related defects. The origins of the bands at longer wavelengths (~550 nm (or 575 nm)), ~650 nm and 750 nm are unknown at present.

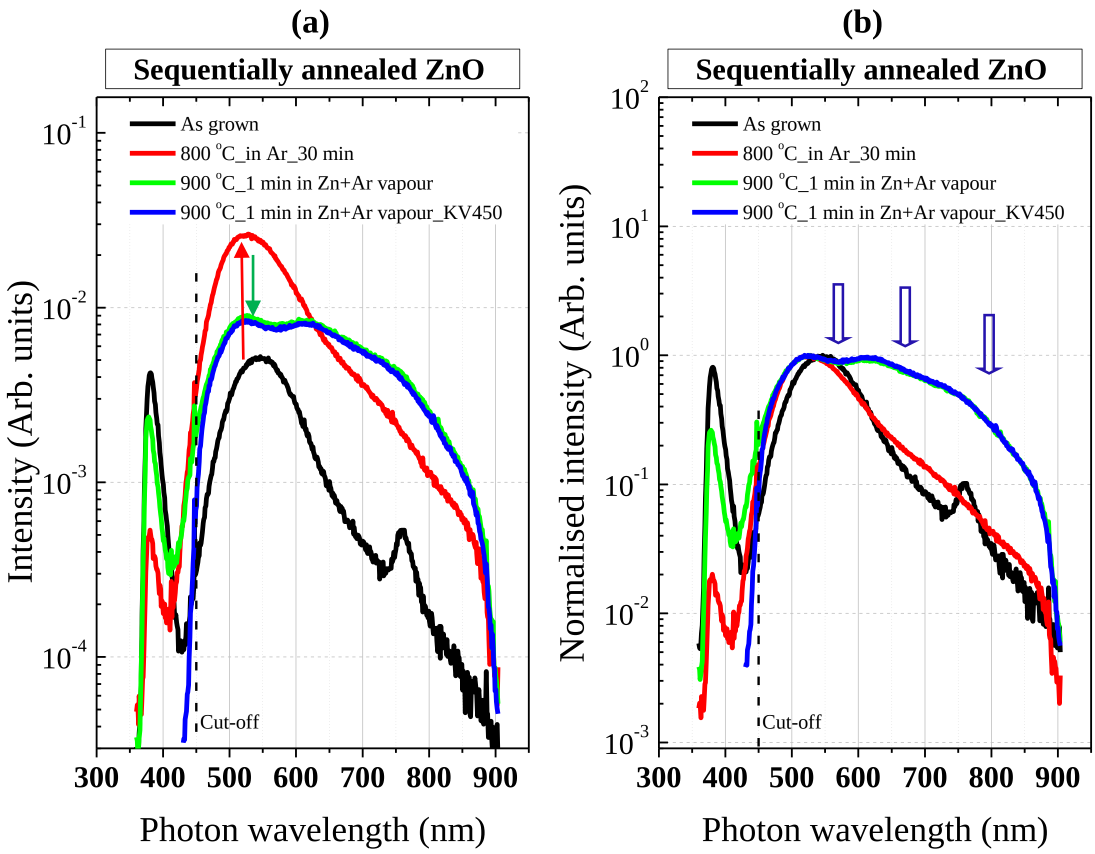

Figure 4.32. RT PL spectra of ZnO nanorods annealed sequentially in Ar at 800 °C and then at 900 °C in Ar and Zn vapour. The numbered arrows indicate subsequent spectral developments caused by (1) annealing in Ar, and (2) annealing in Ar and Zn vapour. Unnumbered arrows in b indicate partially resolved DLE bands.

5. CONCLUSIONS AND OUTLOOK

Zinc oxide (ZnO) nanorods grown by a two-step chemical bath deposition method on a Si substrate were characterized. As-grown ZnO nanorods were thermally treated and studied for a better understanding of the optical properties at room temperature, with the emphasis on the visible luminescence. To this end, thermal treatments of as-grown ZnO nanorods were conducted under different conditions. Specifically the following studies were performed: an investigation of the structure of ZnO nanorods, an analysis of the chemical composition, an investigation of the surface stoichiometry of ZnO nanorods, and a study of defect related-photoluminescence of ZnO nanorods upon thermal treatment in different ambients.The morphology, orientation, and phase of ZnO nanorods were investigated by Scanning Electron Microscopy and X-ray Diffraction. The presence of extrinsic defects throughout ZnO nanorods were probed by Time-of-Flight Secondary Ion Mass Spectrometry. X-ray Photoelectron Spectroscopy and Auger Electron Spectroscopy were used to probe the surface stoichiometry in as-grown ZnO nanorods, as well as in thermally treated ZnO nanorods. Finally, the room temperature optical properties were investigated by Photoluminescence Spectroscopy.

It was observed that as-grown ZnO nanorods exhibit a hexagonal shape and have the wurtzite structure. They have an average length and diameter of ~900 nm and ~50 nm, respectively, and formed perpendicular to the substrate. The main extrinsic species found in as-grown nanostructures were C, H, F, S, and Cl. ToF-SIMS and XPS confirmed the presence of H related-defects, and the oxygen 1S XPS peak at 531.5 eV was therefore assigned to oxygen bound to H related defects. Based on stoichiometry studies, it was found that the near surface regions of solution grown ZnO nanorods is rich in Zn. The room temperature optical properties of as-grown ZnO nanorods were observed to exhibit a near band edge emission centered at ~379.5 nm and deep level emission extending from ~450 nm to ~850 nm. When these nanorods were thermally treated at high temperatures (>850 ^{o}C), it was found that even though their crystalline quality was preserved (as indicated by XRD), their morphology was significantly affected, regardless of the annealing ambient. Furthermore, in the near-surface regions of annealed ZnO nanorods it was found that the Zn/O stoichiometry ratios deviated strongly from unity, showing that thermal treatment indeed affected the concentration of Zn and O. Hence, it was concluded that oxygen vacancy-related defects form within the first 100 nm from the surface, followed by zinc vacancy-related defects further from the surface. Within the detection limit of XPS and AES, it was confirmed that the environment of annealing affects indeed the activation of intrinsic defects, and the only extrinsic defects that were significantly affected by thermal treatment were found to be H-related.

Thermal treatment at high temperatures removed H-related defects, and this removal process was found to affect significantly the room temperature luminescence properties of ZnO nanorods, especially when ZnO nanorods were annealed sequentially from 300 ^{o}C to ~700 ^{o}C in temperature increments of 100 ^{o}C. Specifically, the passivation of vacancy-related defects by H was demonstrated following thermal treatment in this temperature range. Through PL spectroscopy this passivation was probed by following first the progressive quenching and then the enhancement of the blue-green and the yellow-red luminescence bands, regardless of the annealing ambient.

Finally, the green luminescence that evolved following annealing above ~800 ^{o}C was assigned to Zn vacancy-related defects. The red luminescence that dominates the visible emission from ZnO nanorods between 400 ^{o}C and 600 ^{o}C was suggested to be due to oxygen vacancy-related defects.

Suggestions for future work

It is hoped that these results will stimulate other researchers to explore effective ways to suppress completely H-related defects in ZnO nanorods and to master the controlled creation of intrinsic defects in ZnO nanorods by annealing. This will hopefully lead to practical applications of ZnO nanorods in the future. These results can also further stimulate theoretical investigations on the mechanisms of out-diffusion from ZnO nanorods.

REFERENCES

[1] *ZnO nanonails: synthesis and their application as glucose biosensor.* **A. Umar, M. M. Rahman, S. H. Kim, and Y. B. Hahn.** 2008, J. Nanosci. Nanotechnol., Vol. 8, p. 3216.

[2] *Membrane potential measurements across a human fat cell using ZnO nanorods.* **S. Al-Hill and M. Willander.** 2009, Nanotechnol. , Vol. 20, p. 175103.

[3] *Single gallium nitride nanowire lasers.* **J. C. Johnson, H. J. Choi, K.P. Knutsen, R. D. Schaller, P. Yang, and R. J. Saykally.** 2002, Nat. Mater. , Vol. 1, p. 106.

[4] *Semiconductor nanowire laser and nanowire waveguide electro-optic modulators.* **A. B. Greytak, C. J. Barrelet, Y. Li, and C. M. Lieber.** 2005, Appl. Phys. Lett., Vol. 87, p. 151103.

[5] *Nanoribbon Waveguides for Subwavelength Photonics Integration.* **M. Law, D. J. Sirbuly, J. C. Johnson, J. Goldberger, R. J. Saykally, and P. Yang.** 2004, Sci. , Vol. 305, p. 1269.

[6] *From ZnO nanorods to 3D hollow microhemispheres: solvothermal synthesis, photoluminescence and gas sensor properties.* **H. Zhang, J. B. Wu, C. X. Zhai, N. Du, X.Y. Ma, and D. R. Yang.** 2007, Nanotechnol. , Vol. 18 , p. 455604.

[7] *Effect of growth parameters on MgxZn(1-x)O films grown by metalorganic chemical vapour deposition.* **K. Talla, J.K.Dangbegnon, M.C.Wagener , J.Weber , and J.R.Botha.** 2011, J. Cryst. Growth, Vol. 315, p. 297.

[8] *Silicon-Based Light Sources for Silicon Integrated Circuits.* **Pavesi, L.** 2008, Adv. Opt. Technol., Vol. 2008, p. 1.

[9] *Growth of ZnO nanostructures by vapor liquid solid.* **Q. X. Zhao, P. Klason and M. Willander.** 2007, Appl. Phys. A, Vol. 88, p. 27.

[10] *Catalytic Growth of Zinc Oxide Nanowires by Vapor Transport.* **M. H. Huang, Y. Wu, H. Feick, N. Tran, E. Weber, and P. Yang,.** 2001, Adv. Mater, Vol. 13, p. 113.

[11] *Growth of aligned ZnO nanorod arrays by catalyst-free pulsed laser deposition methods.* **Y. Sun, G. M. Fuge, and M. N. R. Ashfold.** 2004, Chem. Phys. Lett., Vol. 396, p. 21.

[12] *Molecular Beam Epitaxy growth of ZnO layers on sapphire employing hydrogen peroxide as an oxidant.* **A. Bakin, A. El-Shaer, A. Che Mofor, M. Kreye, A. Waag, and F. Bertram.** 2006, J. Cryst. Growth, Vol. 287, p. 7.

[13] Growth and Characterization of ZnO Nanorods using chemical bath deposition. **Z.N. Urgessa.** Nelson Mandela Metropolitan, 2012 (PhD thesis).

[14] *Origin of the surface recombination centers in ZnO nanorords arrays by X-ray photoelectron spectroscopy.* **L. L. Yang, Q. X. Zhao, M. Willander, X. J. Liu, M. Fahlman, and J. H Yang.** 2010, Appl.Surf. Sci., Vol. 256, p. 3592.

[15] *Characteristics of point defects in the green luminescence from Zn- and O-rich ZnO.* **C. Ton-That, L. Weston, and M. R. Philips.** 2012, Phys. Rev. B, Vol. 86, p. 115205.

[16] *Effect of humidity on the gas sensing property of the tetrapod-shaped ZnO nanopowder sensor.* **Z. K. Bai, C. S. Xie, M. L. Hu, S. P. Zhang, and D. W. Zeng.** 2008, Mater. Sci. Eng. B, Vol. 149, p. 12.

[17] *Enhanced photocatalytic activity of ZnO nanotetrapods.* **Q. Wan. T. H. Wang, and J. C. Zhao.** 2005, Appl. Phys. Lett., Vol. 87, p. 083105.

[18] *Low temperature near band edge recombination dynamics in ZnO nanorods.* **Z.N. Urgessa, J.R. Botha, M.O. Eriksson, C.M. Mbulanga, S.R. Dobson, S.R. Tankio Djiokap, K.F. Karlsson, V. Khranovskyy, R. Yakinova and Per-Olof Holtz.** 2014, J. Appl. Phys., Vol. 116, p. 123506.

[19] *TOF SIMS induced artificial topographical effects on the* $Y_2(Al,Ga)_5O_{12}:Tb^{3+}$ *thin films deposited on Si substrates by the pulsed laser deposition technique.* **A. Yousif, R. M. Jafer, J. J. Terblans, O. M. Ntwaeaborwa, and M. M. Duvenhage.** 2014, Appl. Surf. Sci. , Vol. 313, p. 524.

[20] *Zinc Oxide From Fundamental Properties Towards Novel Application*. **C. F. Klingshirn, B. K. Meyer, A. W. A. Hoffmann and J. Geurts.** Springer, 2010. p. 351.

[21] *A comprehensive review of ZnO materials and devices.* **Ü. Özgür, Y. I. Alivov, C. Liu, A. Teke, M. A. Reshchikov, S. Dogan, V. Avrutin, S.-J. Cho, and H. Morkoc.** 2005, J. Appl. Phys., Vol. 98, p. 041301.

[22] *Zinc Oxide: Bulk, Thin Films and Nanostructures.* **C. Jagadish and S. J. Pearton.** Elsevier, 2006. p. 577.

[23] *The chemistry and physics of zinc oxide surfaces.* **C. Woll.** 2007, Prog. Surf. Sci., Vol. 82, p. 55.

[24] *Zinc Oxide Fundamentals, Materials, and Device Technology.* **H. Morkoc and U. Ozgur.** WILEY-VCH Verlag GmbH & Co. KGaA,, 2009. p. 469.

[25] *ZnO: Material, Physics and Applications.* **C. Klingshirn.** 2007, Chem. Phys. Chem., Vol. 782, p. 8.

[26] *Preparation of ZnO:N Films by Radical Beam Gettering Epitaxy.* **I. V. Rogozin.** 2006, Electronic and optical properties of semiconductors, Vol. 41, p. 924.

[27] *The physics of semiconductors, An Introduction including Nanophysics and Applications.* **M. Grundmann.** Springer, 2010.

[28] *High quantum efficiency for a porous silicon light emitting diode under pulsed operation.* **J. Linnros and N. Lalic.** 1995, Appl. Phys. Lett., Vol. 66, p. 3048.

[29] *On the origin of suppression of free exciton no-phonon emission in ZnO tetrapods.* **S. L. Chen, S. K. Lee, W. M. Chen, H. X. Dong, L. Sun, Z. H. Chen and I. A. Buyanova.** 2010, Appl. Phys. Lett., Vol. 96, p. 033108.

[30] *Fundamentals of Semiconductors.* **Y. Yu Peter and M. Cardona.** London : Springer, 2010.

[31] *Shallow donors and acceptors in ZnO.* **B. K. Meyer, J. Sann, D. M. Hofmann, C. Neumann, and A. Zeuner. 2005, Semicond. Sci. Technol., Vol. 20, p. S62.**

[32] *First principles study of native point defects in ZnO.* **A. F. Kohan, G. Ceder and D. Morgan.** 2000, Phys.Rev. B, Vol. 61, p. 15019.

[33] *Identification of oxygen and zinc vacancy optical signals in ZnO.* **T. Moe Børseth, B. G. Svensson, A. Yu. Kuznetsov, P. Klason, Q. X. Zhao, and M. Willander.** 2006, Appl. Phys. Lett., Vol. 89, p. 262112.

[34] *Luminescence from Zinc Oxide Nanostructures and Polymers and their Hybrid Devices.* **M. Willander , O. Nur, J. R. Sadaf, M. I. Qadir, S. Zaman, A. Zainelabdin, N. Banoand and I. Hussain.** 2010, Materials, Vol. 3, p. 2643.

[35] *Zinc oxide nanorod based photonic devices: recent progress in growth, light emitting diodes and lasers.* **M. Willander, O. Nur, Q.X. Zhao, L.L. Yang, M. Lorenz, B.Q. Cao, J. Z. Perez, C. Czekalla, G. Zimmermann, M. Grundmann, A. Bakin, A. Behrends, M. AlSuleiman, A. El-Shaer, A. C. Mofor, B. Postels, A. Waag, N. Boukos, A. Travlos, H.S. Kwack and J. Guinard.** 2009, Nanotechnology, Vol. 20, p. 332001.

[36] *Influences of ZnO sol-gel thin film characteristics on ZnO nanowire arrays prepared at low temperature using all solution-based processing.* **J. Huang and C. Lin.** 2008, J. Appl. Phys., Vol. 103, p. 014304.

[37] *Review the chemistry and physics of zinc oxide surfaces.* **Woll, Christof.** 2007, Progress in Surface Science, Vol. 82, p. 55.

[38] *First-principles calculations of solubilities and doping limits: Li, Na, and N in ZnSe.* **C. G. Van de Walle, D. B. Laks, G. F. Neumark and S. T. Pantelides.** 1993, Phys. Rev. B, Vol. 47, p. 9425.

[39] *Chemical potential dependence of defect formation energies in GaAs: dpplication to Ga delf-diffusion.* **S. B. Zhang and J. E. Northrup.** 1991, Phys. Rev. Lett., Vol. 67, p. 17.

[40] *First-principles study of migration mechanisms and diffusion of oxygen in zinc oxide.* **P. Erhart and K. Albe.** 2006, Phy. Rev. B, Vol. 73, p. 115207.

[41] *Diffusion of zinc vacancies and interstitials in zinc oxide.* **P.l Erhart and K. Albe.** 2006, Appl. Phys. Lett., Vol. 88, p. 201918.

[42] *A comparative analysis of deep level emission in ZnO layers deposited by various methods.* **C. H Ahn, Y. Y. Kim, D. C. Kim, S. K. Mohanta, and H. K. Cho.** 2009, J. Appl. Phys., Vol. 105, p. 013502.

[43] *Blue luminescent center in ZnO films deposited on silicon substrates.* **Z. Fang, Y. Wang, D. Xu, Y. Tan and X. Liu.** 2004, Optical Mat., Vol. 26, p. 239.

[44] *Zinc vacancy and oxygen interstitial in ZnO revealed by sequential annealing and electron irradiation.* **K. E. Knutsen, A. Galeckas, A. Zubiaga, F. Tuomisto, G. C. Farlow, B. G. Svensson and A. Yu. Kuznetsov.** 2012, Phys. Rev. B, Vol. 86, p. 121203.

[45] *Defects produced in ZnO by 2.5-MeV electron irradiation at 4.2 K: Study by optical detection of electron paramagnetic resonance.* **Y. V. Gorelkinskii and G. D. Watkins.** 2004, Phys. L. Rev., Vol. B69, p. 115212.

[46] **J. J. Friel.** *X-ray and image analysis in electron microscopy.* s.l. : Princeton Gamma-Tech, Inc, 2003.

[47] *Excitonic structure and absorption coefficient measurements of ZnO single crystal epitaxial films deposited by pulsed laser deposition.* **J. F. Muth, R. M. Kolbas, A. K. Sharma, S. Oktyabrsky and J. Narayan.** 1999, J. Appl. Phys., Vol. 85, p. 7884.

[48] *Science of Microscopy.* **P. W. Hawkes, J.C.H. Spence. [ed.]** New York : Springer Science + Business Media, LLC, 2007. Vol. 1.

[49] *Application of XPS to study electrocatalysts for fuel cells.* **C.J. Corcoran, H. Tavassol, M.A. Rigsby, P.S. Bagus and A. Wieckowski.** 2010, Journal of Power Sources, Vol. 195, p. 7856 .

[50] *Handbookof X-ray photoelectron spectroscopy*. **C.D. Wagner, W.M. Riggs, L.E. Davis, J.F. Moulder and G.E. Muilenberg**. Perkin-Elmer Corporation, 1978.

[51] *Effect of precursor concentration on the growth of zinc oxide nanorod arrays.* **Z. N. Urgessa, O. S. Oluwafemi, and J. R. Botha.** 2012, Physica B, Vol. 407, p. 1543.

[52] NIST X-ray Photoelectron Spectroscopy Database. [Online] 2015. http://srdata.nist.gov/xps/Spec_query.aspx?EType=PE&ENE=284.8+&ENEERR=1.0&EType1=-1&ENE1=&ENEERR1=1.0&EType2=-1&ENE2=&ENEERR2=1.0&EType3=-1&ENE3=&ENEERR3=1.0.

[53] *Origin of the red emission in ZnO nanophosphors.* **V. Kumar, H. C. Swart, O. M. Ntwaeaborwa, R.E Kroon, J. J. Terblans, S. K. K. Shaat, A. Yousif, and M. M. Duvenhage.** 2013, Mater. Lett., Vol. 101, p. 57.

[54] *The stability of the polar surfaces of ZnO: a reinvestigation using He-atom scattering.* **M. Kunat, S. Gil-Girol, T. Becker, U. Burghaus, and C. Woll.** 2002, Phy.Rev. B, Vol. 66, pp. 081402-1.

[55] *Photoluminescence study of hydrogen donors in ZnO.* **F. Herklotz, E. V. Lavrov, and J. Weber.** 2009, Physica B, Vol. 404, p. 4349.

[56] *The defect passivation effect of hydrogen on the optical properties of solution-grown ZnO nanorods.* **Z.N. Urgessa, C.M. Mbulanga, S.R. Tankio Djiokap, J.R. Botha, M.M Duvenhage, and H.C. Swart.** 2015, Physica B, In press.

[57] *Tuning of defects in ZnO nanorod arrays used in bulk heterojunction solar cells.* **D. C Iza, D. M. Rojas, Q. Jia, B. Swartzentruber and J. L MacManus-Driscoll.** 2012, Nanoscale Research Letters, Vol. 7, p. 655.

[58] *Annealing effects on the optical and morphological properties of ZnO nanorods on AZO substrate by using aqueous solution method at low temperature.* **D.R. Hang, S.E. Islam, K.H. Sharma, S.W. Kuo, C.Z. Zhang and J.J. Wang.** 2014, Nanoscale Research Letters, Vol. 9, p. 632.

[59] *Surface effects on photoluminescence of single ZnO nanowires.* **Z.M. Liao, H.Z. Zhang, Y.B. Zhou, J. Xua, J.M. Zhang, and D.P. Yu.** 2008, Phy. Lett. A, Vol. 372, p. 4505.

[60] *Size-dependent surface luminescence in ZnO nanowires.* **I. Shalish, H. Temkin and V. Narayanamurti.** 2004, Phys. Rev. B, Vol. 69, p. 245401.

[61] *Stable enhancement of near-band-edge emission of ZnO nanowires by hydrogen incorporation.* **A. Dev, R. Niepelt, J. P. Richters, C. Ronning and T. Voss.** 2010, Nanotechnology, Vol. 21, p. 065709.

[62] *Identification of two hydrogen donors in ZnO.* **E. V. Lavrov, F. Herklotz, and J. Weber.** 2009, Phys. Rev. B, Vol. 79, p. 165210.

[63] *Effects of Hydrogen Plasma Treatment on the Electrical and Optical Properties of ZnO Films: Identification of Hydrogen Donors in ZnO.* **J. J. Dong, X. W. Zhang, J. B. You, P. F. Cai, Z. G. Yin, Q. An, X. B. Ma, P. Jin, Z. G. Wang, and P. K. Chu.** 2010, Applied materials and interface, Vol. 2, p. 1780.

[64] *Remote hydrogen plasma processing of ZnO single crystal surfaces.* **Y .M. Strzhemechny,J. Nemergut,P.E. Smith, J. Bae, and D.C. Look.** 2003, J. Appl. Phys., Vol. 94, p. 4256.

[65] *Anionic and Hidden Hydrogen in ZnO.* **Mao-Hua Du and K. Biswas.** 2011, Phys. Rev. Lett., Vol. 106, p. 115502.

[66] *Interaction of zinc interstitial with oxygen vacancy in zinc oxide: An origin of n-type doping.* **Dae-Hee Kim, Ga-Won Lee, and Yeong-Cheol Kim.** 2012, Solid State Communications, Vol. 152, p. 1711.

[67] *Hidden hydrogen in as-grown ZnO.* **G. A. Shi, M. Saboktakin, M. Stavola, and S. J. Pearton.** 2004, Appl. Phys. Lett., Vol. 85, p. 5601.

[68] *Evaporation of Zinc and Zinc Oxide under Electron Bombardment.* **Dart, F. E.** 1950, Phys. Rev., Vol. 78, p. 761.

[69] *Nature of red luminescence band in research-grade ZnO single crystals: A "self-activated" configurational transition.* **Y. N. Chen, S. J. Xu, C. C. Zheng, J. Q. Ning, F. C. C. Ling, W. Anwand, G. Brauer, and W. Skorupa.** 2014, Appl. Lett. Phys. , Vol. 105, p. 041912 .

[70] *Effect of oxygen-related surface adsorption on the efficiency and stability of ZnO nanorod array ultraviolet light-emitting diodes.* **W. Z. Liu, H. Y. Xu, J. G. Ma, C. Y. Liu, and Y. X. Liu.** 2012, Appl. Phys. Lett., Vol. 100, p. 203101.

[71] *Oxygen-vacancy mediated adsorption and reactions of molecular oxygen on the ZnO (10-10) surface.* **M.M. Yanfa Yan, Al-Jassim, and Su-H. Wei.** 2005, Phys. rev. B, Vol. 72, p. 161307(R).

[72] International zinc association. [Online] [Accessed: 05 25, 2015.] http://www.zinc.org/basics

[73] *The Zn-vacancy related green luminescence and donor–acceptor pair emission in ZnO grown by pulsed laser deposition.* **Z. Wang, S. C. Su, M. Younas, F. C. C. Ling, W. Anwand and A. Wagner.** 2015, RSC Adv., Vol. 5, p. 12530.